Tuomas Haggrén

Growth of Gallium Arsenide Nanowires on Silicon

School of Electrical Engineering

Thesis submitted for examination for the degree of Master of Science in Technology.

Espoo 10.11.2011

Thesis supervisor:

Prof. Harri Lipsanen

Thesis intructors:

Docent Teppo Huhtio

D.Sc. (Tech) Veer Dhaka

AALTO UNIVERSITY
SCHOOL OF ELECTRICAL ENGINEERING

ABSTRACT OF THE
MASTER'S THESIS

Author: Tuomas Haggrén

Title: Growth of Gallium Arsenide Nanowires on Silicon

Date: 31.10.2011 Language: English Number of pages: 8 + 71

Department of Micro- and Nanosciences

Professorship: Nanotechnology Code: S-104

Supervisor: Prof. Harri Lipsanen

Instructors: Doc. Teppo Huhtio, D.Sc. (Tech.) Veer Dhaka

In this thesis, gallium arsenide nanowires (NW) were grown on silicon substrates by atmospheric pressure metalorganic vapor phase epitaxy. NWs offer a myriad of novel applications and solutions in a variety of different fields, including optoelectronics. Epitaxial NWs with good optical properties are required in many of the possible applications.

The aim of this work was to grow NWs epitaxially with a good yield, optimize the growth parameters in the used system, and to passivate the surface of the NWs by core-shell structures and atomic layer deposition (ALD) in order to improve their photoluminescence (PL). The used shell materials were AlGaAs and GaAsP, and the ALD coating was aluminum nitride. The NW yield and morphology were characterized with scanning electron microscopy, their crystal structure and quality with transmission electron microscopy, chemical composition with energy-dispersive X-ray spectroscopy and optical properties with PL measurements.

The results showed that the NWs can be grown with a good yield within an appropriate range of temperature, molar ratio, and total molar flow. The passivation methods resulted in drastically improved PL intensity. Also unexpectedly large redshift with AlGaAs shells was observed.

Keywords: Nanowire, gallium arsenide, core-shell, metalorganic vapor phase epitaxy, passivation

AALTO YLIOPISTO
SÄHKÖTEKNIIKAN KORKEAKOULU

DIPLOMITYÖN
TIIVISTELMÄ

Tekijä: Tuomas Haggrén

Työn nimi: Galliumarsenidinanolankojen kasvatus piialustakiteelle

Päivämäärä: 31.10.2011 Kieli: Englanti Sivumäärä 8 + 71

Mikro- ja nanotekniikan laitos

Professuuri: Nanoteknologia Koodi: S-104

Valvoja: Prof. Harri Lipsanen

Ohjaajat: Dos. Teppo Huhtio, TkT Veer Dhaka

Tässä työssä kasvatettiin galliumarsenidinanolankoja piialustakiteille ilmanpaineessa olevalla metallo-orgaanisella kaasufaasiepitaskiamenetelmällä. III-V puolijohteista tehdyillä nanolangoilla on mahdollista toteuttaa lukuisia uusia sovellutuksia monilla eri tieteen aloilla, kuten optoelektroniikassa. Epitaksiaaliset ja optisesti laadukkaat nanolangat ovat edellytyksenä monille sovellutuksille.

Työn tavoitteena oli valmistaa nanolankoja epitaksiaalisesti, optimoida kasvuparametrit ja passivoida lankojen pinta ydin-kuorirakenteella ja atomikerroskasvatustekniikalla, jotta nanolankojen fotoluminesenssiominaisuuksia saataisiin parannettua. Epitaksiaalisesti valmistettuja AlGaAs- ja GaAsP-kuorikerroksia sekä atomikerroskasvatettuja alumiininitridipinnotteita käytettiin GaAs-ytimen passivoinnissa. Nanolangat karakterisoitiin pyyhkäisyelektronimikroskoopilla, läpäisyelektronimikroskoopilla, energiadispersiivisellä röntgenspektrometrialla sekä fotoluminesenssimittauksilla.

Tulokset osoittivat, että lähes kaikki nanolangat kasvoivat epitaksiaalisesti, kun kasvuparametrit lämpötila, moolisuhde ja kokonaismoolivirtaus valittiin oikealta väliltä. Käytetyt passivointimenetelmät paransivat fotoluminesenssisignaalia huomattavasti. Myös odottamattoman huomattava punasiirtymä havaittiin GaAs:lle, kun AlGaAs-kuoren kompositio muuttui.

Avainsanat: Nanolanka, galliumarsenidi, ydin-kuorirakenne, metallo-orgaaninen kaasufaasiepitaksia, passivointi

Preface

This thesis was conducted in Nanotechnology group at the Department of Micro- and Nanosciences of Aalto University. I would like to thank Professor Harri Lipsanen for the opportunity to conduct research with such an intriguing and novel topic while carrying out this thesis. I want to thank him for the interest towards the thesis and all the advices during the work. In addition, I would like to thank the instructors Docent Teppo Huhtio and D.Sc. Veer Dhaka for all the support and advices throughout the work, for all the interest they gave this thesis, and for the useful guidance with the research, as well as the contents of the thesis. Portion of the research was done by Veer Dhaka, and I own my gratitude thereof as well.

I want to give thanks to all of the fellow researchers for the readiness to help and advice whenever needed. I own many thanks to D.Sc. Marco Mattila for numerous invaluable advices regarding the used growth system, phenomena occurring during nanowire growth and many other topics. I want to thank also M.Sc. Päivi Mattila for all the help and instructions with photoluminescence measurements and the related theory. Furthermore, I would like to thank Professor Markku Sopanen for numerous indispensable advices, as well as M.Sc. Henri Jussila for many useful points of view. Also the rest of the personnel deserve great compliments for creating a motivating and pleasant working atmosphere.

Finally, I own special thanks for all the members of my family for the support and inspiration they gave me during the study years and the thesis work.

Contents

Symbols

a_A	Lattice constant for material A
α_V^i, β_V^i	Varshni parameters in valley *i*
ζ^i	Bowing parameter in valley *i*
$\Delta\mu_{vs}$	Chemical potential difference between vapor and substrate
μ_v	Chemical potential of reactant vapor
μ_s	Chemical potential of substrate
k_B	Boltzmann constant
T	Temperature
p_v	Partial vapor pressure of a growth component in vapor phase
p_{v0}	Equilibrium partial vapor pressure of a component over a crystalline phase
f_i	Frequency of a surface diffusion or desorption process
f_0	Cutoff frequency of a surface process
E_i	Activation energy of a surface process
λ_n	Distance between two nucleation sites
f_{diff}	Diffusion frequency
E_{diff}	Average activation energy for diffusion
λ_{diff}	Diffusion length
f_{des}	Desorption frequency for a diffusing adatom
E_{des}	Desorption activation energy
$\Delta\mu_c$	Combined chemical potential difference for group III and V elements
C_{III}	Concentration of group III element in alloy particle
C_V	Concentration of group V elements in vapor phase
$C_{III,eq}$	Concentration of group III element at equilibrium with the crystalline phase
$C_{V,eq}$	Concentration of group V element at equilibrium with the crystalline phase
v_i	Normal velocity of a facet in nanowire growth
α_i	Rate constant for a facet in nanowire growth
μ_l	Chemical potential of growth material in liquid
μ_i	Chemical potential of a growth facet
$p_{l,III}$	Group III element pressure in alloy droplet
r_p	Seed particle diameter
$p_{l\infty,III}$	Vapor pressure of group III element in an infinitely large alloy particle
σ_a	Surface energy of a seed particle
$\Omega_{l,III}$	Atomic volume of group III element in a seed particle
μ_p	Chemical potential in a seed particle
μ_{p0}	Reference state for the chemical potential in a seed particle
$p_{l0,III}$	Reference state for group III partial pressure in an alloy
x_{III}	Atomic fraction of group III element
A_{pt}	Interfacial area between seed particle and nanowire top

A_{wt}	Area at nanowire top within diffusion length of adatoms
χ_e	Electron affinity
p_{vi}	Vapor pressure of precursor *i* in a carrier gas
$\bar{p}$	Proportionality coefficient
v_r	Radial growth rate
v_a	Axial growth rate

Abbreviations

ALD	Atomic layer deposition
AlN	Aluminum nitride
AlAs	Aluminum arsenide
AlGaAs	Aluminum gallium arsenide
AsH_3	Arsine
BHF	Buffered hydrofluoric acid
CS	Core-shell
DI	Deionized
EDS	Energy-dispersive X-ray spectroscopy
GaAs	Gallium arsenide
GaAsP	Gallium arsenide phosphide
GaP	Gallium phosphide
HCl	Hydrochloric acid
HF	Hydrofluoric acid
InAs	Indium arsenide
InP	Indium phosphide
LPE	Liquid phase epitaxy
MBE	Molecular beam epitaxy
MOVPE	Metal-organic vapor phase epitaxy
NP	Nanoparticle
NW	Nanowire
PL	Photoluminescence
QW	Quantum well
SEM	Scanning electron microscope
SiO_2	Silicon dioxide
TBA	Tertiarybutyl arsine
TBP	Tertiarybutyl phosphine
TEM	Transmission electron microscope
TMA	Trimethylaluminum
TMG	Trimethylgallium
TMI	Trimethylindium
VPE	Vapor phase epitaxy
VLS	Vapor-liquid-solid method
VSS	Vapor-solid-solid method
WZ	Wurtzite crystal structure
ZB	Zinc blende crystal structure

1. Introduction

Nanoscale structures promise a myriad of novel applications and solutions in a wide range of research fields. When the size of a structure is reduced to the order of tens of nanometers the proportion of the surface increases dramatically compared to the bulk, and surface properties differ considerably from that of bulk due to atomic interactions. In a bulk crystal the atoms are ordered spatially in energetically favorable positions, but at surface they have a lesser number of bonds leading to a different energy construction. This enables a range of possible novel applications with nanoscale structures, one of which is nanowires. Nanowires have two dimensions in nanoscale and third possibly tens of micrometers long, which leads to a high surface-to-volume ratio. The high surface-to-volume ratio has e.g. allowed development of nanoscale sensors, such as mass sensors [1] and pH sensors [2].

Besides interesting properties related to surface effects, nanowires are available in a variety of materials, including compound semiconductors, which are desired in optoelectronic components. However, integrating compound semiconductors to the main street silicon technology has proven problematic due to mismatched lattices. This problem can be overcome with nanowires due to their small dimensions, which allow epitaxial growth on mismatched materials. Optoelectronic cutting-edge nanowire applications include light-emitting diodes [3], field-effect transistors [4], single-nanowire lasers [5], memory devices [6] and solar cells [7].

One of the most important compound semiconductor materials is gallium arsenide (GaAs), which is used in optical and high frequency electronics. In many applications the surface of GaAs poses limitations, as it has notoriously plentiful trap states within the band gap. These states allow nonradiative recombination of charge carriers, thereby decreasing the performance of optoelectronic components. This is problematic especially with structures with large surface area, such as nanowires. By passivating the surface the optical properties of a component can be remarkably enhanced. The passivation can be performed *ex-situ* or *in-situ* directly after the growth.

Semiconductor nanowires can be grown via different mechanisms, one of which is vapor-liquid-solid (VLS). The VLS can be realized with metal-organic vapor phase epitaxy (MOVPE), with which in-situ passivation of nanowires is also possible using core-shell structures. Other passivation methods include atomic layer deposition (ALD), although little research has been focused on this method.

In the recent years, extensive research has been focused on nanowires. In this work gallium arsenide nanowires were grown on silicon substrates in an atmospheric-pressure MOVPE reactor. The aim of this thesis was to optimize nanowire growth parameters in the used reactor and to study effects of different passivation methods. Effects of varying the growth parameters and passivation methods were investigated with electron microscopy and photoluminescence measurements. The passivation methods included GaAs/AlGaAs and GaAs/GaAsP core-shell nanowires and ALD passivation. The work was conducted in Nanotechnology research group in Micronova facilities of Aalto University.

Chapter 2 reviews theory on compound semiconductors and their growth, with focus on VLS growth and effects of different growth parameters. Chapter 2 reviews also

theory on surface states and their passivation. Chapter 3 presents the used equipment and their operational principles. Also sample preparation and characterization methods are presented. Chapter 4 presents the results with different sample preparations, growth parameters and passivation methods. Conclusions drawn from the results are presented in chapter 5.

2. Theory on GaAs nanowires

2.1. III-V semiconductor materials

Compound semiconductors include elements from different materials. Binary compounds are the simplest ones consisting of two basic elements, and they act as a basis for more complicated compounds. In a crystalline form, they have equal amount of the two elements. Practically all of the binary compounds used in technology have a total of eight valence electrons (same total amount as in silicon). The binary compounds contain elements from either groups III and V (III-V compounds) or groups II and VI (II-VI compounds). Binary compound GaAs is on emphasis in this thesis.

Ternary compounds are similar to binary, with a proportion of one element replaced with another from the same group. For example, considering $In_xGa_{1-x}As$, where x goes from zero to unity, part of the group III slots are occupied with In and the rest with Ga, whereas all of the group V slots contain As. Many physical properties of compound semiconductors can be modified by varying the proportions of the elements.

The elements are bound with covalent tetrahedral bonds, as well as weaker ionic bonds, forming a crystal structure [8 p. 4-7]. The structure in III-V materials is typically zinc blende (ZB) [8 p. 4-7], whereas nanowires exhibit both wurtzite (WZ) and ZB phases [9] [10]. In bulk materials the WZ structure is found in compound semiconductors with high ionicity [8 p. 4-7], but in nanowires the resulting structure depends on nucleation conditions [10]. ZB and WZ structures are presented in figure 1.

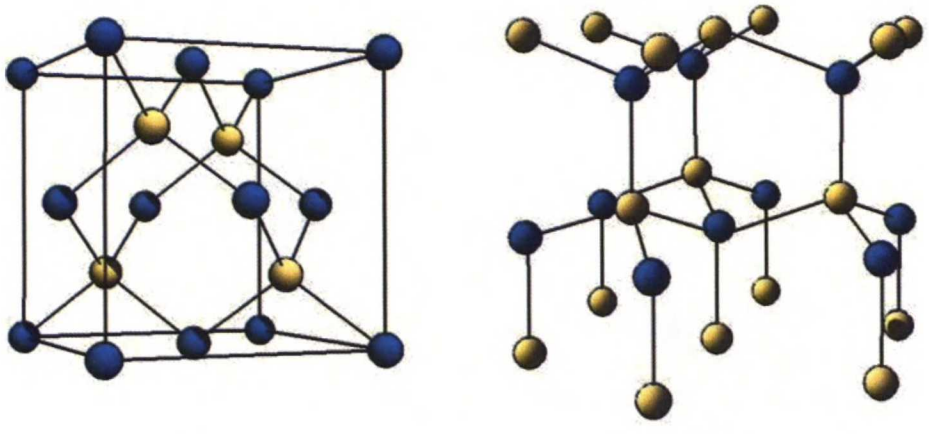

Figure 1: ZB (a) and WZ (b) crystal structures. Yellow and blue balls represent elements from different groups.

A *unit cell* is the smallest unit that describes atomic arrangement of a crystal. For example, figure 1a presents the ZB unit cell. Separation between unit cells in a crystal is referred to as *lattice constant*, and each material composition has a specific lattice constant. For binary compounds it is fixed, and for ternary compounds it can be calculated with Vegard's law [11]:

$$a_{A_xB_{1-x}C} = xa_{AC} + (1-x)a_{BC} \quad (1)$$

where a is the lattice constant, x is between zero and unity, and A, B and C denote different materials in the compound. The Vegard's law applies to many other physical parameters as well. Lattice constant is a crucial parameter regarding heteroepitaxial growth of semiconductors, which will be discussed in more detail in chapter 2.2. For GaAs, AlAs and GaP it has values a_{GaAs} = 5.653 Å + 3.88 × 10^{-5} (T-300) Å/K, a_{AlAs} = 5.661 Å + 2.90 × 10^{-5} (T-300) Å/K and a_{GaP} = 5.451 Å + 2.92 × 10^{-5} (T-300) Å/K, respectively [12].

In a crystal atoms are brought close together, thus lowering the potential barrier for electrons between the atoms, which in turn causes electron orbits to overlap and allows electrons to move between atoms. This overlapping causes discrete energy levels of electrons to spread to wide energy bands. In a semiconductor two bands, the valence band and the conduction band are separated with a forbidden energy gap where no energy levels are available for electrons. The valence band has its energy levels below the band gap, and all of its available states are occupied by electrons at 0 K. The conduction band is the first band above the band gap and it is empty at 0 K. At higher temperature electrons start to move to the conduction band due to thermal effects, although the effect remains small at room temperature. [13 p. 79-83]

The most important locations in the band structure are the valence band maximum and the conduction band minimum, because most of the charge carriers are situated in their proximity and electron transitions typically occur between them. Transitions are typically initiated by absorption or emission of a photon. When a material has the valence band maximum and the conduction band minimum at the same position in **k**-vector space (or wave vector space), the material is referred to as a direct band gap material (figure 2a), and when the positions differ, the band gap is indirect (figure 2b). [13 p. 109-110]

When an electron in a direct band gap material absorbs a photon with energy larger than the band gap, the electron transits from the valence band to the conduction band, leaving a hole behind. On the other hand, in case of indirect band gap, the electron needs to change its k-value as well, which happens via simultaneous phonon absorption or emission. This leads to considerably decreased transition probability. Transitions between the two types of band gaps are presented in figures 2a and 2b. Similarly, when the electron recombines and returns to the valence band, a photon with energy equal to band gap is emitted.

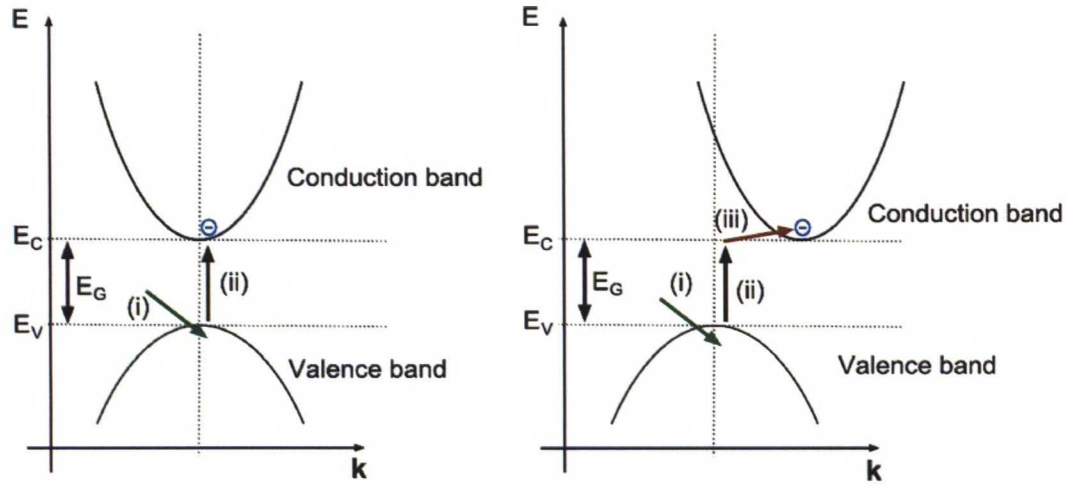

Figure 2: Simplified band structure and photonic electron excitation of (a) direct band gap and (b) indirect band gap material. E_C and E_V denote the conduction band minimum and the valence band maximum, respectively. E_G is the band gap and **k** denotes the wave vector. Green arrow (i) is an arriving photon, black arrow (ii) is an electron excited by the photon and brown arrow (iii) denotes absorption of a phonon by the electron.

In reality there are numerous conduction band minima, which correspond to different positions in the first Brillouin zone. The first Brillouin zone is the smallest cell that describes a crystal lattice. In band diagram they are referred to as Γ, X, and L-valleys, of which the Γ-valley is located in the center of the Brillouin zone and has zero **k**-value. Thus, direct band gap materials have lowest conduction band minimum at the Γ-valley.

Both direct and indirect band gap energies depend on temperature, and the values are given by the empirical Varshni form:

$$E_G^i(T) = E_G^i(T=0) - \frac{\alpha_V^i T^2}{T+\beta_V^i}, \tag{2}$$

where α_V^i and β_V^i are material dependent Varshni parameters related to valley *i*. Table 1 presents the GaAs, AlAs, GaP [12] and $Al_xGa_{1-x}As$ [14 p. 160] band gaps at 0 K in Γ- and X-valleys and corresponding Varshni parameters, except for the GaP Γ-valley. This value is given in eV by equation (3). [12]

$$E_{G,GaP}^{\Gamma} = 2.886 + 0.1081 \times \left[1 - coth\left(\frac{164}{T}\right)\right]. \tag{3}$$

Table 1: Lowest-energy band gaps at 0 K and corresponding Varshni parameters for GaAs, AlAs, GaP [12] and $Al_xGa_{1-x}As$ [14 p. 160]

	GaAs	GaAs	AlAs	AlAs	GaP	GaP	$Al_xGa_{1-x}As$	$Al_xGa_{1-x}As$
Valley	Γ-valley	X-valley	Γ-valley	X-valley	Γ-valley	X-valley	Γ-valley	X-valley
E_G **(eV)**	1.519	1.981	3.099	2.24	eq. (3)	2.35	1.513 +1.380x	1.99 + 1.027x + 0.055x^2
α_V **(meV/K)**	0.5405	0.460	0.885	0.7	-	0.5771	5.8 + 3.6x	4.6 – 1.0x
β_V **(K)**	204	204	530	530	-	372	206 + 123x	204

For ternary alloys, the band gap can be calculated from the band gaps of its binary compounds with a simple quadratic form:

$$E_G(A_{1-x}B_x) = (1-x)E_G(A) + xE_G(B) - x(1-x)\xi, \quad (4)$$

where A and B are the binary alloys and ξ is the bowing parameter, which accounts to deviation from a linear interpolation between the two binary alloys. This parameter is $\xi^{\Gamma}_{AlGaAs} = -0.127 + 1.310x$ and $\xi^{X}_{AlGaAs} = 0.055$ for $Al_xGa_{1-x}As$ Γ- and X-valleys, respectively, and $\xi^{\Gamma}_{GaAsP} = 0.19$ and $\xi^{X}_{GaAsP} = 0.24$ for $GaAs_{1-x}P_x$ Γ- and X-valleys, respectively. [12] The lowest-energy band gap in $Al_xGa_{1-x}As$ transits from the Γ- valley to the X-valley at x = 0.38 - 0.40, depending on the temperature, [14 p. 158] and in $GaAs_{1-x}P_x$ at x = 0.45 [12].

Crystal defects and foreign impurities create allowed energy levels within the forbidden band gap. Such levels are referred to as *trap states* or simply *traps.* They are essentially disturbances in a periodic potential of a crystal structure that allow electrons to recombine nonradiatively, thereby deteriorating the performance of optical devices. Traps are divided to two different types: deep traps and shallow traps, as shown in figure 3. Figure 3 also presents periodic potential of a defect-free crystal. Especially deep traps are harmful in most of semiconductor applications due to their efficient trapping of charge carriers [15 p. 102]. In case of nanowires, defects at the crystal surface are especially detrimental, because of the high surface-to-volume ratio. Surface defects are discussed in chapter 2.5.1.

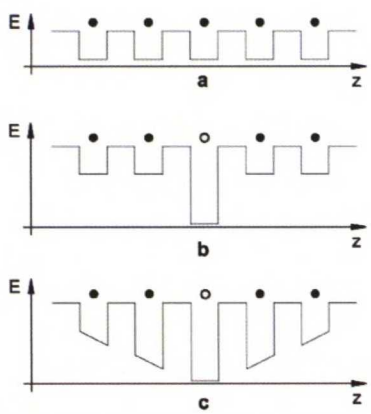

Figure 3: Periodic potential of a crystal structure (a), a deep trap (b) and a shallow trap (c). Black dots represent atoms and white dots defects.

Conduction and valence bands are situated at different energy levels in different semiconductors. Therefore, the bands form steps at a junction of two semiconductors. The junction is denoted type I, when one of the materials has its band gap within the band gap of the other material, *i.e.* one of the materials has the lowest conduction band minimum and the highest valence band maximum. In type II junction, band gaps overlap only partially. One of the materials has then the lowest conduction band minimum, and the other material has the highest valence band maximum. Figure 4 shows band diagrams of the two types of junctions, as well as behavior of charge carriers near the junction. Electrons are situated in the lowest conduction band minimum, and holes in the highest valence band maximum. In type II junction electrons and holes travel to different sides of the junction and accumulate in its vicinity due to electrical attraction.

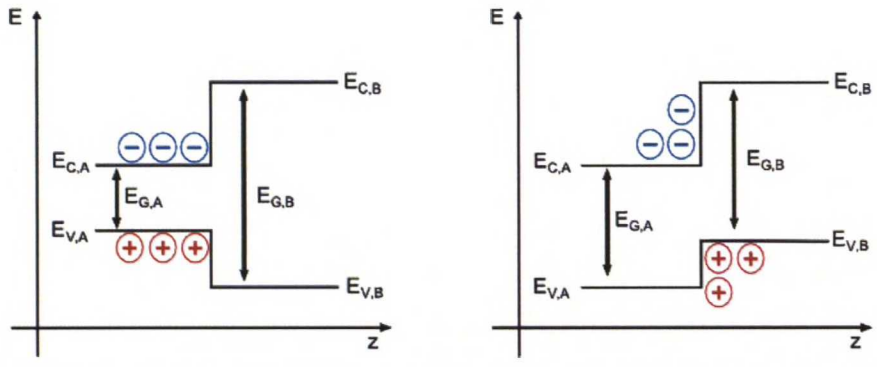

Figure 4: Semiconductor junction types I (left) and II (right). Subindexes A and B denote different materials in the junction. Electrons (blue) are situated at the conduction band minimum, and holes (red) at the valence band maximum. In type II junction they attract each other.

In this work, GaAs/$Al_xGa_{1-x}As$ nanowire (NW) junctions were studied. The materials have junction type I, and the offsets in the conduction band (ΔE_C) in eV is given for $x \leq 0.8$ by [14 p. 278]

$$\Delta E_C^{\Gamma}(x) = 0.85x \tag{5}$$

for the Γ - valley, and

$$\Delta E_C^{X}(x) = 0.48 - 0.30x \tag{6}$$

for the X -valley. The offset in the valence band (ΔE_V) in eV is given by

$$\Delta E_V(x) = 0.50x. \text{ [14 p. 278]} \tag{7}$$

2.2. Epitaxial growth

Epitaxial growth is a delicate process, where a single crystalline material is deposited on a single crystalline substrate. The substrate crystal then affects orientation and structure of the growing crystal. Epitaxy was first performed from liquid phase, supersaturated melt, from which crystalline material was precipitated. This technique named *liquid phase epitaxy (LPE)* is still commonly used due to its simplicity. When a supersaturated vapor is used instead of liquids, the epitaxial process is termed *vapor phase epitaxy (VPE).* This is the most versatile technique, allowing numerous different materials to be used, either as pure vapors or as vapor-phase precursor materials. Another advantage of VPE is the controllability of the growth process. MOVPE is a VPE technique which uses metalorganic precursor materials, and is used to prepare all samples in this thesis. MOVPE will be explained in more detail in chapter 4.1. Another popular epitaxial technique *molecular beam epitaxy (MBE)* uses elemental or molecular beams of material in a high vacuum. [16 p. 10-11]

Regardless the growth process, crystal growth is driven by thermodynamics. Thermodynamics also determines the parameter range for successful growth, since the growth only occurs when a difference in chemical potential exists between the precursors and the product material. The chemical potential difference can be achieved by a constant supply of precursor materials, as is the case in VPE. The potential difference for a one-component system can be calculated with [16 p. 9-10]

$$\Delta\mu_{vs} = \mu_v - \mu_s = k_B T \ln\left(\frac{p_v}{p_{v0}}\right), \tag{8}$$

where $\Delta\mu_{vs}$ is the chemical potential difference between the vapor and the substrate, μ_v and μ_s refer to the chemical potential of the vapor and the substrate, respectively, k_B is the Boltzmann constant, T is temperature, p_v is the partial pressure of the growth component in the vapor phase and p_{v0} is the equilibrium partial vapor pressure of the component over the crystalline phase in the given conditions. It is noteworthy that when growing binary or ternary compounds, the process becomes more complicated, since the potential difference between the vapor and crystal is determined by the two gaseous materials [16 p. 9, 23]. As the chemical potential difference is a prerequisite for crystal growth, it is clear from equation (8) that p_p must be over p_{p0} in order for growth to occur. Thus a constant supply of precursors is required. The difference in chemical potential must be sufficiently large for a given growth process, thus temperature needs to be sufficiently high as well. On the other hand, at too high temperatures the deposited atoms have insufficient time to find stable locations [17 p. 71], and the subsequently growing crystal becomes defected. Therefore, the temperature has to be chosen from an appropriate range for each process.

The deposition can be performed either on similar or dissimilar material as the growing crystal. In case both deposited and the substrate materials are the same, the process is referred to as *homoepitaxy*. Figure 5a presents a lattice-matched layer deposition, as is the case with homoepitaxy. Homoepitaxial growth progresses principally layer by layer and can be infinitely long. When the growing crystal and the substrate are dissimilar, the process is termed *heteroepitaxy*. Heteroepitaxial layers are strained in most cases, as different materials rarely have similar lattice constants.

When thin layers conform to the substrate and remain defect-free, they are termed *pseudomorphic* layers. Figure 5b presents such layer with biaxial compressive strain. [18 p. 65-67] The strain is compressive when the deposited layer has higher lattice constant than the substrate and tensile when it is lower. Due to the elasticity of the semiconductor materials, lattice constant perpendicular to the substrate surface changes as well. The strain also changes the band gap and the effective masses of charge carriers. Above *critical thickness* strain energy exceeds chemical energy of dislocations, and a defected crystal becomes energetically more favorable than elastic deformation, leading to a poorer crystal quality. [11 p. 5, 22-29] The crystal quality deteriorates with increasing defect density, which in turn increases with layer thickness and lattice mismatch [18 p. 65-67]. In addition to thin 2D layers, defect-free structures can also be obtained by keeping lateral dimensions small, as is done with nanowires. Like the thin layers have to be sufficiently thin, the nanowires need to have sufficiently small diameters to conform elastically to the underlying substrate. Nevertheless, the diameter can be about a magnitude higher than the critical thickness of a thin film of the same material [19]. Thus, nanowires can overcome some limitations of lattice mismatch, which is one reason why they are promising in many device applications.

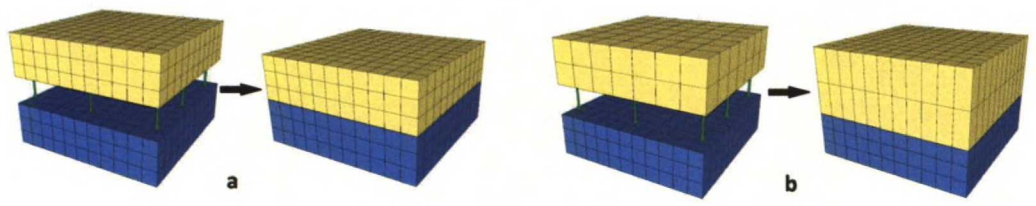

Figure 5: Epitaxy of (a) lattice matched and (b) lattice mismatched layers. In case of lattice matched epitaxy, the layers can be theoretically infinitely thick. In lattice mismatched epitaxy the layers conform until critical thickness, after which they become defected.

Figure 6 presents various processes occurring during epitaxial growth as follows. Growth process starts with atoms arriving at a substrate surface (1) and forming bonds with it. The adsorbed atoms are termed *adatoms*. After adsorption the adatoms may diffuse along the surface (2), take a previously occupied site of a substrate atom (atom exchange) (3), or evaporate back to atmosphere (desorption) (4). It is energetically favorable for the adatoms to place themselves at kinks (5), surface defects, or in groups of adatoms (island growth) (6), where they have more neighboring atoms than on a flat surface, and thus more bonds and less surface energy. Therefore, they diffuse along the surface until they evaporate or find a stable position, which can be either in the substrate or in an already grown layer.

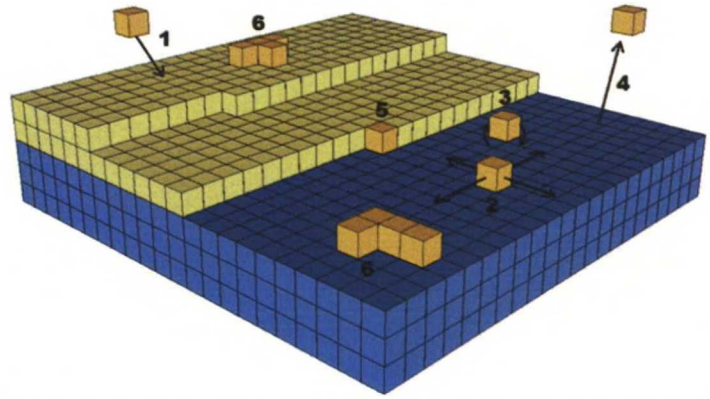

Figure 6: Various surface processes: (1) adsorption, (2) diffusion along the surface, (3) atom exchange, (4) desorption, (5) binding at a kink and (6) island formation. Substrate is marked with blue, grown epitaxial layers with yellow and atoms taking part in the process with orange.

The diffusion and desorption processes are thermally activated and the frequency of a process *i* depends on temperature with: [20 p. 11]

$$f_i = f_0 e^{-E_i/k_B T}, \tag{9}$$

where f_i is the frequency of the process i, f_0 is the cutoff frequency and E_i is the activation energy of the process. Diffusion constant can be calculated with: [20 p. 12]

$$D = {\lambda_n}^2 f_{diff} = \lambda^2 f_0 e^{-E_{diff}/k_B T}, \tag{10}$$

where λ_n is the distance between two nucleation sites, f_{diff} is diffusion frequency, and E_{diff} is the average activation energy for diffusion. Combining equations (9) and (10) we get a formula for diffusion length: [20]

$$\lambda_{diff} = \left(\frac{D}{f_{des}}\right)^{\frac{1}{2}} = \lambda_n e^{-E_{diff}-E_{des}/2k_B T}, \tag{11}$$

where f_{des} is the desorption frequency (from eq. 9) and E_{des} is the desorption activation energy. From equation (11) we see that diffusion length increases with temperature. E_{diff} and E_{des} depend on the materials taking part in the process; hence, the diffusion length depends on the diffusing material and on the surface. λ_{diff} for a Ga adatom on GaAs surface is typically less than 2 µm [21].

When III-V semiconductors are deposited, two materials are participating in the process. Adatoms from different groups can then nucleate with each other and alter effective λ_n. The nucleated pair can also diffuse along the surface and further complicate the situation. Additionally, adatoms from the same group can collide. When concentration of an element increases, also probability of collisions between adatoms of that element become more frequent. Thus, increased concentration decreases the mean

free path and the diffusion length. Therefore, molar ratio of the elements affects the diffusion length.

In case of ternary compounds, proportions of the elements depend on the molar flows of the precursors. Molar flows of group V precursors are typically in excess when III-V materials are grown in MOVPE. Thus when ternary compound with two different group III elements ($A_x^{III}B_{1-x}^{III}C^{V}$) is grown, group III growth is expected to be mass-transport limited with

$$x_A = \frac{F_A}{F_A+F_B}, \tag{12}$$

where x_A is the group III proportion of the material A in the grown layer, and F_A and F_B are molar flows of group III precursors A and B, respectively. In case of ternary material with two different group V elements ($A^{III}C_{1-x}^{V}D_x^{V}$) is grown, both of the precursors are typically in excess. Thus, the group V related growth is not mass-transport limited, and the proportion of the elements in resulting material depend on relative bond strengths of the constituting binary alloys and equation (12) needs to be corrected with a distribution coefficient: [22 p. 18]

$$x_D = \frac{KF_D}{KF_D+F_C}, \tag{13}$$

where x_D is the group V proportion of the material D in the grown layer, K is the distribution coefficient, and F_C and F_D are molar flows of group V precursors C and D, respectively.

Surface defects and surface impurities, such as native oxide, can be detrimental to the delicate epitaxial growth [18]. For example, amorphous native oxide can offer a stable site for the atoms arriving to the surface. As the atoms mimic the crystal structure of the underlying material, a layer grown on native oxide then becomes amorphous as well, or polycrystalline in some cases. Similar effects arise from other surface defects as well, possibly ruining the epitaxial process [18].

2.3. Vapor-Liquid-Solid growth mechanism

2.3.1. Principle of particle-assisted vapor-liquid-solid growth

VLS is a special case of crystal growth, which uses pre-deposited seeds to initiate growth in selective areas. In many cases VLS is used to perform epitaxial growth, as is the case in this thesis. The growth occurs only via seeds, allowing one-dimensional crystal growth and fabrication of nanowires. Material is constantly introduced to the seed supersaturating it, which causes the seed to precipitate the introduced material. In the process the seed is lifted, thus forming a column-like crystal underneath.

Different techniques for VLS growth include MBE [23] [24], CVD [25] and MOVPE [26] [27] [28] [29] [30]. In this thesis a MOVPE system was used and the following section describes processes in MOVPE unless stated otherwise. Besides different techniques, the seeds can be of different nature. The growth process is termed either (i) *catalyzed* or (ii) *non-catalyzed*, according to the seed deposition method.

Regardless the seed type, the base diameter of the growing column is determined by size of the seed.

In catalyzed growth, foreign seed particles, typically metals [16 p. 15], are deposited on the substrate prior to growth. Especially gold has been used widely ([16] [26] [27] [28] [29] [30]), due to good solubility of many group III elements to gold at typical growth temperatures [28] [31 p. 3]. However, since Au acts as a deep-level impurity in silicon, also other seed materials, such as copper [25] [32] and iron [33], have been investigated. The term "catalyzed" is misleading, since although the seed particle is not consumed in the process [16 p. 15], it is rarely catalytic in the sense that activation energies of the chemical reactions in the process remain unchanged in most cases [31 p. 3-4]. Instead, the particle effectively collects the deposited material [28], which leads to VLS growth that is described in more detail in chapter 2.3.3. The particles are typically deposited either from aerosol or colloid solution, or they can be formed from a thin film by annealing [34 p. 54]. In this work all samples were prepared using Au seeds deposited from gold solution.

Catalyst-free growth is typically realized by *in-situ* growth of small metallic droplets before the nanowire VLS growth. The droplets then act as seeds for the growth, much like the pre-deposited particles described above. The method is commonly used to grow binary compound nanowires with a droplet of one of the elements in the growing crystal. [31 p. 5-6] For example, In droplets have been used to grow InP nanowires in MOVPE [35] [36] and Ga droplets have been used to grow GaAs nanowires with MBE [23]. Also catalyst-free GaAs nanoneedle growth with MOVPE has been reported [37]. Thus the catalyst-free growth offers a method to avoid possible contamination from foreign atoms diffused from the seed particle.

Figure 7 shows the basic principle of catalyzed one-component VLS nanowire growth. The particle is first deposited on a substrate, and the system is heated to growth temperatures. At this point an alloy is formed between the particle and the substrate (figure 7a). When the desired growth temperature is reached, precursor materials are introduced to the reactor and the introduced material is incorporated to the seed particle (figure 7b). With a constant supply of precursor materials, the particle becomes supersaturated and precipitates the introduced material, thus forming a crystal underneath (figure 7c).

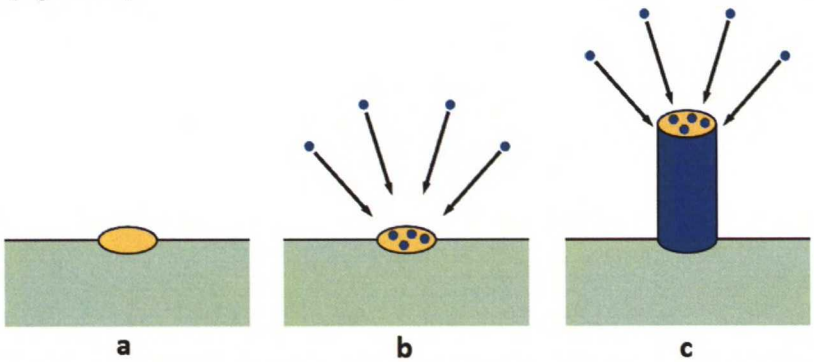

Figure 7: Principle of particle-assisted VLS growth. The seed particle (yellow) is placed on a substrate (green), and the system is heated to growth temperature (a). Either precursor materials in MOVPE or beams of elemental material in MBE (blue dots) are introduced to the particle, leading to supersaturation (b). The particle precipitates the material and forms a nanowire while material supply is preserved (c).

2.3.2. Substrate orientation and stacking defects in VLS

The surface properties of substrate affect the crystal formation during the growth process so that the growing crystal tends to orientate itself to the crystalline direction with lowest free energy. For the typical zinc blende structure in III-V and II-VI compound semiconductors, the direction is {111}B [31 p. 4-5]. As the nanowires grow to this direction, it is possible to grow highly oriented vertical nanowires on a substrate with {111}B direction, whereas other crystalline directions have proven problematic.

However, even in the lowest-energy direction, the crystal structure in a growing nanowire is seldom perfect. The ZB structure consists of three alternating layers, *A, B* and *C,* forming a structure: *ABCABCABC* ..., as shown in figure 8a. Changing the sequence to $AB\overline{A}\overline{B}\overline{C}\ \overline{A}\overline{B}\overline{C}$ ... (fig. 8b) requires little energy, and hence this type of faults is common in nanowires. The described fault is termed here *twin plane* or *twin fault.* If the twin planes occur subsequently, it turns the crystal structure to wurtzite: *ABABAB* ..., as shown in figure 8c. [31 p. 5] Similarly, thin sections of ZB can emerge in the WZ structure, reducing the crystal quality [9] [10]. The structure is then *ABABCBABA*... [10] and the defect is termed here *stacking fault.* Superordinate for twin plane and stacking fault is *stacking defect* in this work.

ZB and WZ structured nanowires have different band structures, which causes issues in optical applications. Similarly for electronic applications, stacking defects act as scattering centers for electrons, degrading performance. [10] Twin planes have been proposed to emerge due to distortions in the seed particle shape; the distortions in turn result from nucleation in different crystal orientations at vapor-liquid-solid trijunction. Density of twin planes and thus the nanowire crystal structure can be controlled with basic growth parameters, temperature and molar ratio, possibly resulting in either pure ZB or WZ nanowires. [9] Other proposed mechanisms for stacking defect formation are small fluctuations in the growth system, such as thermal and mass transport fluctuations. [10]

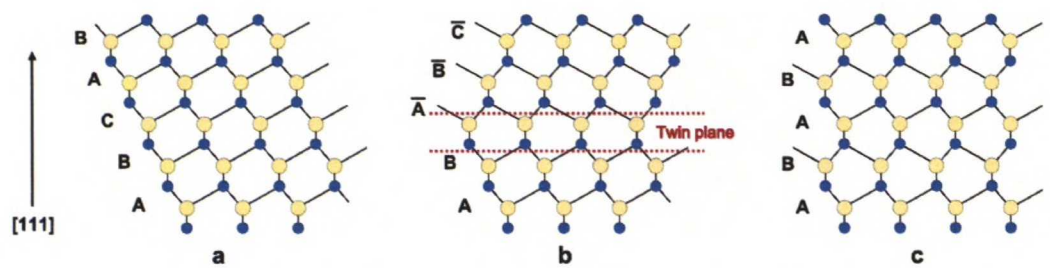

Figure 8: Planar projections of ZB structure (a), ZB structure with a twin plane (b) and WZ structure (c). The alternating layers are denoted *A, B* and *C*, with [111] direction upwards to the direction of the alternating layers, and after twinning the respective layers are denoted $\overline{A}$, $\overline{B}$, and $\overline{C}$. WZ structure in (c) is essentially formed from consecutive twin plane formations from ZB.

2.3.3. Thermodynamic, kinetic and physical processes in the particle-assisted VLS growth

Nanowire growth occurs when the adatoms reach the interface between the seed particle and the substrate, and nucleate there. From thermodynamic considerations and according to equation 2, the chemical potential of a given atom must be higher in vapor phase than in crystal in order to enable crystal growth. If the atoms first diffuse to the seed particle and then to the crystal, thermodynamically it suggests that the chemical potential in the seed particle is between those in the vapor and the crystal, as figure 9 shows. However, in this case the potential difference between the vapor and the crystal would be higher than between the seed particle and the crystal. Thus, if only thermodynamic aspects are considered, the growth would occur faster directly from the vapor than from the seed particle [16 p. 22].

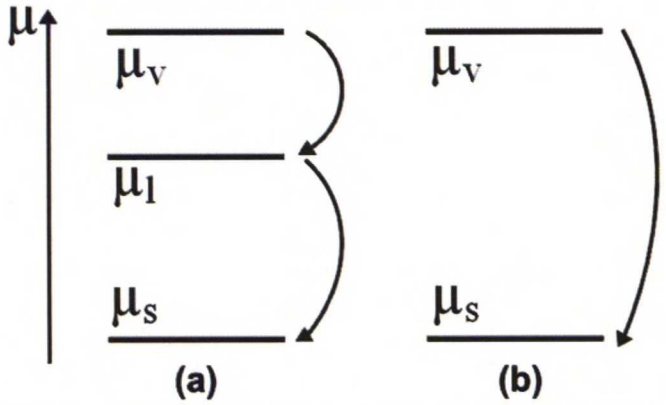

Figure 9: Incorporation of an element from vapor phase (μ_v) to solid crystal phase (μ_s) via liquid seed particle (μ_l) (a) and directly (b). Arrows on right represent the stepwise process.

In the thermodynamic considerations above, conditions in the system are assumed to be uniform. On the other hand, if concentrations of reactant materials would be higher around the seed particle, it could lead to locally increased chemical potential around the particle, and thus in the particle as well. [16 p. 22] The intuitive explanation would be that the seed particle acts as a catalyst. Different groups have obtained controversial results for changes in activation energy with the use of a seed particle. For example, the activation energy has been found reduced for Si nanowires grown in MOVPE [38], but other groups have deduced it unchanged in a similar system [28]. For GaAs nanowires, different groups have found the activation energy to remain unchanged [28] [39], namely 67-75 kJ/mol for nanowires compared to 67 kJ/mol for planar film growth [28], but also a lowered activation energy of 57 kJ/mol has been reported [29]. It should be noted that determining appropriate activation energy for comparison is not trivial, since the energy may be affected by the materials present, growth conditions and the vicinity of the substrate surface. In general, the seed particle may have catalyzing effect in some cases, but it does not suffice to explain the mechanism behind VLS growth. [16 p. 24]

In MOVPE, the increased reactant concentration could be a consequence of enhanced decomposition rate of precursor molecules in the vicinity of the seed particle. This could be due to higher accommodation probability of the precursors of the liquid, although it is not clear whether liquids have higher accommodation probability than solid surfaces. Nevertheless, for Si, it is often assumed that enhanced concentration leads to the VLS growth. [40 p. 151-152] It is clear, though, that the enhanced decomposition rate is not enough to explain the VLS growth process, as nanowires can also be grown with MBE [23] [24].

As the thermodynamic and kinetic reasoning does not suffice to explain the growth process, also physical surface processes must have an important role [16 p. 25] [28] [31 p. 3]. Instead, as noted earlier, the particle has been proposed to act as a sink for the reactant materials. For MOVPE, Johansson *et al.* have suggested that since the nanowire growth occurs at temperatures where planar film growth is kinetically hindered, the decomposition products diffuse along the surface to the metal seeds. With constant supply of the products, the atmosphere in the vicinity of the seed soon becomes supersaturated. As many group III elements, including Ga, readily dissolve in Au at typical growth temperatures, the Au particle effectively gathers the group III adatoms diffusing along the surface, becoming supersaturated itself and initiating wire growth. [28]

This explanation is supported by the processes undertaken by adatoms that were described in chapter 2.2. When the adatoms are not incorporated to the substrate as an epitaxial film, majority of them diffuse along the surface or evaporates back to the ambient atmosphere. On the other hand, the evaporated adatoms increase their partial pressure in the atmosphere, and they may be adsorbed back to the surface as well. In any case, they either eventually diffuse to a metal particle or increase the partial pressure in the atmosphere until blown out of the reactor. Enhanced partial pressure increases the chemical potential in vapor phase, which leads to higher dissolving rate of adatoms to the seeds.

2.3.4. Supersaturation, precipitation and crystal growth

Regardless the means by which the decomposition products reach the seed particle, the processes undertaken in supersaturation and nucleation of the growing crystal are the same. Considering the seed particle, in a simple case it forms a binary system, such as Au-Si when Si nanowires are grown. The Au-Si system is a simple eutectic system, and its phase diagram is presented in figure 10. In VLS process, the percentage of Si is first increased to thermodynamically unstable amount in a Au particle under constant temperature, as denoted with an arrow from node A to B in figure 10. In other words, the particle becomes supersaturated due to the reasons discussed in the previous chapter. The supersaturation occurs when the amount of Si exceeds the liquidus line, *i.e.* the line between areas 2 and 3 in figure 10. The system has a tendency to return to the liquidus concentration; hence the particle precipitates Si in order to lower the concentration, as shown with an arrow from node B to C in figure 10. However, if the particle is constantly supplied with Si, it remains supersaturated, constantly precipitating Si and forming a crystal underneath itself.

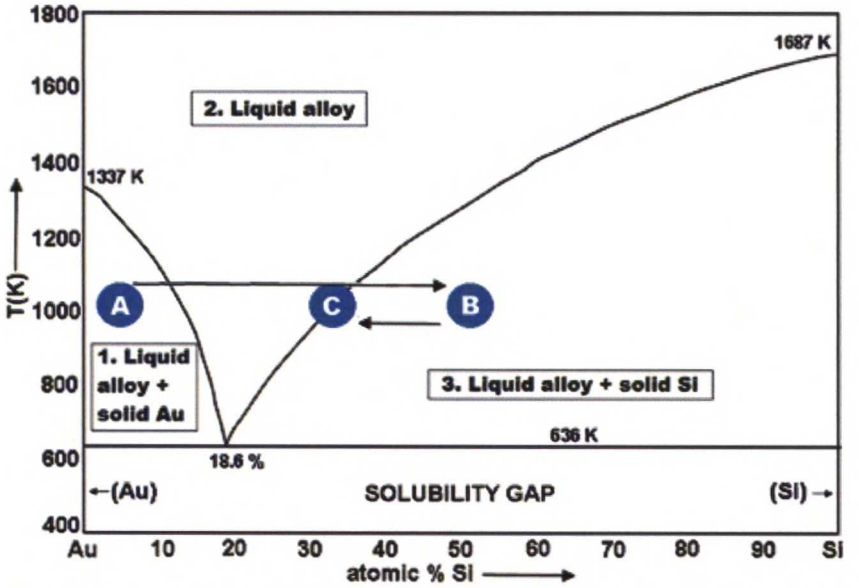

Figure 10: Au-Si phase diagram and principle of VLS process. In the beginning of VLS growth, Si percentage in the seed is low (A), and is increased over the liquidus line by continuous supply of Si (B), causing precipitation of Si from the seed until liquidus composition is reached again (C). The figure is modified from [16].

Considering growth of III-V compound semiconductors, the process is again more complicated, although only one of the elements dissolves to the particle in relevant temperatures, and thus only binary alloys need to be considered. Normally the dissolved element is from group III, for example Ga in GaAs. However, Au-Ga system forms numerous different compounds with melting points between those of Au and Ga. The different compounds have several separate eutectic points, but it is unclear whether they lead to growth of binary III-V compounds. [16 p. 23-24, 62] Furthermore, Harmand *et al.*concluded that Ga concentration in Au had been over 25 % in their system, and that the concentration corresponds to liquid phase of the Au-Ga system at relevant temperatures [41]. This also indicates that the explanation given for growth of Si nanowires from Au-Si system described above does not suffice to explain growth of III-V compounds.

Another important question is how the group V material reaches the interface between the particle and the crystal, where the growth occurs. It has been explained that the growth of a nanowire proceeds stepwise one atomic bilayer at a time, with each bilayer consisting of III-V pairs. Nucleation takes place at the trijunction of the vapor, seed particle and crystal, from where the layer growth propagates across the particle-crystal interface. [9] Ga is provided to the growth location directly from the seed particle, and As could reach the location by traveling along the growth interface, or along grain boundaries, in case the seed particle is solid. [16 p. 23]

Concentrations of the elements in the vapor phase and in the seed dictate the difference in chemical potential between the phases. Thus the chemical potential difference is a measure of supersaturation, and the terms can be used interchangeably [9]. Formula for the chemical potential difference in a two-component system resembles that of one-component:

$$\Delta\mu_c = kT \ln \frac{C_{III} C_V}{C_{III,eq} C_{V,eq}}, \quad (14)$$

where $\Delta\mu_c$ is the combined chemical potential difference for both elements, C_{III} and C_V are concentrations of the group III and V elements, respectively, during the growth; $C_{III,eq}$ and $C_{V,eq}$ are concentrations of the group III and V elements, respectively, at equilibrium with the crystalline phase. [9] As described earlier, group III element forms an alloy with the seed particle, and group V element nucleates directly from the vapor phase. Thus, C_{III} and $C_{III,eq}$ refer to the group III element in the alloy, and C_V and $C_{V,eq}$ refer to the group V element in vapor phase.

Figure 11 sums up the processes occurring during the nanowire growth. The arriving atoms can land on three different surfaces: the seed particle, the nanowire and the substrate. In each case the process starts with mass transport from the vapor phase (1) [42], and on the seed particle surface it can be followed by the diffusion of arriving atoms to the liquid seed particle (2). The seed particle becomes eventually supersaturated, and the adatoms diffuse to the interface between the particle and nanowire (3) [42], since it is the easiest site for them to nucleate. If the particle is solid, process (3) denotes adatom traveling via grain boundaries or along the growth interface. Finally the atoms nucleate (4) and become incorporated in the nanowire [42].

The adatoms may land on the nanowire surface as well. In case the point of arrival is within diffusion length from the seed particle, the adatoms diffuse to the growth interface or to the seed particle (5) [30]. Shortly after nanowire nucleation, the adatoms can diffuse from substrate to the growth area as well. When the distance from point of arrival to the seed particle is greater than diffusion length, it can either re-evaporate (6) or nucleate on the surface (7), the latter resulting in planar film growth [42]. As nucleation is a thermally activated process, planar growth becomes more significant in high temperatures. The re-evaporation or film growth can occur also on the substrate surface (8) [42].

It is intuitive to think that, as the group V atoms reach the growth interface without forming an alloy with the seed particle, their preferred path is via diffusion along the surface. This would imply that diffusion length on the nanowire surface affects the proportion of group V atoms reaching the interface, and thus effective molar ratio would vary with the diffusion length. Effective molar ratio also depends on cracking of precursor materials in MOVPE [40 p. 159]. Another noteworthy point is that in case of heteroepitaxy, some atoms from the substrate diffuse to the base of the wire, which can affect the nanowire properties in some cases.

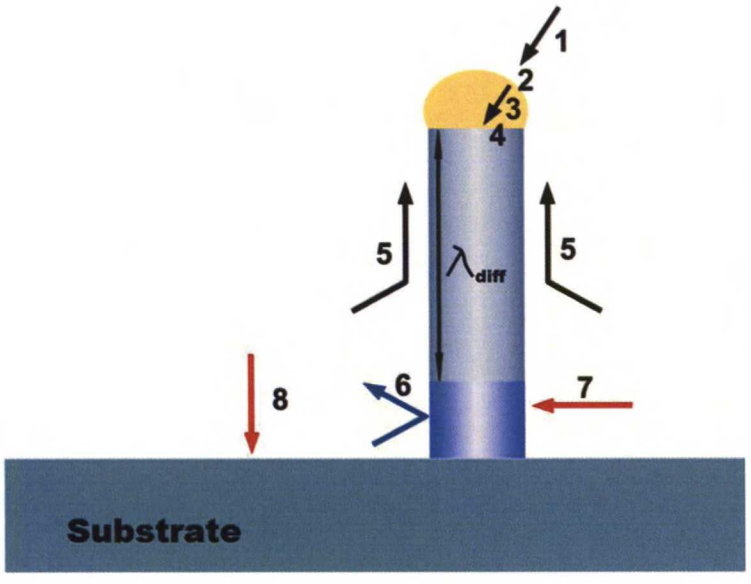

Figure 11: Processes undergone by incoming atoms in nanowire growth: mass transport (1), impingement or diffusion (2), diffusion or travel through the seed particle (3), nucleation at liquid-solid interface (4), adsorption and diffusion to the seed particle (5), evaporation back to atmosphere (6), sidewall growth (7) and planar growth on the substrate (8). Red arrows indicate processes that are significant in high temperatures, and blue arrow processes dominates in moderate temperatures.

Planar GaAs growth with TMG and arsine (AsH_3) has been observed to be limited by reaction rate up to 550 °C, after which it is mass transport limited. NWs are most often grown at temperatures below 550 °C, thus, the NW growth is reaction rate limited unless the seed particle acts as a catalyst, lowering the temperature where all of the reactants are used in the process. [40 p. 160] As noted earlier, there are controversial results about activation energies in VLS growth, and therefore the limiting process is unclear as well. Besides activation energy considerations, Joyce *et al.*observed reduced tapering with faster growth rates, indicating their process to have been mass transport limited [43].

Although the VLS method is widely accepted, in some cases the particle being liquid during growth is arguable. In addition to VLS, the nanowire growth has been reported to occur also by vapor-solid-solid (VSS) method [25] [44] [45]. On the other hand, differentiating between solid and liquid nanoparticles (NP) is not always trivial, as NPs have been reported to reshape at low temperatures, indicating very high mobility of the atoms [16 p. 25]. Moreover, the state of the particle has been reported to depend on pressure and thermal history for the Au-Ga system [46]. Pressure affecting the phase of alloys can be considered as a general phenomenon, whereas hysteresis in melting and freezing may occur only in few alloys. With the Au-Ga alloy, nanowire growth was possible with the particle both in solid or liquid state [46], although the growth is not always possible with the particle in both of the states [45]. Nevertheless, it can be concluded that both VLS and VSS are very similar and valid mechanisms for nanowire growth [16 p. 27].

2.3.5. Growth rate, kinking and crawling

Regardless the state of the particle, a proportion of nanowires commonly kink or crawl (*i.e.* grow along the surface), especially with heteroepitaxy. During the growth, the growing nanowire can be estimated to be completely faceted, allowing the use of a simple growth model, as proposed by Schwarz and Tersoff [47]. They propose a formula for facet growth rate as follows:

$$v_i = \alpha_i(\mu_l - \mu_i), \tag{15}$$

where v_i denotes the normal velocity of the facet, α_i is the rate constant that can be different for different facets, μ_l is the chemical potential of the NW material in liquid and μ_i is the chemical potential of the facet. v_i can be used to calculate the axial growth rate as well [48]. The chemical potentials are described in more detail in [47], and μ_l includes liquid composition, interfacial energies, droplet curvature, wire material density and material volume added to the droplet from vapor phase. μ_i takes into consideration capillary pressure, interfacial energies, facet areas, their movements and interactions. [47] Higher potential difference leads to faster growth according to equation (15), which is consistent with the previous discussion in the thesis.

Simulations suggest that facet growth rates have a strong effect on wire morphology, and that they can affect the occurrence of kinking and crawling of nanowires. Small variations in local environment can lead to kinking of the nanowire in case the variations cause a facet in a new growth direction to be energetically favorable. The variation can be caused by thermal gradient in growth chamber, for example. [47] Also growth rate has been observed to affect the fraction of kinked wires with Au-assisted Si nanowires [49].

For the crawling of nanowires, the simulations also suggest a similar explanation to the kinking phenomenon. In the beginning of the nanowire growth, a tapering pedestal is formed under the seed droplet. The droplet must introduce new facets after this initial state, in order for the nanowire to grow epitaxially. In case the introduction of new facets fails, the pedestal continues tapering until the seed droplet falls off, and the wire growth continues along the surface. The failure can be caused by energetic hindrance for new facet formation, which also could result from local changes in the environment. [47]

2.4. Growth parameters and their effects

2.4.1. Oxide removal

Although oxide removal is not a growth parameter, it has a substantial effect on the success of epitaxial growth of nanowires, and is therefore discussed here. As described in chapter 2.2., epitaxy is a delicate process that can be ruined by surface defects or impurities such as native oxide. Silicon oxide (SiO_2) can be effectively removed with hydrofluoric acid (HF) or with buffered hydrofluoric acid (BHF). Etch rate for SiO_2 with HF can reach the order of 1 µm/min and with BHF 100 nm/min. [50] Since the native oxide is only few nanometers thick, dipping a sample to either of the etchants for a few seconds removes the oxide completely.

More importantly, the surface quality after etching differs with the two etchants. HF etch results in an atomically rough surface, whereas BHF produces smooth ones with atomically flat terraces hundreds of nanometers wide [51]. The smooth surface in turn has a higher yield of vertical nanowires [29]; thus, surface smoothness is important to achieve a good yield of vertical nanowires.

After the native oxide is removed, the surface will be vulnerable for oxygen in the surrounding atmosphere; a new layer of native oxide forms in a timescale of hours [17 p. 4]. Indeed, the native oxide formation for one hour after etch has been reported to reduce the proportion of germanium nanowires growing vertically from 94 % to 63 % [52]. The pace of native oxide formation can be reduced by passivating the silicon surface. After etching, the surface atoms have dangling bonds, which promote oxidation. When the passivating atoms, for example hydrogen atoms, are attached to the dangling bonds the effect can be countered. Both HF and BHF etches indeed provide a hydrogen-passivated surface [51], although the passivation gives only limited protection and for a limited time.

In case gold seeds are deposited from a colloid solution, the harmful effects of native oxide can be further decreased by the addition of HF or hydrochloric acid (HCl) to the solution. Possible residues of native oxide are then further etched during the seed deposition, increasing proportion of vertically growing nanowires [52]. When HCl is used, the resulting substrate surface can be Cl-terminated instead of H-terminated.

2.4.2. Temperature

Temperature is one of the most essential and basic parameters used in the control of nanowire growth. Additionally, the nanowires grow only within a limited temperature range. Low temperature limit of nanowire growth is lower than the planar growth of a given material, due to reasons described in chapter 2.3.3. For GaAs nanowires grown in MOVPE, growth has been reported to occur at as low as 330 °C, but with significantly varying morphology [53]. Device applications generally require well-defined structures and good crystal quality, properties lacking in nanowires grown in low temperatures. These properties are commonly found in epitaxial nanowires. Straight NWs can be grown on amorphous materials as well, although they lack the directionality of epitaxial ones. Epitaxial GaAs NWs have been grown with good yield at 400 °C on GaAs substrate [26] [39], and at 417 °C on Si substrate [29], but epitaxy has been reported to fail already at 390 °C [53]. Actual temperatures in different MOVPE systems may differ with some tens of degrees from the reported values, since the temperature measurement in MOVPE is not accurate.

At low growth temperatures planar growth is kinetically hindered [28], whose onset is around 480 – 500 °C [39 p. 62], leading the growth to occur solely via the seed particles. Nanowires have then a constant diameter dictated by the seed particle, and their crystal structure is ZB or WZ, depending on nanowire diameter and growth parameters [10] (ZB for GaAs [9] [10]). When the temperature is raised, growth occurs also on the substrate and nanowire surfaces. Those parts of a nanowire close to its base are exposed to planar growth for the longest time, and hence, they become thicker than the parts closer to the tip, resulting in a tapering morphology. The higher the growth temperature is, the faster the planar growth proceeds, and the more tapered the

nanowires become. The planar growth on Si surface refers to cluster formation instead of 2D film due to the large lattice mismatch.

The lower limit of the nanowire growth temperature can be stretched to some extent by using a two-temperature process, where nucleation occurs at a relatively high temperature. After nucleation the sample is cooled down to a growth temperature, which can be colder than would be possible with a single-temperature growth. With this technique, epitaxial GaAs nanowires have been grown with a good yield at temperatures as low as 350 °C. [53] This indicates that the activation energy of nanowire nucleation is higher than that of growth itself.

When the temperature is raised from the low limit, nanowires first become increasingly tapered and eventually cone-shaped. At high temperatures most of the adatoms contribute to the sidewall growth, reducing axial growth rate and thereby nanowire length [26] [29].When the temperature is raised further, the epitaxy fails eventually. In general, adatoms seek to position themselves according to a characteristic crystal structure, since the crystal structure is energetically favorable for an ensemble of atoms. However, when the adatoms have sufficiently high thermal energy, subsequent layers grow before all of the adatoms find their positions, causing defects to the epitaxial growth. Similarly, nanowire nucleation can occur to a random direction due to exceedingly fast growth. In literature upper temperature limits have scarcely been reported, but GaAs wires have been grown on Si at 550 °C with low molar ratio [9] and at 600 °C on GaAs(111) [54].

Temperature has a substantial effect also on the crystal structure of nanowires. Simulations predict generally higher twin plane density with higher supersaturation [9] (thus, with higher temperature as well according to eq. (14)), even though supersaturation between vapor and solid generally decrease at higher temperature [10]. However, precursor decomposition increases exponentially with temperature, increasing the supersaturation [10]. The increase in twin plane density with higher temperature has also been experimentally verified by numerous groups [9] [10] [29] [53] [55], and transition from pure ZB to pure WZ in GaAs NWs was found when temperature was varied from low to high while varying molar ratio as well [9]. The theoretical modeling of the phenomenon is described in detail in [9]. Pure crystal quality, either WZ or ZB in nanowires, is desirable in optical applications due to improved photoluminescence (PL) properties [53] [56].

As crystal growth is a thermally activated process, growth rate increases with increasing temperature, as can be seen from equations (14) and (15). Also precursor molecules in MOVPE decompose more completely at higher growth temperatures. However, in MOVPE the NW growth rate decreases after a peak temperature that corresponds to the temperature where the precursor trimethylgallium (TMG) loses its last methyl group. At elevated temperatures the planar growth competes with axial NW growth, depleting the surrounding atmosphere from reactants and hence reducing axial NW growth rate. [30] With precursors TMG and AsH_3 the peak growth rate has been reported to occur at approximately 475 °C on Si(111) [29] and GaAs(111) [30] substrates, and with precursors TMG and tertiarybutylarsine (*TBA*) at 440 °C on GaAs(111) substrate [34 p. 66].

2.4.3. Molar ratio

Second main parameter used to control III-V NW growth in MOVPE is molar ratio, *i.e.* the ratio of reactant species in moles available in the reactor chamber. Since precursor molecules contain one group III or V atom, molar ratio is the same for the precursor gases as well. However, as precursor decomposition requires a moderately high temperature, a portion of precursors will not contribute to the growth, resulting in a lower effective molar ratio for the precursors. In principle, growth could occur at any given molar ratio, but in practice group V precursors should be in excess in order to avoid homogenous nucleation of group III species [40 p. 161]. Nevertheless, NW growth with molar ratio as low as 0.74 has been achieved [26].

Joyce *et al.*observed that low molar ratio resulted in increased twin plane density and carbon impurity incorporation in NWs; therefore, NWs grown with low molar ratio would be problematic in many applications. The measured wires were GaAs NWs grown with molar ratio of 12. [57] On the other hand, later the same group fabricated pure WZ GaAs nanowires with a combination of low molar ratio and high temperature, though the carbon impurity was not commented on the latter paper [9]. Bao *et al.*reported that low molar ratio also results in "worm-like" structures growing at surfaces, most likely due to group III homogenous nucleation and droplet formation in group III –adatom rich environment [29].

Possible problems with low molar ratio suggest the use of high ratio. Indeed, twin plane density in GaAs NWs has been found to decrease with increasing molar ratio [9] [29] [57]. However, GaAs [43] [57] and InAs [58] NWs grown at high molar ratios (approximately at V/III = 90) have been found to become tapered and kinked. Nevertheless, InAs NWs have been grown with molar ratio as high as 1500 [59]. Tapering of the wires can be explained with lower activation energy of planar growth at higher V/III ratios, leading to competing radial growth on NW sidewalls, which also leads to lower axial growth rate. The radial growth offers an explanation also to the kinking of NWs. The radial growth consumes a proportion of Ga adatoms diffusing along the NW surface, precluding them from reaching the growth interface. This in turn deprives the seed particle from these adatoms, lowering their concentration and possibly altering the state of the particle. In a different state other growth direction may become preferable, and the NW becomes kinked. Another explanation for kinking is changes in surface energies; for example, excess As can form As-terminated (111)B surfaces, causing the growth system to favor another growth direction. [57] It should be noted that NW growth process depends on various factors, and the effects of varying molar ratio cannot be considered alone. Although high molar ratio has been found detrimental to NW quality, combined with low temperature it resulted a in twin-plane free pure ZB nanowire structure [9].

Growth rate has also been found to vary with molar ratio [57][58][59]. Joyce *et al.*found that, at low molar ratios, GaAs NW growth rate increases with increasing molar ratio due to enhanced decomposition of TMG with excess AsH_3 [57]. The enhanced decomposition of group III and group V precursors when both are present can be considered a general effect [40 p. 161]. At higher ratios the axial growth rate is diminished, because radial growth becomes significant and consumes a proportion of Ga adatoms, as discussed above. Also the As-terminated (111)B surfaces explained

above might hinder growth in the [111]B direction. [57] Similar behavior for InAs growth rate was reported by Dick *et al.*[59].

In general, most suitable molar ratio for NW growth is moderately high but below the onset of kinking. In the intermediate region stacking defect density remains low, and NWs grow in well-defined directions. Also, the axial growth rate is fastest at intermediate molar ratios, which is beneficial, as explained in more detail in the next subchapter.

2.4.4. Total molar flow

Total molar flow of precursor gases in MOVPE can be cautiously interpreted as a measure of supersaturation in the growth system [10]. Increasing the molar flow of precursors increases the difference in chemical potential between vapor phase and substrate, as can be seen from equations (8) and (14). However, as supersaturation depends on many other parameters as well, such as temperature, pressure, diffusion and precursor decomposition, which have also effects among each other, the total precursor flow should only be considered as one of numerous factors.

Total molar flow has also an effect on twin plane formation [9] [10], and hence it affects crystal quality as well. Different simulations indicate increasing proportion of twinned planes with increasing supersaturation [9] [60], and therefore with increasing precursor concentrations as well. Another factor affected is the growth rate of NWs, which increases with higher molar flow, as suggested by equation (15), and verified experimentally in [26] [43] [59].

In contrast to bulk material growth, Joyce *et al.*found that rapid growth improves NW properties. The benefits of rapid growth included reduced tapering, reduced crystallographic defect density and low carbon impurity concentration. They suggest that tapering is lower due to different limitations in axial and in radial growth; axial being mass transport limited and radial kinetically limited. The lowered twin plane density could be due to both As and Ga species lowering surface and interface tensions in the droplet. The authors propose that the low impurity concentration results from reduced sidewall growth, which is the main route for impurity incorporation. [43]

However, some of the results are in contrast with previous findings; results from Johansson *et al.*suggest that twin plane density in GaP NWs is higher at higher supersaturation [61]. Joyce *et al.*used total molar flow to vary the level of supersaturation, whereas Johansson *et al.*used pulsed TMG flow and varying In background levels. This indicates that supersaturation alone does not suffice to control crystallographic quality, as other system parameters might have a significant effect as well. Also, in later works, both groups performed simulations which suggest that stacking defect density decreases eventually with increasing supersaturation in certain conditions. The condition in the simulations from Joyce *et al.*is high enough vapor-nucleus interfacial energy [9], and in simulations from Johansson *et al.*it is low enough ratio between energies of stacking defect nucleation and ordinary nucleation [62].

In the previous subchapter effects of varying V/III ratio were discussed. Regardless the total molar flow, effect of varying molar ratio on morphology remains the same [10]. However, as previous results have shown both increasing [61] and decreasing [43] stacking defect density, it can be concluded that the optimal total molar flow depends on the used system.

2.4.5. Pressure

Pressure is perhaps the least studied parameter affecting NW growth. However, as the phase diagram of a given growth system depends on the absolute pressure, it can cause changes in appropriate NW growth parameter windows. Moreover, pressure affects supersaturation [10], which in turn is important parameter in NW growth. Another affected parameter is the mean free path of diffusing adatoms, since in higher pressure the adatoms travel shorter distance. Reasoning for this is intuitive; when the density of both group III and group V adatoms is higher, they have higher probability to collide and to nucleate close to their adsorption sites.

Reduced diffusion length, or increased nucleation on surfaces, increases tapering of NWs. Experimental results, which can scarcely be found, support this reasoning. Caroff *et al.*observed notably increased tapering with InAs NWs when reactor pressure was raised fivefold [55]. Also morphology of NWs changed clearly in their experiment [55]. Despite the probable effects of pressure in NW growth, it has been scarcely studied in theory or in experiment.

2.4.6. Growth time

Particle-assisted NW growth changes little during the growth if the conditions are kept stable. With non-catalyzed growth the seed droplet may become incorporated to the wire, ceasing the growth, but as seeds of foreign material are generally not consumed, this effect can be ignored in the particle-assisted growth. There are, however, minor effects associated with growth time with particle-assisted growth as well. First, the effective adatom collection area shrinks when the seed droplet is lifted from the substrate surface. Initially the collection area includes substrate surface within diffusion length, but as the seed particle rises, the area shrinks. After the height of the nanowire equals the diffusion length of adatoms, adatoms landing on the substrate cannot contribute to NW growth, and all of the diffusing growth material comes from the wire surface.

Secondly, when nanowires have reached moderate length, the surface area in the proximity of the seeds is increased due to the emerged nanowire surfaces. In case planar growth is significant, it consumes a considerable proportion of available reactants, reducing mass transport to the axial growth site and decreasing NW growth rate. Nevertheless, this effect on the growth rate should be small.

Third possible effect is related to enhanced decomposition rate at the substrate surface. Distance of the seed droplet from the substrate surface can therefore affect on the number of different reactants available. Depending on the system, the effect can deprive the growth site from a proportion of one or more reactant species, therefore possibly affecting effective molar ratio and total reactant concentration.

Nevertheless, experiments suggest that growth rate remains approximately constant during the growth. Only notable finding was that the nucleation requires few seconds after introduction of precursor gases in MOVPE. Otherwise NW length has been observed to have a linear dependence on growth time. [26] [29]

2.4.7. Seed diameter

Surface energy in WZ structure is lower than in ZB structure [10]; therefore, as nanowire diameter decreases, and surface-to-volume ratio increases, WZ becomes energetically more favorable. This would suggest that a small seed particle diameter leads to a larger proportion of WZ sections in ZB nanowires, or even to pure WZ nanowires. Indeed, pure WZ and ZB InAs nanowires have been grown by varying only the seed particle diameter [55] [63]. However, since both pure GaAs ZB and WZ nanowires have been grown for a range of seed particle diameters [9], it is clear that the diameter should be considered as only one factor among others.

Another effect arising from diminished diameter is Gibbs-Thomson effect. In III-V nanowire growth with MOVPE, the effect predicts increased partial pressure of group III element in the seed particle [63]. As the effect influences supersaturation, it affects NW morphology and growth rate as well. Effects become more significant with small seed particle diameters [60] or in a low-supersaturation system [64]. As described above, NW morphology is indeed affected by the seed diameter. Nevertheless, in typical MOVPE growth conditions, the supersaturation is large regardless the seed particle diameter, and Gibbs-Thomson effect can be neglected [64]. On the other hand, in a system with low supersaturation, the effect remains significant with relatively large seed diameters [63].

In case Gibbs-Thomson effect is valid, group III element pressure ($p_{l,III}$) in alloy droplet can be calculated with [63]

$$p_{l,III}(r_p) = p_{l\infty,III} e^{\left(2\sigma_a \Omega_{l,III}/r_p k_B T\right)}, \tag{16}$$

where r_p is the seed particle radius, $p_{l\infty,III}$ is the vapor pressure of the group III element in an infinitely large alloy particle, σ_a is the surface energy of the particle, $\Omega_{l,III}$ is the atomic volume of group III element in the particle and k_B is the Boltzmann constant. This in turn can be used to calculate the chemical potential of the group III element in the seed particle: [63]

$$\mu_p = \mu_{p0} + k_B T \ln \frac{x_{III} p_{l,III}(r_p)}{p_{l0,III}}, \tag{17}$$

where μ_p is the chemical potential in the seed particle, μ_0 is a reference state for the chemical potential, $p_{l0,III}$ is a reference state for the group III partial pressure, and x_{III} is the atomic fraction of the group III element in the seed particle. From the equations (16) and (17) it can be seen that the chemical potential in the seed particle is inversely proportional to the seed particle radius; therefore, supersaturation decreases in small seed particles. [63] This leads to reduced growth rate, as explained in chapter 2.4.4.

Decreased growth rate with small diameters has been attributed to the Gibbs-Thomson effect in experiment [26], although other experiments have demonstrated also opposite behavior [59] [64]. The controversial results can be explained by differences in the growth systems; the growth-limiting process determines the behavior. The reactants from the seed particle are removed through the particle – nanowire interface, which can be approximated flat. The interfacial area between the seed particle and the NW top

(A_{pt}) is then a circle with radius of the seed particle (r_p). This gives the dependence $A_{pt} \sim r_p^2$. At steady-state growth (NW length exceeds the diffusion length of reactants), majority of the reactants diffuse along the nanowire surface from area next to the NW top within the diffusion length ($A_{wt} = 2\pi r_p \lambda_{diff}$), and $A_{wt} \sim r_p$. It is clear that ratio A_{pt} / A_{wt} increases with radius, decreasing the growth rate. On the other hand, if the growth is reaction-rate limited, other effects such as Gibbs-Thomson effect may prevail.

2.4.8. Seed particle density

When NWs grow in close proximity to each other, they share the diffusion area on the substrate in the beginning of the growth, leading to competition of available growth material. The competition ceases when the NW length exceeds the diffusion length of group III material (group III materials diffuse further than group V materials [16 p. 35]), since the adatoms diffusing to the growth interface land only on the NW sidewalls. However, if the density is extremely high, the atmosphere might be depleted to some extent from the growth species, which reduces supersaturation and hinders the growth. This effect was suggested to take place with a density of order 100 NW / μm^2 for GaAs NWs [65].

In other experiments, no significant length dependency on density was observed for GaAs or InGaAs NWs with low In composition. However, when the In composition was high, NW length decreased with increasing density. This behavior was attributed to longer diffusion length of In on GaAs(111)B surface, which was used in the experiment. The density was low enough for competition of Ga adatoms to remain insignificant, whereas competition for In species hindered the growth rate. The competition for In species between NWs was verified by lower In composition with higher wire density. [66] The results indicate that the effects of the density depend on the diffusion lengths of the used materials. For GaAs NWs, the effect is negligible even with moderately high densities (0,7 NW / μm^2 was used in [66]).

2.5. Surface states and passivation

2.5.1. Surface states and effects

In a perfect bulk crystal, atoms are placed according to the lowest internal energy configuration for the structure, with a certain number of neighbors for each individual atom. At the surface, however, the number of neighbors is reduced, leaving part of normally occupied bonds dangling and altering the lowest energy configuration. Therefore, atoms at the surface adjust to the new configuration, forming a *surface reconstruction* which tends towards lowest possible internal energy. [15 p. 13]

The dangling bonds prefer to be charged and can introduce shallow and deep traps to the forbidden energy gap. Additionally, surface is vulnerable to absorption of impurities which cause additional trap states. Energy levels of the traps can be distributed throughout the forbidden energy gap, as shown in figure 12, forming a path for electrons and holes to recombine nonradiatively near the surface [67 p. 120]. Compared to many other semiconductors, GaAs has poor surface properties [68].

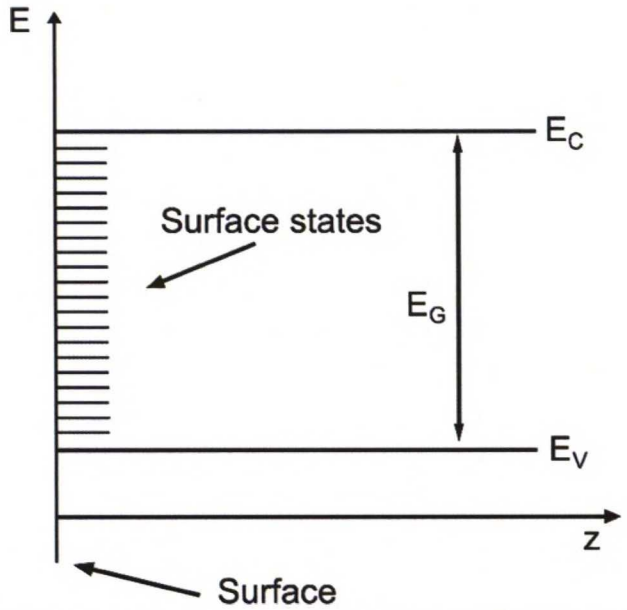

Figure 12: Band diagram with surface states within the band gap caused by surface defects and impurities. The states can be situated at any levels throughout the band gap.

Due to the detrimental effects of the surface states, surface passivation is crucial in many electronic and optical applications. An ideal passivation layer performs three functions: (i) chemical passivation, *i.e.* preventing any reactions between ambient atmosphere or subsequent layers; (ii) electrical passivation, *i.e.* preventing or eliminating interfacial trap states; (iii) providing a potential barrier for charge carriers [69]. A passivation layer may also perform only one or two of the functions.

In chemical passivation, atoms in the passivating layer form bonds with the surface atoms. The resulting surface layer is then ideally inert. A hydrogen passivated surface, where a hydrogen atom occupies each dangling bond, can be thought as a simple chemical passivation layer. Electrical passivation refers to quenching the surface or interfacial states. The passivation layer provides an interface with considerably fewer trap states compared to a bare surface. However, the surface of the passivation layer might also have high density of trap states. In case the passivation layer acts also as a potential barrier, the charge carriers travel preferably to the core, and a smaller percentage recombines at the new surface. The potential barrier is essentially an offset in band gaps of the materials. The junction of the materials should be of type I (see figure 4), with the passivating material having a larger band gap. The larger the offset between the band gaps is, the better passivation the layer provides.

2.5.2. In-situ passivation with core-shell nanowires

In-situ passivation in a MOVPE reactor is practically performed by growing a core-shell NW structure. A core-shell (CS) nanowire has a typical NW as a core, on which a conformal film (shell) is deposited. Figure 13 shows the process of CS NW growth and a cross section of the NW. The shell of a CS NW can perform all of the three passivation functions described in the previous chapter.

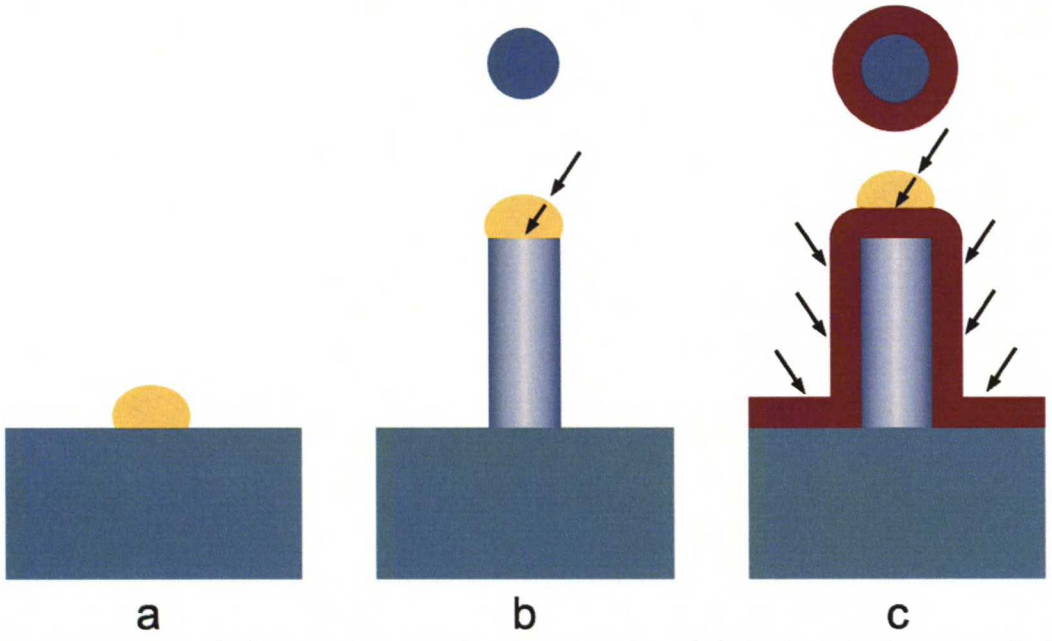

Figure 13: Core-shell nanowire growth. First a seed particle is deposited (a), a typical NW is grown (b), after which a planar film is grown to form a shell (c). The arrows indicate places for growth during the different steps. Cross section of the NW is presented above the wires.

For a shell to act as a potential barrier, it needs to have a larger band gap than the core, and the junction should be of type I. The shell material for GaAs NWs is commonly AlGaAs [70] [56] [71] [72] [73] [74], and other materials include GaInP [75], GaP [76] and GaAsP [77]. GaAs has also been used as a shell material for InGaAs NWs [78]. AlGaAs is the most popular shell material due to its good lattice match with GaAs (~0.3 % mismatch to AlAs [79]), notable band offsets in conduction and valence bands, effective passivation and high electron mobility [71]. On the other hand, shell materials with a considerable lattice mismatch cause strain in the core and HH- and LH-bands to split. Therefore, strained CS NW structures allow band gap engineering. [76]

The performance of the potential barrier depends also on its thickness. The thickness should be sufficient to inhibit exciton tunneling through the shell to the surface. A relatively thick lattice-matched shell remains harmless to optoelectronic purposes, since the charge carriers travel from the shell to the core due to band offsets. Only a thick shell with indirect band gap or low band offsets might suppress PL in the core. In case of ternary shells, a sufficiently high composition of a large band gap material is required to achieve adequate band offset. If only chemical passivation is desired, one or few monolayers of passivating material suffice for passivation.

CS GaAs nanowires have shown notable increase in PL intensity compared to bare NWs, including increase over a magnitude for GaAs/AlGaAs NWs [56] and 2-3 orders of magnitude for GaAs/GaInP [75] and InGaAs/GaAs NWs [78]. For highly tapered GaAs NWs also reduced PL intensity was observed with AlGaAs shell deposition [54].

The PL signal peak typically shifts from the bulk value in CS NWs. For GaAs/AlGaAs NWs low temperature PL peaks have been reported at ~820 nm [43] [56]

[57] and at ~840 nm [30] [54]. The ~820 nm peak corresponds to free exciton recombination in MOVPE grown bulk GaAs [80], and it has been observed in GaAs/GaAsP NWs as well [77]. The redshift in GaAs/AlGaAs NWs to 840 nm was suggested to arise from tensile strain caused by the shell [30] [54]. On the other hand in ref. [54] bare GaAs NWs had the PL peak only a few nanometers below the 840 nm peak, thus the peak had redshifted only slightly. In ref. [30] bare NWs were not studied.

With strained CS structures notable shift in the PL peak position has been observed. When varying the lattice mismatch over 2.6 %, PL peak shifted ~135 nm in one study [75] and in another a mismatch of 3.6 % caused the peak to shift 120 nm [76]. Peak broadening has also been observed due to inhomogeneous strain [75].

2.5.3. Ex-situ passivation by atomic layer deposition

In atomic layer deposition (ALD) one atomic bilayer at a time is deposited conformally. Thus, it provides similar passivation as core-shell structures, but due to slow growth rate in ALD, typically thin layers are made. This thin layer is enough to provide chemical and electrical passivation, but electron tunneling to the surface remains in effect. Thus, no effective potential barrier is acquired. For this reason good surface properties are desired for the passivation layer.

In previous studies, GaAs surfaces have been successfully passivated with ALD. In the studies, near-surface quantum wells (QW) were passivated with aluminum nitride (AlN) [81] and titanium nitride [82]. Both of the materials showed improvement in PL intensity of circa an order of magnitude compared to a nonpassivated sample. However, the improvement was strongly dependent on the layer thickness. The best results were acquired with 0.3-0.5 nm thick AlN layer [81]. The AlN layer was also characterized with EDS, which showed no oxygen; thus no detrimental oxygen bonds were formed at GaAs surface. [81]

3. Research methods

3.1. MOVPE

All of the samples in this work were prepared with a MOVPE apparatus in the Micronova clean room premises of Aalto University. The apparatus is manufactured by Thomas Swan & Co. Ltd., and its operational principle is presented in figure 14. The essential part of the system is a quartz reactor in which the growth occurs. A substrate is heated there to growth temperatures and controlled flows of precursor gases are directed to the reactor, enabling the growth of NWs and other structures.

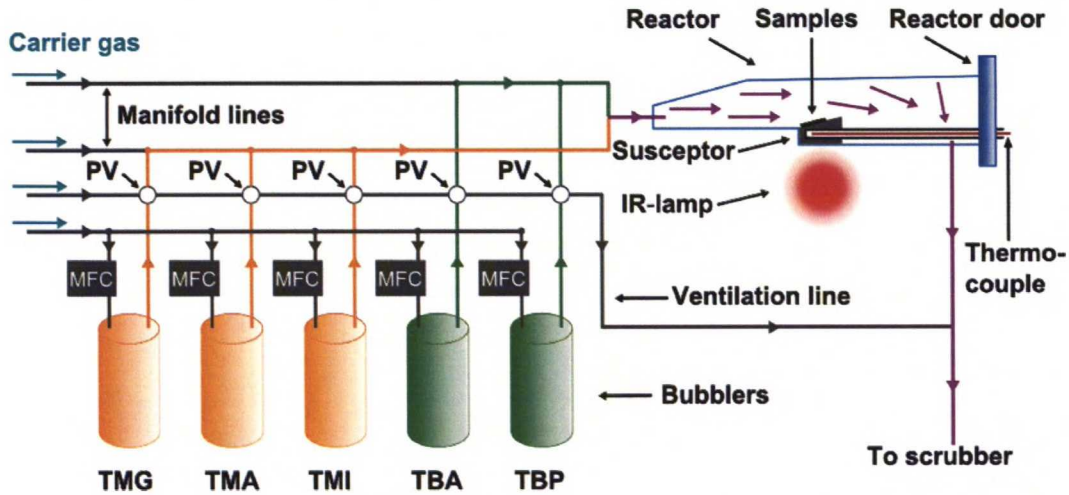

Figure 14: Operational principle of the MOVPE system. Orange color indicates group III materials, green group V, and purple mixture of the two. In the figure all of the precursors are directed to the reactor, but each can be directed to ventilation line instead with PVs. The arrows on the lines and inside the reactor indicate the direction of the gas flow.

The process begins with sample preparation and loading. Sample preparation in this work includes cleaning, typically followed by etching and Au particle deposition. The prepared samples are first brought to a glove box with nitrogen atmosphere. There they are placed on a graphite susceptor which is then put to the reactor. During the loading, nitrogen flows through the reactor for safety reasons.

After the loading, the reactor door is sealed and the reactor is tested for leakages under nitrogen flow in pressures lower and higher than what is used during the growth. When no leakages are detected, gas flow is switched to hydrogen, which is used to remove residual oxide from the substrate and as a carrier gas for precursor materials.

The precursors used in MOVPE are organometallic, including group III precursors trimethylgallium (TMG), trimethylaluminum (TMA) and trimethylindium (TMI), as well as group V precursors tertiary butyl arsine (TBA) and tertiary butyl phosphine (TBP). The precursors are in inside bubblers which are kept in a desired temperature in a liquid bath. Inside bubblers they are in liquid form except for TMI,

which is solid. Operating principle of a bubbler is presented in figure 15. A carrier gas, *i.e.* hydrogen, is introduced to the liquid precursor material. As the carrier gas flows through the liquid, it becomes saturated with the precursor material i with vapor pressure p_{vi} [20 p. 20]:

$$p_{vi} = \bar{p} 10^{c_i - d_i/T}, \tag{18}$$

where $\bar{p}$ is a proportionality coefficient, c_i and d_i are material-dependent constants and T is the temperature of the precursor liquid. The TMG bath of the MOVPE system had a set point of -10 °C, but actual temperature varied circa 0.5 °C below the set point. Thus, actual TMG flow to the reactor has varied slightly between growth days.

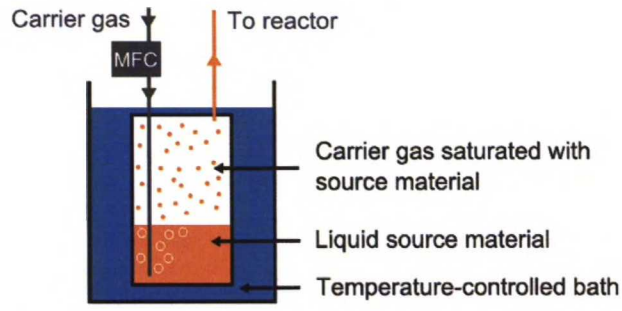

Figure 15: Operational principle of a bubbler.

Flow of the carrier gas to the bubblers is controlled with mass-flow controllers (MFC). From the bubblers precursor gases are directed with pneumatic valves (PV) to either ventilation or manifold lines. Some of the precursor flows to the reactor can be diluted with hydrogen to decrease the flow rate. To stabilize the precursor gas flow, it is first directed to the ventilation line for a few minutes. It is then directed to the manifold lines which lead to the reactor. There are own manifold lines for group III and group V precursors in order to prevent premature reactions. Total gas flow to the reactor is kept constant with make-up lines.

The group III and group V precursor flows are combined shortly before they reach the reactor. Flow of the precursors inside the reactor is made laminar by the reactor shape. Pyrolysis of the precursors requires elevated temperatures, and thus the substrate is heated. This is done by heating a graphite susceptor with an infrared (IR) lamp. Graphite absorbs infrared wavelengths well and is thus heated efficiently. Temperature of the susceptor is measured with a thermocouple, which is inside a quartz tube. However, as the temperature is not measured directly from the substrate, which is cooled by a constant gas flow, the readout is cooler than the substrate temperature. Moreover, the temperature of the substrate surface depends also on heat conductance from the susceptor. This is affected by the heat conductance of the substrate material, and possible substrate bending or susceptor surface topography, which reduce the contact area between the susceptor and the substrate. In general, the temperature readout is some tens of degrees Celsius above the actual substrate surface temperature. All of the temperatures reported in this thesis are measured from the susceptor.

The pyrolysis of the precursors is a complicated step-wise process. As an example, TMG consists of three methyl groups attached to a gallium atom. The methyl groups detach one by one at elevated temperatures, last one detaching at about 450 – 475 °C [30]. The pyrolysis processes are affected by other factors as well, such as presence of other precursors and a substrate surface, and crystal growth is possible at significantly lower temperatures than what is required for a complete pyrolysis. After the precursors are decomposed, adatoms diffuse to the surface and undertake processes explained in chapter 2.2. Reaction byproducts and the precursors that do not take part in crystal growth are flushed to the ventilation line out of the reactor. The ventilation lines lead to a gas scrubber.

After the crystal growth the substrate cools down slowly. The crystal surface consists of group V atoms due to the high V/III –ratio used in III-V material growth. To prevent desorption of the group V atoms the reactor is flushed with group V precursors during the cooling. The group V layer on the surface on the other hand prevents desorption of the group III atoms. Finally, the gas flow to the reactor is switched back to nitrogen to enable loading of the next sample.

During the process growth takes place also on reactor walls, reactor door and thermocouple tube as well. During subsequent growths part of that material desorbs and may travel to the sample surface and affect crystal growth. Therefore, the reactor and the other parts with undesired growth are cleaned regularly.

During the growth runs, different parameters were adjusted with a control software. The software controlled temperature, carrier gas flow, precursor flows and their dilution, and durations of different steps in a growth recipe. The growth recipe was written stepwise, and different parameters were given in each step. Table 2 presents the used growth parameters at different growth steps. Steps 5 and 6 were used only when CS NWs were grown. The parameters that were varied included temperature, growth time, total molar flow, V/III ratio and shell composition and growth time. In the study a growth time of 60 seconds and a TMG flow of 10.8 µmol/min were used unless stated otherwise. The Ga addition step (2) before the NW growth was qualitatively found beneficial in seeding epitaxial growth, and was also included in growth runs unless stated otherwise.

Table 2: Steps included in NW growth. Steps 5 and 6 were included only in CS NW growth.

#	Step	T (°C)	Time (s)	TMG (µmol/min)	TMA (µmol/min)	TBA (µmol/min)	TBP (µmol/min)
1	SiO_2 rem.	650	600	-	-	-	-
2	Ga addition	650	3	10.8	-	-	-
3	Cooling	To growth T	-	-	-	-	-
4	NW growth	370-560	15-300	1-14	-	19-270	-
(5)	Heating	To growth T	-	-	-	25-30	-
(6)	Shell growth	600-700	2-57	10.8-17.6	5.8-18	439	
7	Cooling	To 250	-	-	-	25-30	-

3.2. Substrate preparation prior to nanowire growth

Substrates for the MOVPE growth were cut from about 0.3 mm thick two-inch exactly oriented Si(111) wafers. Resistivity of the wafers was 1-10 Ωcm. This wafer will be referred to as the reference wafer in the rest of the study. Also two other Si(111) wafers, a highly doped and one with 4° miscut and with resistivity of 8-20 Ωcm, were tested. Differences between different wafers were tested by growing NWs on them in the same growth run after identical sample preparation.

Substrates with a size of approximately 100 mm^2 were cleaved from the wafers. The substrates were first cleaned in ultrasonic bath in acetone and isopropyl alcohol for two minutes each. Next they were rinsed in deionized (DI) water for five minutes and dried with nitrogen.

As native oxide can be detrimental for epitaxy, the substrates were etched in BHF before deposition of Au NPs. Different etch times were studied, and the substrates for the systematic study were etched for 12 seconds. The BHF etch was followed by a quick rinse in DI water and nitrogen drying.

The Au NPs were deposited from a solution manufactured by BBInternational. The solution contained $9 \times 10^{10} \frac{1}{ml}$ Au NPs with a mean diameter of 41.1 nm. Two deposition methods were tested: with poly-L-lysine (PLL) or with hydrochloric acid (HCl). In the PLL method the sample surface is first rinsed with PLL solution in order to form a positively charged layer on the surface, which improves adhesion of negatively charged Au NPs [34]. Deposition of PLL has no effect on nanowire growth besides higher overall density [29]. After the PLL rinse, excess PLL was rinsed off in DI water and Au-particle solution was placed on the sample for a while, and then blown away with a nitrogen gun.

HCl-assisted deposition was performed by placing Au solution on the substrates and adding a small amount of HCl. Different HCl concentrations and Au deposition times were tested. The samples in the systematic study were treated with 19 % HCl added to Au solution for 30 seconds. It has been proposed that acidifying the Au solution neutralizes the Au NPs, allowing them to attach to the silicon surface, which is negatively charged in water at neutral pH [52]. HCl also etches SiO_2 residues availing the epitaxy. After the deposition the solution was blown away with a nitrogen gun.

3.3. Atomic layer deposition

Function principle of ALD is based on the use of materials that grow only one monolayer at a time, and subsequent layers of different materials grow on each other. The growth is performed in cycles, each cycle consisting four stages. The function principle and the four stages are presented in figure 16. In the first stage, first precursor flows into the reactor and decomposes, and the desired material is deposited to the surface (figure 16a). The adsorption of the product molecules is based on chemical reactions; thus the molecules can be chosen from ones that react only with the underlying surface, but not with themselves [83 p. 35]. As the material does not react with itself, only one monolayer is deposited. After the surface is saturated, precursor molecules are purged from the reactor (figure 16b). In the next phase the 2nd precursor is directed to the reactor (figure 16c). Again, one monolayer is deposited, followed by

purging of the 2nd precursor (figure 16d). At this point the surface can accommodate the material from the 1st precursor again, and the cycle starts over.

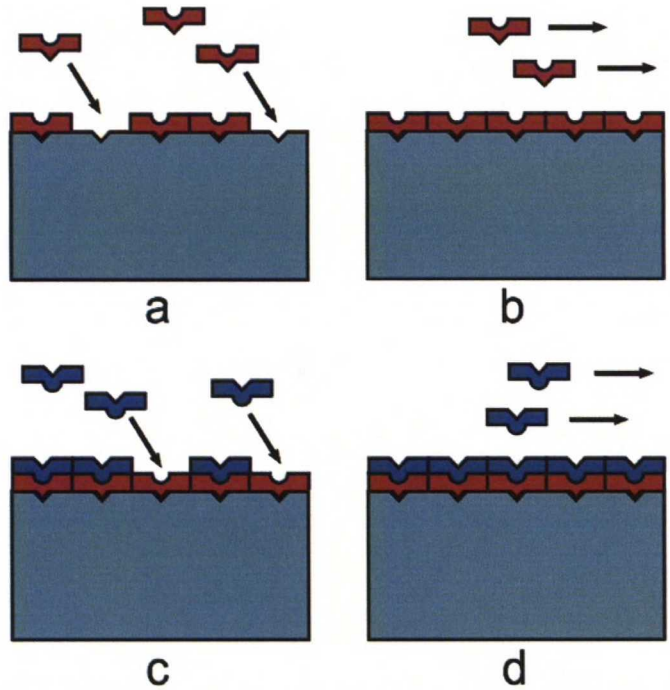

Figure 16: Principle of ALD growth. One cycle consists of four stages: 1st precursor pulse (a), purge (b), 2nd precursor pulse (c) and purge (d). Red blocks indicate the 1st precursor and blue ones the 2nd precursor.

The ALD system used for passivation in this work was Beneq TFS 500. It has a laminar flow type reactor, where the precursor gases flow over the sample. 2 Å and 5 Å thick aluminum nitride (AlN) layers were grown in the ALD reactor. The growth temperature was 150 °C or 250 °C for the cores grown at 450 °C or 470 °C, respectively. The NW surface may oxidize before the ex-situ ALD passivation. Therefore, the native oxide was etched in HF before the ALD growth.

3.4. Characterization equipment

3.4.1. Electron microscopy

Scanning electron microscope (SEM) uses an electron beam to acquire images with resolution down to a 1 nm range. The images are suitable to characterize sample morphology and dimensions, but insufficient to study crystal structures. Electron beam is acquired typically from a heated filament, usually tungsten. The electrons are typically accelerated to energy between 1 keV and 30 keV. The beam is demagnified with electromagnetic condenser lenses down to a nanometer scale at the sample surface. Position of the beam on the sample is controlled with a scanning coil. [84 p. 122-124] A schematic diagram of a SEM is shown in figure 17a.

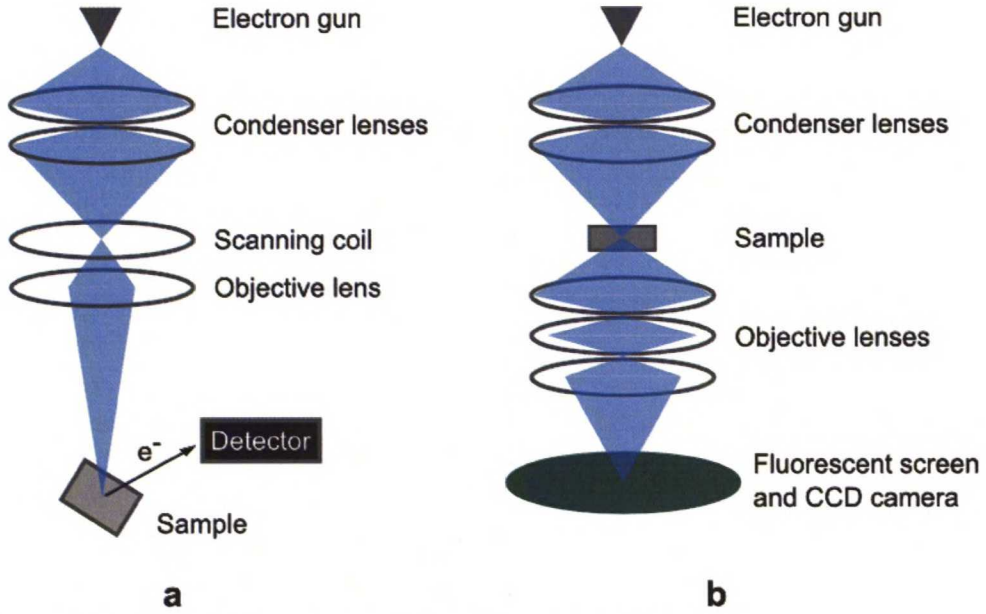

Figure 17: Schematic diagrams of a SEM (a) and TEM (b).

When the incident electrons hit the sample secondary electrons are emitted from the sample atoms. Other signals caused by the beam include backscattered electrons, X-rays and Auger electrons. For imaging purposes the secondary electrons give the best spatial resolution [84 p. 128]. The other signals are more suitable for material or surface characterization, for example.

A SEM image is acquired by scanning the electron beam over a rectangular area stepwise while gathering secondary electrons at each position. This type of scanning is termed *raster scan*. A widely used detector for the secondary electrons is the Everhart-Thornley detector. It uses a thin aluminum film under bias voltage to gather and accelerate the secondary electrons to a scintillator. The electrons then excite the scintillator and the emitted light is detected by a photomultiplier, the signal of which gives intensity of the secondary electrons at each beam position. [84 p. 125, 129] Another type is an in-lens detector, which detects secondary electrons passing through the aperture. The intensity of the secondary electrons is transformed to a grayscale image of the sample.

The SEM device used in this work was Zeiss Supra 40. At optimal working distance it can achieve a resolution of 1.0 nm with 15 kV acceleration voltage. For most images in this work voltage of 9-12 kV was used. Electron source is thermal type, and for imaging the in-lens detector was used.

As transmission electron microscope (TEM) can reach atomic resolution, it can be used to characterize crystal structure and quality of NWs as well as details of their morphology and dimensions. Also TEM uses an electron beam to characterize the sample, but electron acceleration voltage is higher and the beam passes through the sample. Typical acceleration voltages are in the 200-400 kV range for materials science, giving resolution down to 0.16 nm [31 p. 16].

Figure 17b shows a schematic diagram of a TEM system. The electron beam is first demagnified with a group of electromagnetic condenser lenses to the sample, and

after passing through the sample it is directed to a fluorescent screen with another group of lenses. The image of the sample can be recorded with a CCD camera from the fluorescent screen. Magnification up to 1 million can be achieved with the numerous lenses in a high-resolution TEM system. [31 p. 15-16]

For TEM imaging, nanowires were placed on a copper grid covered with a holey carbon film. The NWs were transferred by placing the grid on a substrate with NWs, and by moving the grid on the surface. The NWs then broke off and attached to the grid. To increase their density, the sample surface was also scratched over the grid, thus making NWs fall on the grid. The used TEM apparatus was JEM-2200FS model by JEOL.

In the TEM also an EDS analysis was performed on one of the studied GaAs/AlGaAs NWs. EDS is based on x-rays emitted by the sample material after an inner-shell electron is ejected and replaced by an electron from an outer shell. Each element has its characteristic x-rays, thus chemical composition of a material can be studied with EDS. GaAs/GaAsP NWs were studied with EDS in Hitachi TM-1000 SEM.

3.4.2. Photoluminescence

Photoluminescence measurements are used in this work to study optical properties of NWs, their band gaps, and effect of different passivation methods. In PL electrons are excited with a laser, and when the electrons recombine radiatively, they emit photons with energy corresponding to the band gap of the semiconductor. The energy and intensity of the PL signal can be used to characterize the material. Band gap energy depends on numerous factors, including material composition, stresses, impurities and quantum effects. Signal intensity corresponds to the amount of radiatively recombining electron-hole pairs. Thus, it gives information about defect density and crystal quality of the sample.

Figure 18 presents the PL setup used in this work. A frequency doubled Nd:YVO_4 laser with a wavelength of 532 nm was used for excitation. The laser beam was first attenuated to suitable excitation intensity. The laser beam was then directed to a chopper, which blocks the beam at a desired frequency. After the chopper the beam was focused on a sample with a lens. The intensity on the sample was circa 10 mW for most of the measurements in this work.

During the measurement samples were placed in a cryostat and the temperature was varied between 20K and 170K. The samples were attached to a vertical holder which was at approximately 45° angle towards the laser and on the other side to a monochromator, as shown in figure 18. PL signal has been observed to be higher in the direction parallel to the nanowires [85], thus an inoptimal signal was acquired from samples with vertical NWs.

The PL signal from the sample was collected with a lens, and focused to the monochromator input with another lens. The monochromator allows only one wavelength go through at a time, allowing stepwise signal detection at different wavelengths. The monochromator could be damaged from high intensity, thus a filter was placed at the input to block the reflected laser beam. Cutoff wavelength of the filter was 610 nm, thus it blocked the laser efficiently, but allowed the PL signal to go through, as its expected wavelength was well above 610 nm. Before measuring the

samples, monochromator calibration was checked with a reference sample with a known wavelength.

From the monochromator the signal is guided to a germanium detector which was cooled with liquid nitrogen to 77 K. The detector can detect wavelengths from 400 nm to 1600 nm, although the signal is weak for near both of the limits. After the detector the signal was read by a lock-in-amplifier. A lock-in-amplifier registers only the signal corresponding to the chopper frequency. Finally the signal was converted to a digital form and read by software.

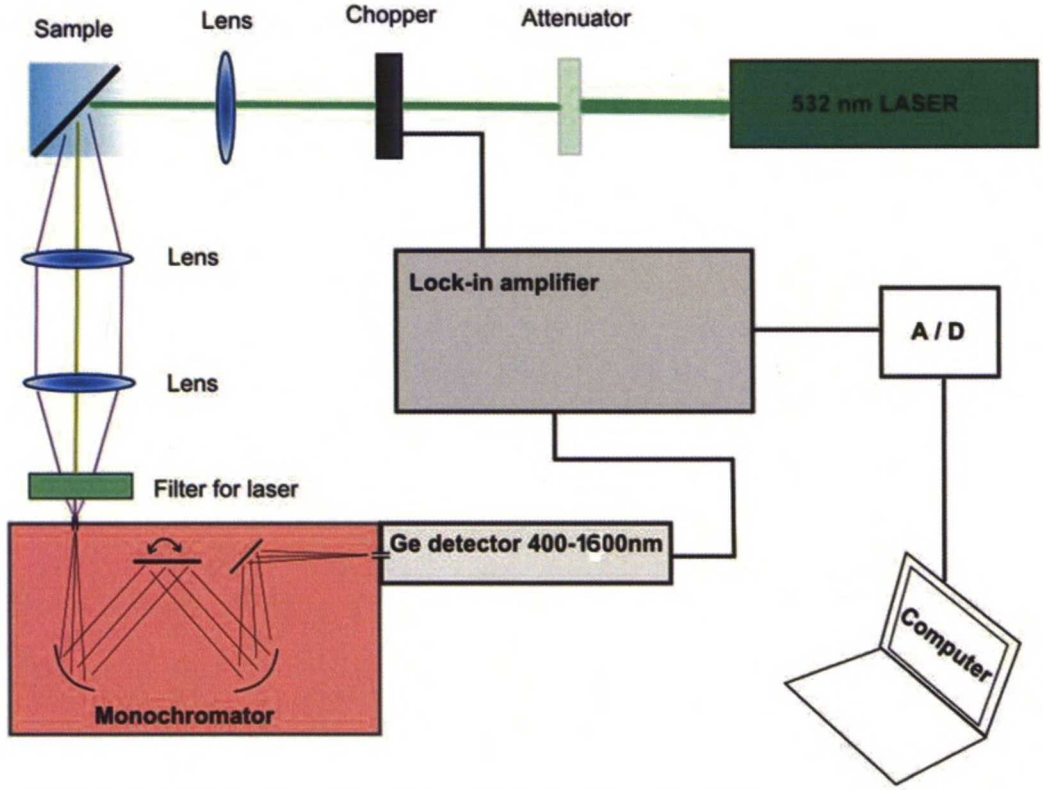

Figure 18: Schematic diagram of the used PL measurement setup.

4. Results and discussion

4.1. Effects of substrate preparation

Substrate preparation studies included different Si(111) wafers, oxide etch time, Au NP deposition methods, and HCl concentrations in the HCl-assisted Au deposition. All of the presented results are acquired from the reference wafer unless stated otherwise. The parameters studied were NW density and yield of epitaxial NWs.

NW density varied between approximately 0.2 and 0.7 NW/μm^2. The density was comparable to what has been reported elsewhere with similar deposition methods and Au NP solution [66]. The density varied considerably within some samples as well, as figure 19 shows. From such samples only the successful areas were considered in the study. Density of as-deposited Au NPs was found to be approximately 0.9 – 1.5 NP/μm^2 on three different samples, indicating that only a portion of the Au NPs seed NW growth. Differences in Au NP density can be attributed to agglomeration of the NPs during storage and to the inexact deposition methods.

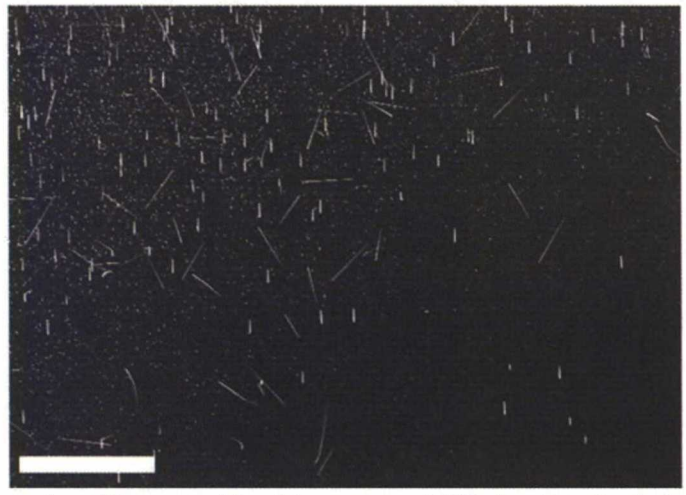

Figure 19: A sample with a considerably varying NW density. Scale bar is 10 μm and viewing angle is 15° from top view.

Table 3 presents densities of numerous samples used in the systematic study. The data was acquired from SEM images by counting the NWs on 4-6 areas of approximately 150 μm^2. No clear dependence on any parameter was found. The variation in density can be explained in part by agglomeration of Au NPs during storage, and in part by variation in the success of Au NP deposition. Additionally, some growths on the surface could not be identified as Au-seeded nanowires, since similar growths were seen on samples without Au NPs on them. Such growths are presented in figure 20, and they explain the low density with T = 430 °C in the series V/III = 2. This sample had considerable amount of growths along the surface and only few actual NWs. As the NW density on the sample was only ~0.02 NW/μm^2 and a typical Au NP density was ~1 NP/μm^2, it is reasonable to assume that most Au particles contributed to growth along the surface.

Table 3: NW densities with different growth parameters. *Temperature was 510 °C instead of 500 °C.

Temperature	370 °C	390 °C	410 °C	430 °C	450 °C	470 °C	500 °C	530 °C
V/III = 2 (NW/ μm^2)				0.02	0.60	0.17	0.51	
V/III = 7 (NW/ μm^2)		0.57	0.25	0.70	0.28	0.27	0.20	0.72
V/III = 16 (NW/ μm^2)				0.40		0.14	0.34*	
V/III = 25 (NW/ μm^2)	0.33	0.29	0.25	0.34	0.47	0.34	0.35	0.53

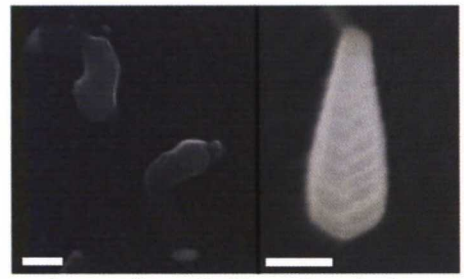

Figure 20: Growth along the surface (left) and pointing out of the surface (right). Images are taken at 15° angle. Scale bars are 100 nm.

Proportion of vertical NWs varied considerably on different samples that were grown with the same recipe and had the same preparations, but were grown on different growth sessions. This is probably due to varying success of oxide removal and to the amount of impurities on the reactor walls. Most of the samples also had areas with high and low proportions of vertical NWs. This can also be attributed to the oxide etching and Au deposition methods. Additionally, local variations in the precursor flows and in the temperature can also affect epitaxy [47].

Table 4 presents NW densities and yield of epitaxial NWs on the three different wafers. Each sample was etched in BHF for 15 seconds, and 37 % HCl was added to the Au solution which was put on the sample for 30 seconds. V/III ratio during the growth was 25 and temperature 430 °C. The NWs were grown in the same growth run on all wafers. The data was acquired from SEM images of 2-3 typical areas containing from tens to hundreds of NWs on each sample.

Table 4: NW densities and yields of epitaxial NWs on different wafers

	Reference wafer	4 ° miscut wafer	Highly doped wafer
NW total density (μm^{-2})	0.15	0.24	0.33
Epitaxial NWs	50 %	48 %	35 %

NW densities on the different wafers were typical on each wafer, whereas the yield was poorer with the highly doped wafer. Doping should not have a significant effect on epitaxy, since the dopant atoms are accommodated into the lattice. From the dopant concentration aspect, solid solubility of dopants to silicon can reach the order of 10^{21} cm^{-3} [17 p. 165], whereas Si lattice has 5×10^{22} cm^{-3} atoms [17 appendix A]. Thus, almost 10 % of the atoms can be of foreign material, which could have effect on the

seed particle, *e.g.* by forming an alloy with it. The highly doped wafers had also been stored for a prolonged period of time, which might have altered their surface.

Oxide etch time effect on the yield of epitaxial NWs was studied in two different runs, one on the reference wafer and the other on the highly doped wafer. On the reference wafer the longest tested etch time, 90 seconds, gave the best results, whereas on the highly doped the shortest etch time of 10 seconds was the best. This suggests that the etch time is not a decisive parameter in NW growth.

Effects of different Au NP deposition methods were tested by growing NWs simultaneously on substrates prepared with both methods. This was done in three different growth runs, and table 5 presents the results. The results are averages from six typical 150 – 300 μm^2 areas in each sample. Sample pairs 1 and 2 in table 4 had gallium deposited to the substrate before NW growth, whereas pair 3 lacked this step. These results indicate that the deposition methods are equally good when Ga is deposited, and without Ga the HCl method is better.

Table 5: Effects of Au NP deposition with HCl and PLL methods.

Growth run #	V/III – ratio	Temperature	Deposition method	NW density (μm^{-2})	Vertical NWs
1	7	450	HCl	0.21	43 %
1	7	450	PLL	0.42	39 %
2	25	430	HCl	0.34	40 %
2	25	430	PLL	0.34	42 %
3	25	450	HCl	0.38	65 %
3	25	450	PLL	0.20	30 %

Samples with the HCl Au NP deposition method were more homogenously covered with NWs, as shown in figure 21. This can be attributed to inhomogeneous deposition of PLL, thus some areas may have too much or too little PLL for the Au NPs to attach properly. On the other hand, some areas had higher density with the PLL method than was achieved with the HCl deposition method.

Figure 21: Typical sample surface after NW growth. Au NP deposition methods HCl (left) and PLL (right) are presented. On the dark areas fewer NWs have grown. Scale bars are 100 μm.

Effect of HCl concentration in the droplet added to the Au solution was tested with two samples with concentrations of 3 % and 37 %. pH-value of resulting solutions were tested with pH papers, and each solution had pH at the lowest value on the scale, which was 1. Besides the HCl concentration the samples had identical preparations and NWs were grown in the same run. NW densities and percentage of epitaxial NWs was calculated from six typical 150 μm^2 areas. NW density on both samples was 0.3 μm^{-2} with 3 % HCl and 0.24 μm^{-2} with 37 % HCl. Thus the NW densities were similar, and no effect could be accounted for the concentration. Degree of epitaxy was also similar for both samples, 43 % for 3 % HCl and 44 % for 37 % HCl. Thus, it can be concluded that already 3 % HCl concentration was enough to neutralize Au NPs, and that excess HCl caused no harmful effects to the growth.

4.2. Effects of growth parameters

4.2.1. Temperature and molar ratio

The studied effects of temperature and molar ratio included yield of epitaxial NWs, axial - and radial growth rates, and NW morphology. Studied temperature range was 370-560 °C and V/III ratios 2, 7, 16, 25, 35, 45 and 55 were included. Epitaxial NWs were grown with V/III ratios 2, 7, 16, 25 and 35, when the TMG molar flow was 10.8 µmol / min. However, with the V/III ratio of 35 most of the epitaxial NWs kinked during the first 60 seconds of growth. When total molar flow was lower, also higher V/III ratios yielded epitaxial NWs, as will be discussed in chapter 4.2.2. Also, only small areas on most samples with the V/III ratio 2 of had epitaxial NWs. Only the T = 430 °C sample in the V/III = 2 series had epitaxial NWs throughout the sample; however, their density was low. As a conclusion, growth window for epitaxial NWs was found to be approximately between molar ratios 7 and 35 with the used TMG flow.

Figure 22 presents the percentage of epitaxial NWs as a function of temperature for V/III ratios 2 (a), 7 (b), 16 (c) and 25 (d). Also SEM images of the V/III = 25 series are presented in figure 23. Molar ratios 7, 16 and 25 are within the growth window, thus results regarding them can be considered a general case, whereas results from the V/III = 2 provide only additional information. At low temperatures reactants in the seed particle have insufficient energy to find the locations with lowest energy, thus only small proportion of NWs grow epitaxially, as can be seen for molar ratios 7 and 25 in figure 22. Highest percentages of epitaxial NWs grow at a temperature range from approximately 450 °C to 530 °C, and the proportion decreases again at higher temperatures. This indicates that at about 450 °C the reactants have the energy needed to find favorable positions for epitaxial growth, and other factors such as surface defects become limiting. Data point with V/III = 7 and T = 500 was neglected in the considerations, as the low percentage is most likely due to failed surface preparations. At high temperatures the reactants have insufficient time to find the favorable positions before subsequent reactants arrive to the growth site.

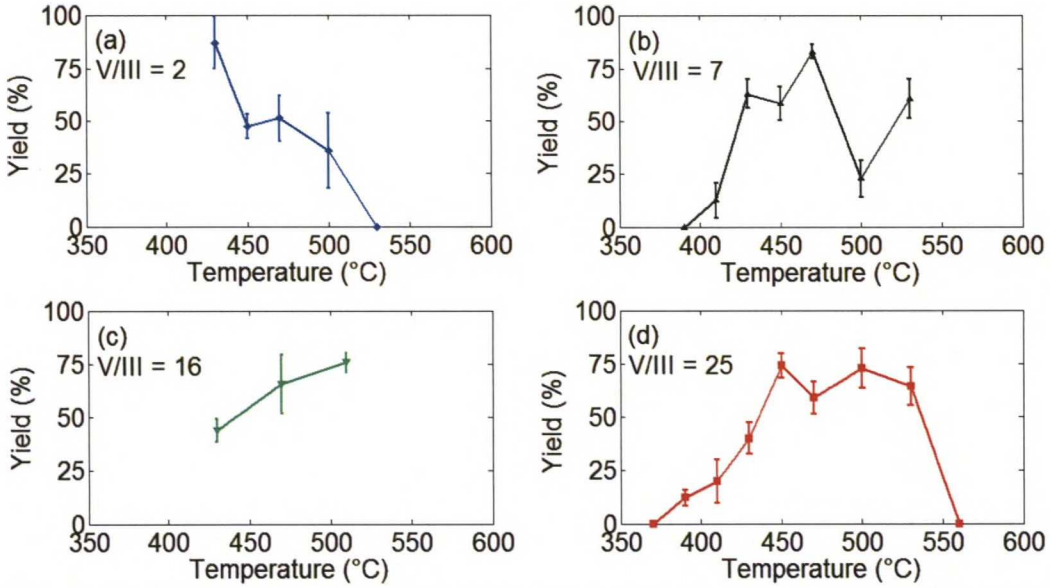

Figure 22: Yield of epitaxial NWs as a function of temperature for V/III ratios 2 (a), 7 (b), 16 (c) and 25(d). The error bars correspond to standard deviation in the data.

The yield for the V/III ratio of 2 has a decreasing tendency. However, as mentioned earlier, most Au particles on the sample grown at 430 °C seeded growth along the surface and only a small portion of them seeded epitaxial NW growth. Thus, the data point should have a lower value, whereupon the shape of the graph would be similar to that of other studied molar ratios.

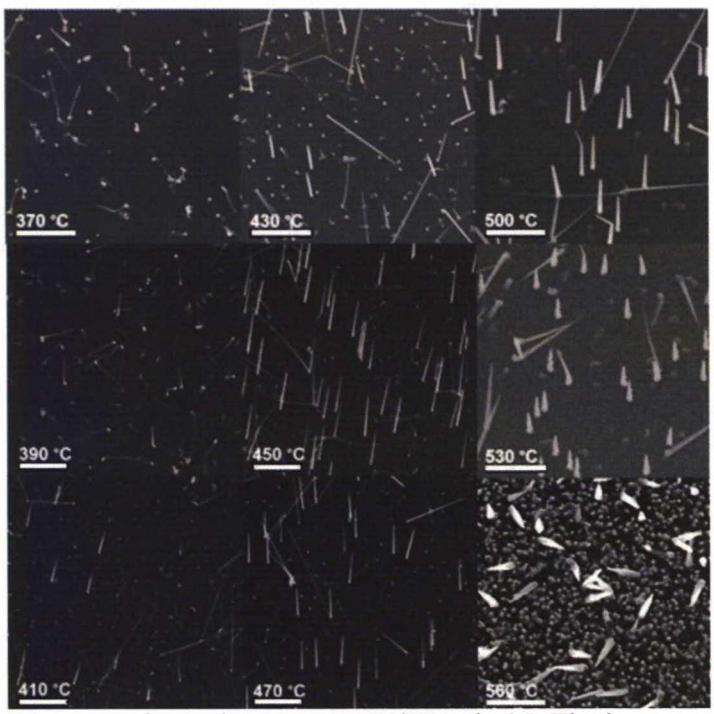

Figure 23: SEM images of samples grown at V/III ratio 25. The images are taken at 15° angle, and the scale bars correspond to 2 μm.

In general, much fewer NWs grew epitaxially with the V/III ratio of 2 than with 7, 16 or 25. Also this can be explained with a high proportion of Au NPs crawling on the surface, which were greater in size and numbers for a lower molar ratio. The increased probability for the NPs to seed growth along the surface can be due to the homogenous nucleation of group III species, which creates Ga islands on the surface, thus altering the surface properties. The results suggest that this promotes Au NP crawling, *i.e.* that crawling becomes energetically more favorable. Another explanation could be that the seed particle precipitates gallium at a faster rate than can be compensated with present As adatoms, thus leading to incomplete crystal formation under the seed and failure of epitaxy.

Axial growth rates as a function of temperature are presented in figure 24 for molar ratios 2, 7, 16 and 25. The growth rate increases with temperature up to approximately 450 °C, and decreases at higher temperatures. This behavior corresponds well to previous studies. With AsH_3 the peak growth rate was approximately 470 °C [29] [30] and with TBA approximately 440 °C [34 p. 66]. The increase up to 450 °C is due to a higher growth rate and more efficient precursor pyrolysis, after which planar growth becomes significant, as explained in more detail in chapter 2.4.2. The graph for V/III = 2 increases only slightly up to 470 °C and then remains almost constant. This indicates that at V/III = 2 the growth occurs at the mass-transport limited regime, for which minor dependence on temperature is typical [16 p. 31]. Limited amount of available reactants also diminishes the growth rate.

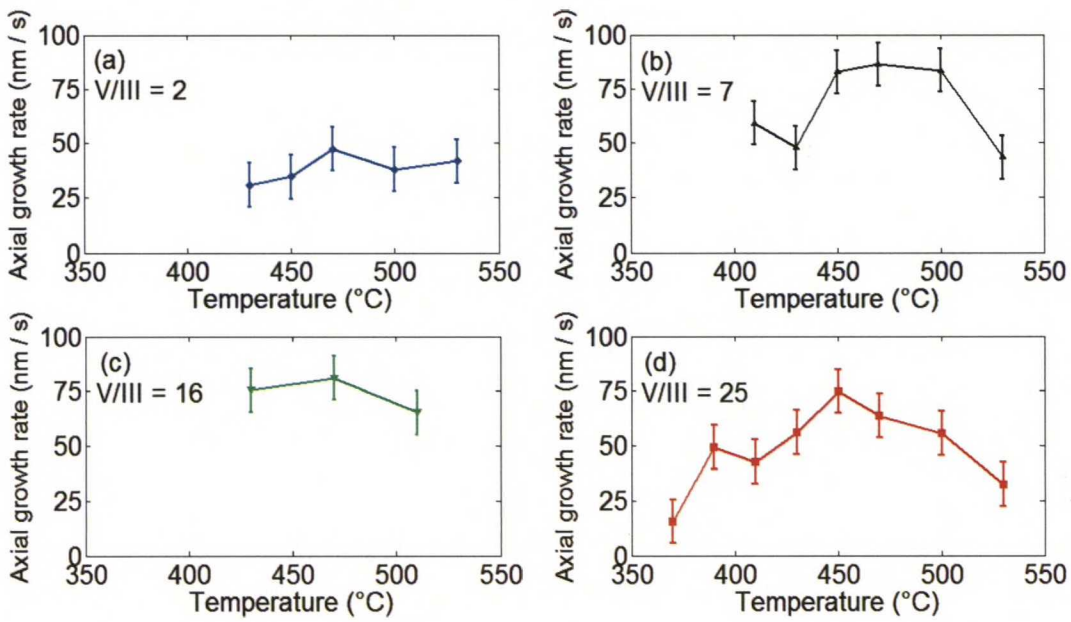

Figure 24: Axial growth rates as a function of temperature for V/III ratios 2, 7, 16 and 25. Error bars (10 nm/s) equal to largest variation between samples with identical preparations and recipes. Standard deviation was typically 1-2 nm/s.

From the figure 24 it is also apparent that at the V/III ratio of 2 the growth is slowest and increases at V/III = 7. This can be explained with the pyrolysis efficiency of the precursors. AsH_3 reaction species enhance decomposition of TMG [57], and using TBA instead of AsH_3 does not affect the pyrolysis efficiency of TMG [34 p. 66]. Thus, when TBA is more abundant TMG decomposition efficiency increases, leading to the faster growth rate.

The growth rate remains almost constant at around 70 nm/s for V/III = 16 and drops again for V/III = 25. As explained in chapter 2.4.3, excess As can form As-terminated (111)B surfaces on GaAs, hindering the axial growth. Also depletion of Ga from Au NP can cause solidification of the seed particle, which contributes in decreasing the growth rate. [57]

In general, growth rate during one run was approximately constant besides slight variation between dense and sparse areas. However, variation as high as 10 nm/s was observed in two samples that were grown on different days, even though preparations and growth recipes were identical. The difference could be due to varying atmospheric pressure, different Au NP densities, and different surface properties resulting from the inexact nature of sample preparation. One of the samples had significant amount of formations grown on the surface. The substrate surface affects pyrolysis of the precursors, thus it affects growth rate as well. Most of sample pairs grown on different days with identical preparations and recipes had variation of 3-4 nm/s, and the value 10 nm/s should be considered exceptional.

Table 6 presents comparison of the observed growth rate to that of reported previously with approximately same parameters. There is clear variation in the values reported by different groups, but the rates observed are significantly higher than any of the previously reported values.

Table 6: Comparison of growth rates reported elsewhere and observed in this study.

TMG flow (µmol/min)	V/III ratio	Temperature (°C)	Pressure (Torr)	Reported rate (nm/s)	Observed rate (nm/s)
12	46	450	75	~3.5 [43]	~50
10	7	440	100	~30 [26]	~83
50	20	450	100	~15 [29]	-
10	~7	440	38	3.44 [34]	~83

Figure 25 presents sidewall growth rates and tapering as functions of temperature for molar ratios 2, 7, 16 and 25. The sidewall growth rate, or radial growth, is presented as planar growth rate; the NW radius increased twice this rate. To measure tapering, a ratio between radial and axial growth rates was used:

$$tapering\ parameter = \frac{v_r}{v_a}, \tag{19}$$

where v_r is the radial growth rate and v_a is the axial growth rate. As was expected, sidewall growth becomes more substantial in higher temperatures. Almost no radial growth, only ~0.2 Å/s was observed at temperatures below 400 °C, and at 450 °C it remained at ~2 Å/s. At higher temperatures it became more significant, as growth conditions approached those suitable for planar growth.

Radial growth rate for the V/III ratio of 2 increases slower with increasing temperature than for higher V/III ratios. This also indicates that the growth with V/III = 2 is in the mass-transport limited regime, since the dependence of temperature is diminished. Observing the high-temperature regime, graphs with higher V/III ratio show more exponentially growing behavior. This suggests that at high temperatures mass transport plays a role for the other V/III ratios as well.

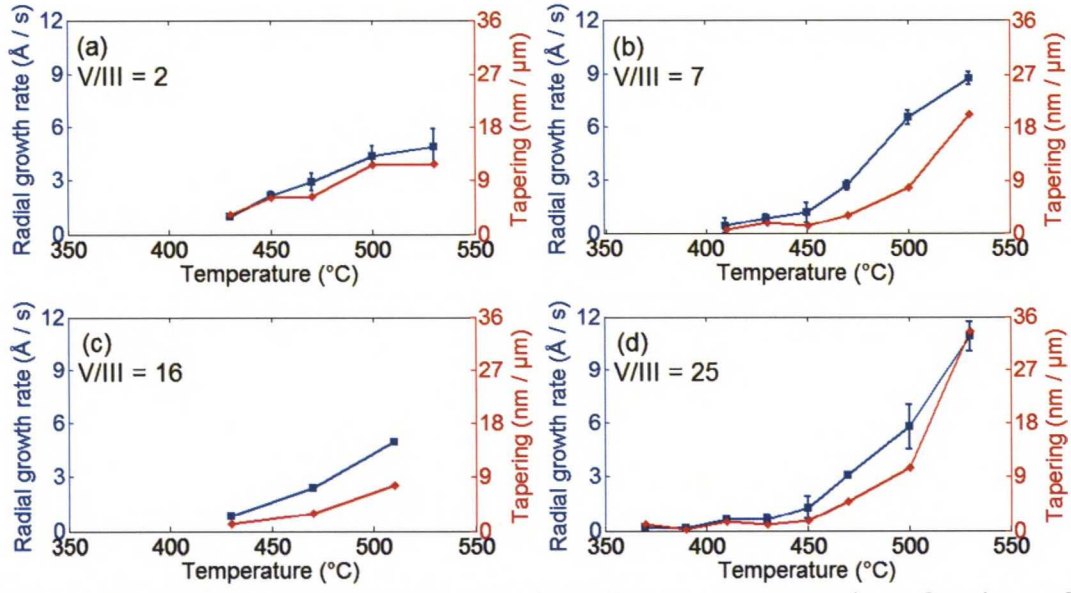

Figure 25: Radial growth rates (blue) and tapering parameters (red) as functions of temperature for V/III ratios 2 (a), 7 (b), 16 (c) and 25 (d). Error bars in growth rate graphs equal to standard deviation for each sample.

The behavior of the tapering is not affected by the molar ratio. For all of the studied ratios, tapering becomes increasingly apparent at high temperatures. The tapering in the studied NWs is smaller than reported previously. Joyce *et al.*reported NWs with markedly low tapering, e.g. 3 nm/µm on one side in NWs grown at 450 °C and with a V/III ratio of 23 [43]. In this study, tapering of 1.7 nm/µm was observed in NWs grown at 450 °C and with the V/III ratio of 25. Joyce *et al.*found that fast growth rate leads to lessened tapering [43]. This explains also the minute tapering observed in this study.

Temperature was found to affect also NW sidewall smoothness and kinking. Figure 26 shows SEM images taken at 90 ° view of NWs grown at a temperature range of 370 °C – 560 °C. Also close-ups from typical bases are shown. V/III ratio was 25 for samples grown at 370 °C, 390 °C and 560 °C, and 7 for the rest of the samples. Growth time was 60 seconds. Varying growth rate can be seen from the length of the NWs. At temperatures below 400 °C the bases have no well-defined shape and the NWs grow commonly to random directions. Tapering becomes significant at high temperatures, and sidewall profile becomes more undulating. The undulating behavior has been observed in a previous study [9] [74], and is explained by side faceting due to twin defects and surface tension at high temperatures [74].

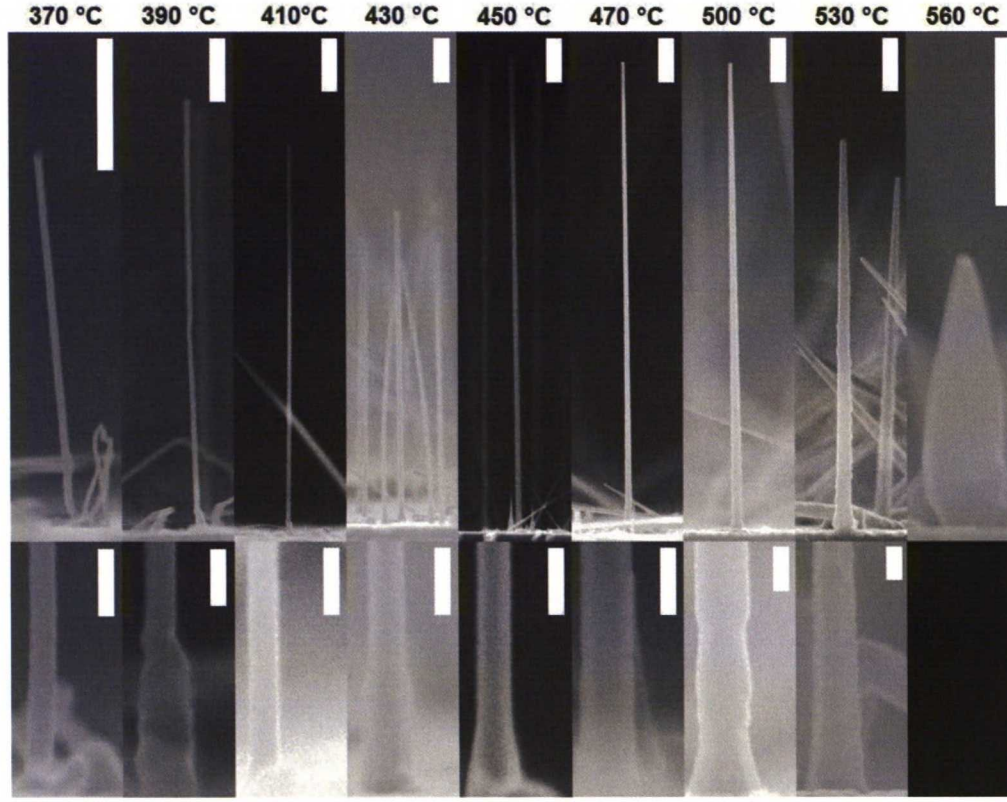

Figure 26: Side view of NWs (upper row) grown for 60 seconds at a temperature range of 370 – 560 °C. Also typical NW bases are shown (lower row). Scale bars are 500 nm in the upper row and 50 nm in the lower one.

Figure 27 presents yield of epitaxial NWs (a), axial growth rate (b), radial growth rate (c) and tapering parameter (d) as a function of V/III ratio. Temperature was 470 °C and the TMG molar flow was 10.8 µmol/min for all of the samples. The values were obtained from 5-6 typical areas or NWs from the samples, besides for the yield of V/III ratio 45, where only one typical area was studied. Error bars equal to standard deviations in yield and radial growth rate, and to 10 nm/s in axial growth rate.

Yield was highest for V/III = 7, and decreased for both lower and higher values. At molar ratios 45 and 55 no or little epitaxially nucleated NWs were observed, and the epitaxially nucleated ones kinked rapidly. Possible detrimental aspects of high molar ratio were discussed in chapter 2.4.3. and they included solidification of the seed particle and As-terminated growth interface. Both of these factors can prevent epitaxial growth of NWs. In a previous study a proportion of GaAs NWs grown on GaAs(111)B substrate became kinked at a molar ratio of approximately 90 [57], when TMG flow 12 µmol/min was used. The ratio is higher than observed in this study. The difference can be reasoned in part by different substrates, as epitaxy is easier to perform on similar materials. Also, low-pressure reactor was used in [57], which might cause differences as well.

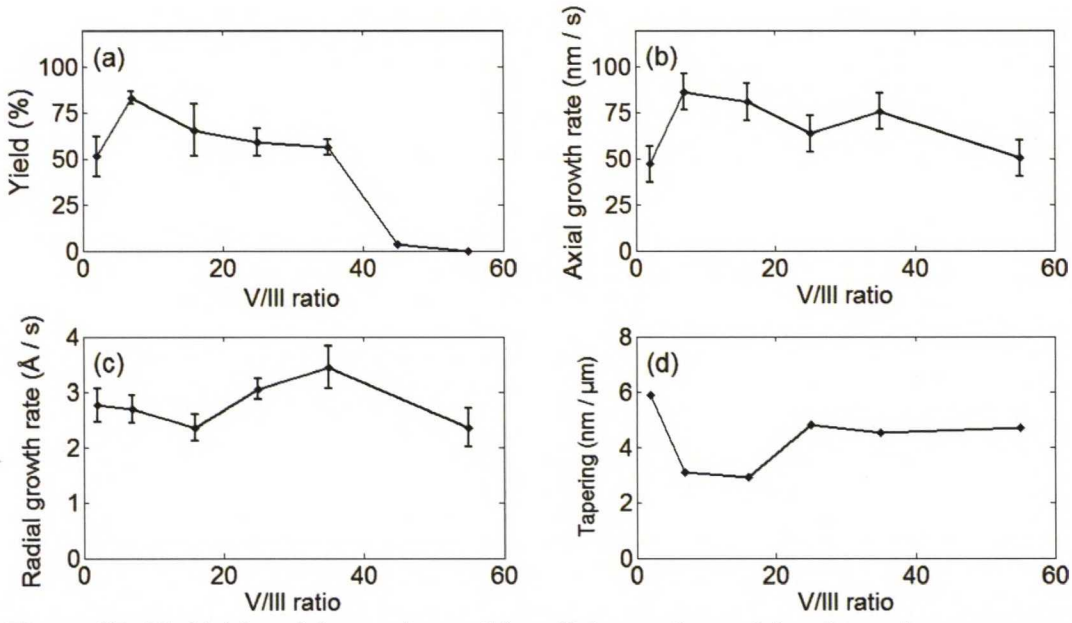

Figure 27: Yield (a), axial growth rate (b), radial growth rate (c) and tapering parameter (d) as a function of V/III ratio.

Axial growth rate is comparably slow at V/III ratio 2, then rises rapidly to V/III ratio 7 and then decreases again. The growth rate being slow with V/III ratio 2 can be explained with limitations in mass transport at low As concentrations. The decrease at higher ratios is due to As-terminated (111)B growth interface and solidification of the seed particle, as discussed in chapter 2.4.3.

The radial growth rate has increasing trend except for data points for V/III ratios 16 and 55. The growth rate for V/III ratio 55 was calculated from NWs that had kinked shortly after nucleation and were growing parallel to the surface. As growth occurred on the surface as well, proximity of the NW sidewalls was depleted from reactants to some extent, slowing the radial growth. Thus, the data point of V/III ratio for radial growth rate can be considered invalid, and the sidewall growth to increase with increasing molar ratio. This behavior was expected due to reasons discussed in chapter 2.4.3. and observed in previous studies [43] [57] [58] [59].

The axial growth rate was affected more significantly by increasing molar ratio than the radial growth rate. Thus, tapering depended mainly on the axial growth rate. The faster the axial growth rate was, the less tapered the NWs were, as figure 27 shows.

Morphology of the epitaxial NWs was unaffected by the V/III ratio below the onset of kinking at V/III = 35, as shown in figure 28a. However, the V/III ratio had considerable impact on the proportion of kinked NWs, as figure 28b shows. With a TMG flow of 10.8 µmol/min the kinking probability rose rapidly after the V/III ratio of 25. When kinking became significant, yield of epitaxially nucleated NWs declined as well. Images with lower molar ratios are not shown, but they were similar to the one with V/III = 25 with additional surface growth.

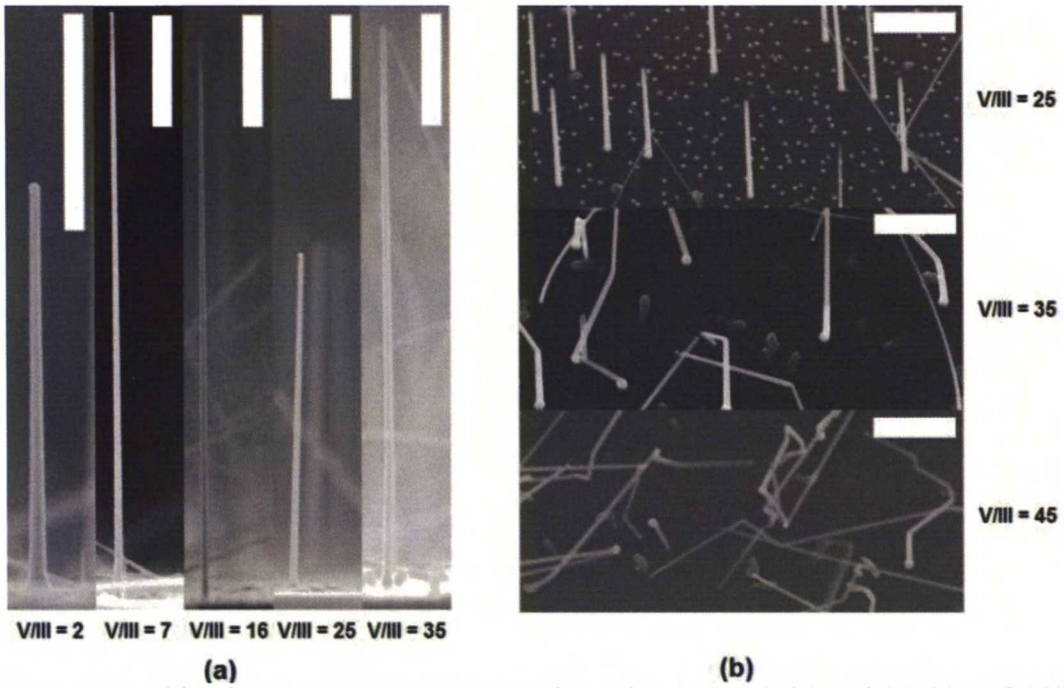

Figure 28: Side view on NWs grown at molar ratios 2, 7, 16, 25 and 35 (a) and 15° view on NWs grown at molar ratios 25, 35 and 45 (b). Temperature was 470 °C for all of the samples besides the one with V/III ratio 45, which was grown at 450 °C. Scale bars are 1 µm.

4.2.2. Total molar flow

Total molar flow was found to have a pronounced effect on the yield of epitaxial nanowires, as shown in figure 29a. The yield decreases rapidly after a critical value of TMG flow, which in turn depends on the molar ratio. As noted in chapter 2.4.4., total molar flow can be cautiously interpreted as a measure of supersaturation. Also, according to equation (14) the supersaturation increases when either of the precursor concentrations is increased. Thus, the results indicate that increasing supersaturation impedes the nucleation of epitaxial NW after a critical value is reached. In the used system the critical TMG flow is approximately 7 with the molar ratio of 25 and 1 or less with the molar ratio of 45.

As discussed in chapter 2.4.4., increasing supersaturation has been found to decrease twin defect density [43], as well as to increase it [61]. In case increasing supersaturation or total molar flow increases stacking fault density, *i.e.* causes unordinary nucleation at the growth interface to become more favorable, it could also lower nucleation to other crystal directions. Thus, increasing total molar flow would promote nucleation to other crystal directions and induce kinking to the nanowires, which was observed in this study.

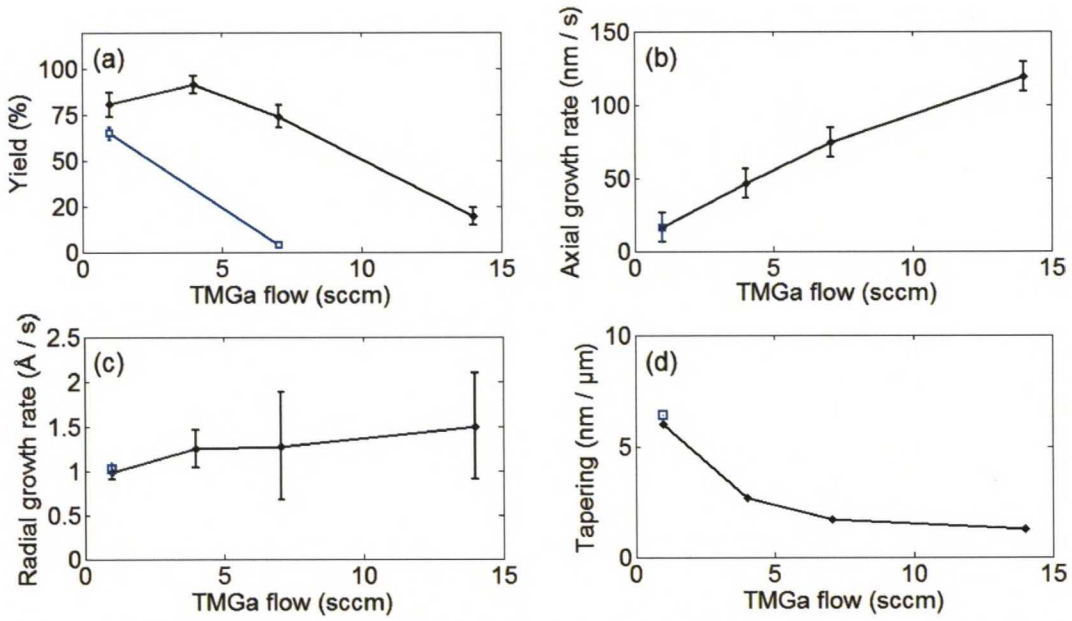

Figure 29: Yield of epitaxial NWs (a), axial growth rate (b), radial growth rate (c) and tapering parameter (d) as a function of TMG flow when V/III ratio was kept constant. Black graphs correspond to V/III ratio 25 and blue graphs or data points to V/III ratio 45. Error bars for yield and radial growth rates equal to standard deviations and for axial growth rate to 10 nm/s.

The axial growth rate increases dramatically with increasing total molar flow, as presented in figure 29b. The dependence is approximately linear with a slightly decreasing tendency at highest studied flow rates. The linearly increasing tendency with supersaturation was predicted in equation (15), though it considered chemical potentials only in the seed particle and in the growing facet. However, it is reasonable to assume that the tendency is similar also when III-V NWs are grown, *i.e.* one of the growth components arrives to the growth interface directly from vapor phase. The decreasing tendency at highest studied molar flows can be attributed to limitations in reaction rate at the used 450 °C temperature. Thus, the observed behavior fits well the theory.

The radial growth rate on the other hand, is relatively unaffected by the increased molar flow, as figure 29c presents. Similar behavior has been observed elsewhere, and was attributed to axial growth rate being mass-transport limited, whereas radial growth is kinetically limited [43]. Indeed, observing figures 24 and 25 it is obvious that the radial growth increases radically with temperature, whereas the axial growth rate is diminished at higher temperatures due to depletion of reactants. Thus, the same reasoning explains the observed behavior in this study. From this follows also the decreasing tapering observed in figure 29d.

4.2.3. Growth time

Nanowire length as a function of growth time is presented in figure 30. The dependency is linear, which was predicted in discussions in chapter 2.4.6. and has been reported in previous studies [26] [29]. The linear fitting with the least-squares method crosses

growth time axis at circa 0.25 s, which suggests that the NW growth begins after only quarter of a second after the introduction of precursor gases. This is faster than the value of a few seconds reported elsewhere [26] [29]. The difference is probably due to the Ga introduced to the reactor and thus to the seed particles before the actual growth step. The linear dependence allows good control of nanowire length for different applications.

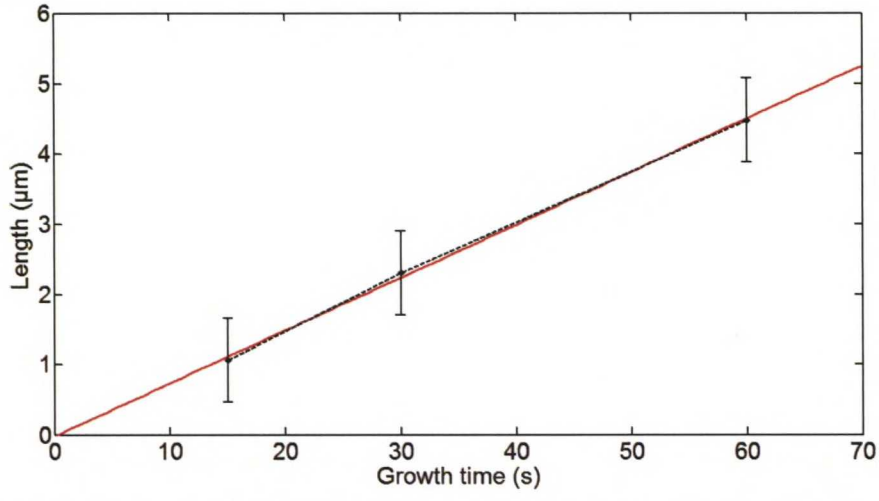

Figure 30: NW length as a function of growth time (black) and a linear least squares-fitting to the data (red).

4.3. Crystallography

4.3.1. TEM characterization

Crystal structure, orientation and quality were investigated with TEM in this work. Figure 31 presents images from two different NWs. Figures 31 a-c present a tip (a), a segment with a stacking fault (b) and an electron diffraction pattern (c) of one NW while figure 31d shows the tip of another. The NW in figures 31 a-c is referred to here as the first NW and the NW in figure 31d as the second NW. The studied segment of the first NW was approximately 10 µm long, and only one twin plane was observed after the neck region, demonstrating high crystal quality. The diffraction pattern corresponds to zinc blende [86 p. 36] with lattice constant a = 0.565 nm, which is characteristic for cubic GaAs. The growth direction was identified as [111], which was expected for epitaxial NWs on (111) surface.

The neck region of the 1st NW decreases in diameter and has high density of defects. The neck region forms during the cooling period after the actual growth, as Ga atoms are depleted from the Au particle in As-rich atmosphere. Thus, Ga concentration in the Au particle is decreased to the equilibrium value. The growth of the neck region then occurs at lower temperature, as well as with lower supersaturation. However, the Ga atoms are depleted quickly compared to the pace of cooling down. Thus, the main contributor to the observed high twin plane density is low Ga supersaturation in the Au particle. This in turn indicates that high supersaturation is beneficial in the system used in this work.

For the 2nd NW, characteristics of the neck region and the Au particle differ from the 1st NW. First, the neck region is similar to the rest of the NW with only minute decrease in diameter. Second, the Au particle diameter is notably larger than the NW top diameter, whereas in the 1st NW the difference is smaller. The diameters in the 1st NW are 33.7 nm for the NW top and 39.8 nm for the Au NP, and in the 2nd NW 39.8 nm for the NW top and 60.8 for the Au NP. This indicates that the growth has ceased after the TMG flow was switched off, and the Ga remained in the NP. This would explain the larger NP diameter and unchanged morphology in the neck region. It would be unexpected that the growth would cease at typical growth temperatures, but the cease could be due to an As-terminated growth interface after supersaturation in the Au particle was lowered.

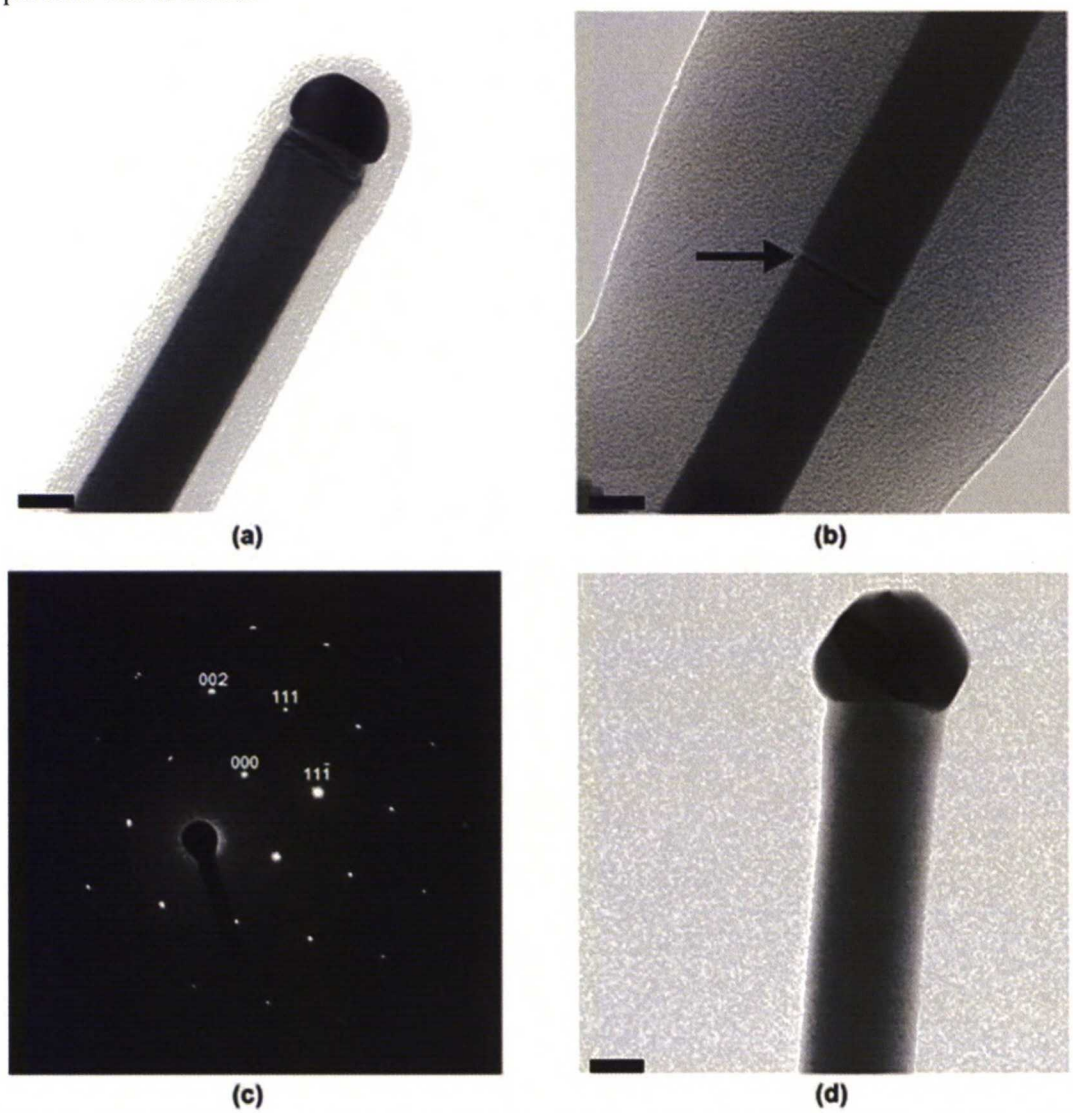

Figure 31: TEM images of the tip (a), a segment with a twin plane (b) and electron diffraction pattern (c) of one NW and the tip of another (d). Scale bars are 20 nm.

Also a GaAs/AlGaAs CS NW was characterized with TEM. The core was grown at 450 °C with V/III = 25 for 5 minutes and the TMG flow was 10.8 µmol/min. The shell was grown at 650 °C with the same TMG and TBA flows, and in addition with a TMA flow of 15.8 µmol/min. Figure 32 presents a segment of the core-shell NW with a twin plane (d) and diffraction patterns above the twin plane (a), at the twin plane (b) and below the twin plane (c).The diffraction pattern above the twin plane was a mirror image from the pattern below the twin plane, as expected [86]. The crystal directions above the twin plane are marked with orange, and the ones below with white and the common directions for both with yellow. At the twin plane crystal directions from both sides are visible.

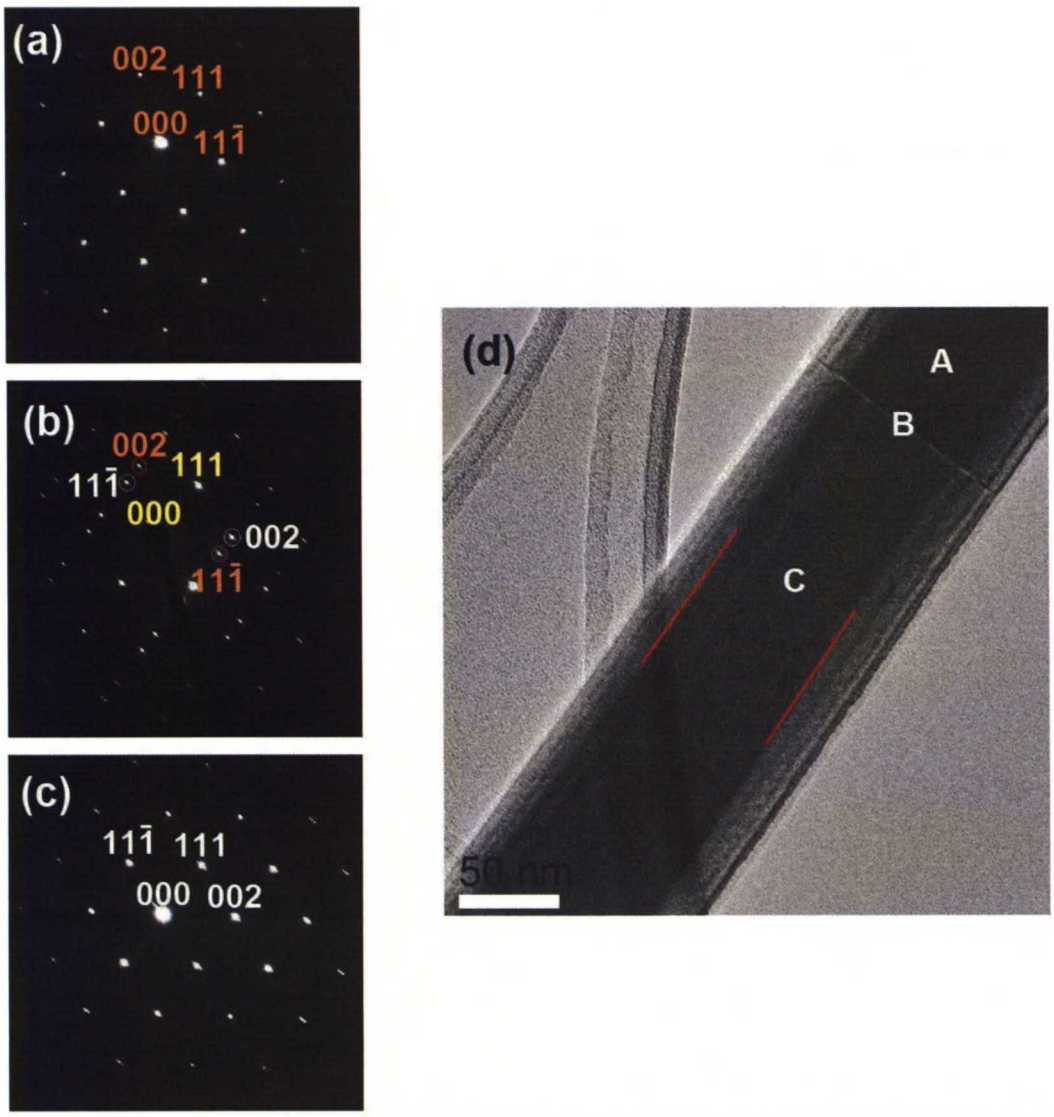

Figure 32: Electron diffraction patterns above a twin plane (spot A) (a), at the twin plane (spot B) (b) and below the twin plane (spot C) (c), and a TEM image of the CS NW (d). The directions above the twin plane is marked with orange, below with white and common directions for both with yellow. Scale bar is 50 nm.

The core-shell structure can be identified from figure 32d. There is a clear contrast between the core (between the red lines) and the shell (outside the red lines). The thickness of the core was 75 nm and the shell was approximately 20 nm thick. Also an EDS analysis was performed at the shell, and the proportions were 12.57 ± 0.04 % aluminum, 33.59 ± 0.02 % gallium and 53.84 ± 0.01 % arsenic. The As proportion was over 50 %, thus the composition measurement was inaccurate, or the As-terminated surface contributed to the proportion over 50 %. These values were used to estimate the compositions in other AlGaAs shells grown in the study.

4.3.2. Kinking directions

A high proportion of kinked NWs (figure 33) was observed in a part of one sample grown at 500 °C and V/III = 25. The kinking being significant only in a part of the sample suggests that it was caused by local variations in gas flows. The proportion of kinked NWs was observed to increase slightly at higher temperatures, thus variations in temperature have a small contribution. However, as shown in chapter 4.2.2., high supersaturation leads to high probability of kinking, thus the local variations in the precursor flows are a more probable cause.

Figure 33 shows a top view of an area with kinked NWs. The NWs kink to six directions with 60 ° angle to the neighbors. Also, from 90° images it was clear that the NWs kinked only upwards. Thus, the kinking directions are the other three available {111} directions. This indicates that the NWs either nucleated to {111}A direction and eventually kinked to the favorable {111}B direction, or they started with {111}B as would be expected, and kinked to {111}A at the prevailing conditions. The NWs kinking to six directions can be explained with twin planes altering their orientation [31 p. 27], which was seen also in figure 32.

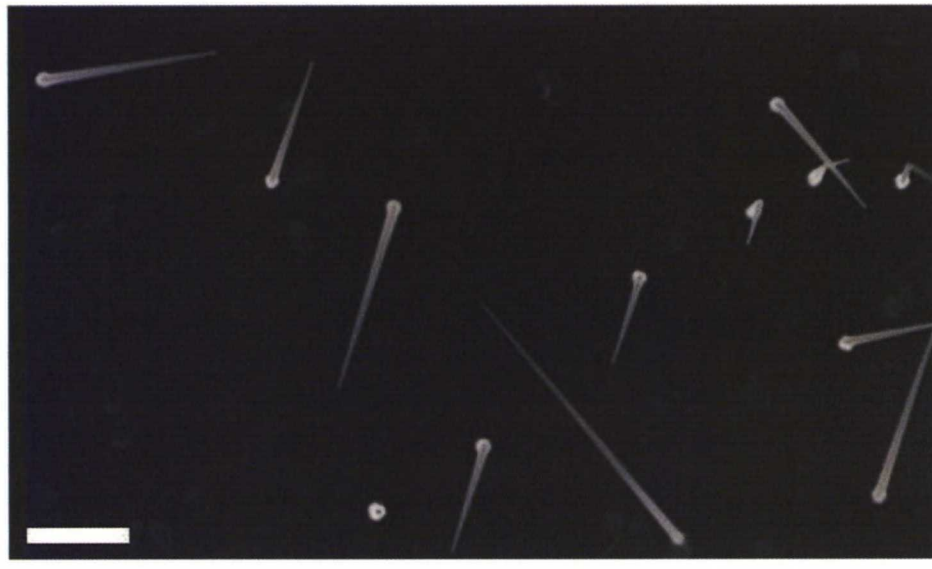

Figure 33: Top view on kinked NWs. A NW without kinking is located down left in the image. Scale bar is 1 μm.

4.4. Photoluminescence

4.4.1. GaAs/AlGaAs core-shell nanowires

GaAs NWs without passivation showed no PL signal in the measurements even when laser intensity was increased tenfold from that of used with CS NWs. This was an unexpected result, as the stacking defect density was low in the studied NWs, and PL signal has been acquired from bare GaAs NWs elsewhere [56] [71] [75]. The stacking defects act as effective centers for nonradiative recombination, which quenches the PL intensity [71]. Nevertheless, the NWs measured in earlier studies were also plagued by stacking defects [56] [71]. Thus, they are not sufficient to explain the lacking PL signal. Other possibilities include carbon impurities, which are common in MOVPE growth, and silicon incorporation. Silicon alloys with the Au seed during the oxide removal step and can be incorporated to the NW during the growth.

Optical properties of the NWs were studied by coating them with different materials, such as AlGaAs. PL measurement results at 20 K of GaAs NWs grown at 450 °C for 300 s with different shell compositions are presented in figure 34a. The EDS measurement showed 12.57 % aluminum and 33.59 % gallium, thus group III proportions were x_{Al} = 37.4 % and x_{Ga} = 62.6 %. Other compositions were calculated comparing the molar flows of TMG and TMA in the measured sample to the other samples, and the composition was assumed to depend on mass transport with equation (12). All shells were grown at 650 °C and the TMG flow was 10.8 µmol/min besides for the one with x_{Al} = 8.3 % the TMG flow was 17.6 µmol/min due to limitations in MFCs.

Figure 34a shows that the PL peak position blueshifts slightly from x_{Al} = 15.5 % to x_{Al} = 21.9 %, and redshifts thereafter with increasing x_{Al}. The different behavior with x_{Al} = 15.5 % is probably due to the use of different TMG flow. The observed redshift is an unexpected result, as the GaAs band gap is 1.518 eV at 20 K according to equation (2), and 2.24 for AlAs. Also, previously reported values for the PL peak in GaAs/AlGaAs NWs has varied between 1.477 eV and 1.517 eV [30] [43] [54] [57]. The redshift to 1.477 eV was previously attributed to strain [30] [54]. The strain effect was observed also in the present work; PL peak redshifted 5 meV when the growth time of the shell was increased from 20 s to 57 s with shell composition x_{Al} = 21.9%. The PL peaks with lowest aluminum composition are similar to previously reported values, and the peak positions could be due to strain. Breadth of the peaks can be attributed to observed variations in NW thicknesses and density. The density might affect the composition, as one of the group III materials might be mass-transport limited to a higher degree, and thus be depleted to a greater extent in dense areas.

However, due similar lattice constants of GaAs and AlAs, strain effects are not sufficient to explain the observed redshift up to 110 meV at higher Al proportions. Also possible Al diffusion to the core can be ruled out, as it would increase the band gap instead of decreasing it. Another explanation that was considered was transitions from the AlGaAs conductance band to the GaAs valence band (type II transition). This type of transition has previously been observed in axial heterostructure GaAs/GaAsSb/GaAs NWs [87]. Energy for the transition was acquired by deducting the valence band offset (equation 7) from the AlGaAs band gap in the Γ- and X-valleys. The AlGaAs band gap was calculated directly with the AlGaAs Varshni parameters from table 1, with equation (2), as well as with GaAs and AlAs Varshni parameters with equations (2) and (4). Both

calculations gave approximately the same results. Figure 34b presents the AlGaAs band gaps in the Γ- and X-valleys, the corresponding transition energies from the AlGaAs conduction band to the GaAs valence band, and the experimental results. The energy of the proposed transition is approximately 400 meV higher than observed in the PL study. The shape of the curve is similar, but the measured curve bends downwards at lower compositions. It can be concluded that this type of transition is a very unlikely explanation due to large difference in the observed energy, unless the materials are appropriately doped.

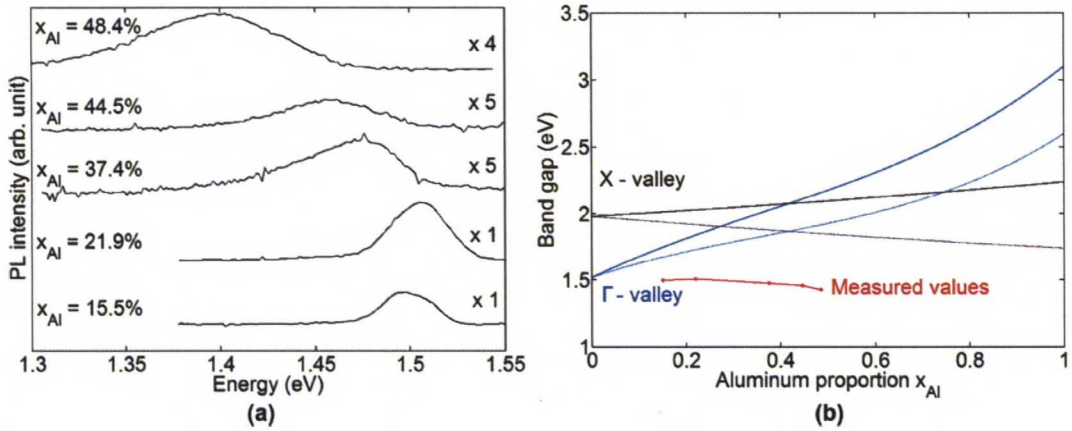

Figure 34: PL spectra for GaAs/$Al_xGa_{1-x}As$ NWs with varying shell composition (a), and band gaps (solid line) in Γ- (blue) and X-valleys (black) with energy gaps between AlGaAs E_C and GaAs E_V (dashed line) and measured values (red) (b).

Figure 35 shows band diagrams of intrinsic GaAs and n-type AlGaAs apart (a) and after contact in equilibrium (b). The Fermi level is aligned throughout the junction, which causes the bands to change their relative positions. The band gaps on each side remain constant until the heterojunction, and the exact heterojunction position is closer to the more heavily doped side of the junction [88 p. 230-231]. From figure 35b it is apparent that the conduction band minimum can be lower in AlGaAs than in GaAs.

The relative positions of the conduction bands depend on Fermi levels on each side at the junction. There is little difference in intrinsic GaAs/AlGaAs junction, as figure 35a shows. This small difference is and unlikely to cause enough variation to explain the observed redshift. Nevertheless, in case AlGaAs was sufficiently n-doped or GaAs p-doped, type II transition could explain the observed values.

Carbon doping is inherent in MOVPE growth, and carbon impurities have previously been identified as the dominant impurity in GaAs NWs, and it was found to act as an acceptor. [43] Carbon is a group-IV element, and therefore it can act as a donor or an acceptor depending on its site in a III-V lattice. In case the carbon impurities would occupy group III sites in AlGaAs, it would shift the AlGaAs E_C lower in relation to the GaAs E_C. However, this kind of doping is not expected.

At the GaAs/AlGaAs heterojunction the GaAs E_C bends downwards and the AlGaAs E_C upwards. Thereby a triangular potential well is formed on the GaAs side with a typical thickness of <10 nm. This structure leads to a high concentration of electrons in the triangular potential well, whereas the AlGaAs side of the junction is depleted. [89 p. 141-142] This potential well can have its bottom at a lower value that

GaAs E_C. However, the triangular QW bottom is relatively close to the GaAs E_C, as has been previously measured. The band gap has been observed to shift only a few meV when the transition occurs between the QW and GaAs E_V [90].

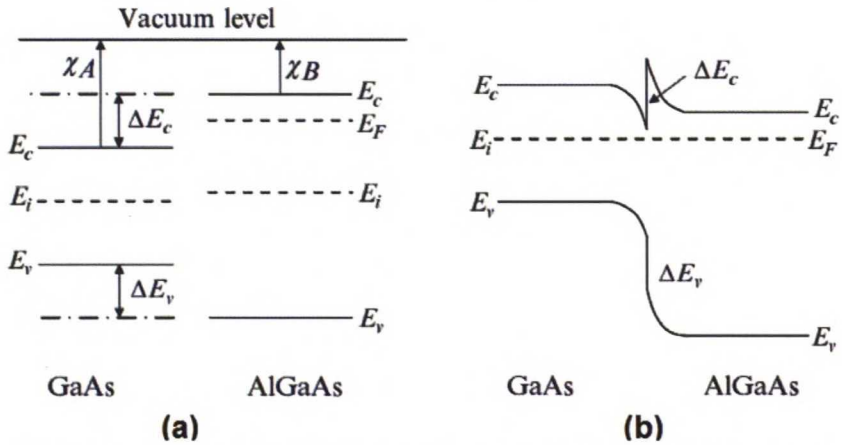

Figure 35: GaAs/n-AlGaAs heterojunction before (a) and after (b) contact [89 p. 141].

Another possible explanation is quantum effects, as they have been observed with up to 15 – 35 nm thick GaAs NWs [85]. In case Al diffuses significantly to the GaAs core, it can decrease its diameter. Thus, it could form a QW within the NW. Higher aluminum concentration would increase the diffusion depth, thus the QW width would decrease at higher TMA flows. However, this would cause a blueshift in PL signal, and therefore does not explain the results.

To investigate whether the signal was indeed from the NW core, a series was made with varying core composition and unchanged shell deposition parameters. The calculated shell composition was 21.9 % for all samples. The studied NW core compositions and the PL peak positions are presented in table 7. The aluminum proportions were calculated from the PL peak positions with equation (4). The NW with low TMA flow during the core growth showed two peaks with corresponding x_{Al} = 3.6 % and x_{Al} = 16.8 %. The peak corresponding to higher x_{Al} is expected to originate from the shell. As the aluminum composition corresponding to the rest of the peaks increases with increasing TMA flow during the core growth, it can be concluded that the signal was indeed from the core. The discrepancy of the calculated value of 21.9 % and the one found from PL measurements can be attributed to general inaccuracy of EDS and to possible deviations of from the assumed linear TMA / (TMA + TMG) molar ratio dependency. It is also noteworthy that no signal from the shell was seen other samples, indicating efficient electron transfer from the shell to the core.

Table 7: PL peak positions and corresponding x_{Al} for CS NWs with varying core composition.

TMA flow during core growth	PL peak position	Corresponding x_{Al}
None	1.506 eV	0
Low	1.577 eV, 1.717 eV	3.6 %, 16.8 %
Moderate	1.640 eV	7.6 %

Also the effect of shell deposition temperature was studied with x_{Al} = 48.8 % shells, and the measured PL signals at 20 K are presented in figure 36. Composition of tertiary semiconductors is expected to vary with temperature, which explains the variation of the peak position. The intensity results indicate that optimal growth temperature for the shell is around 650 °C. Another noteworthy observation is the peak position difference of 30 meV for the shell grown at 650 °C in figures 34a and 36. This difference shows that the shell growth at high TMA flows is plagued by variations in different growth runs, and has poor repeatability.

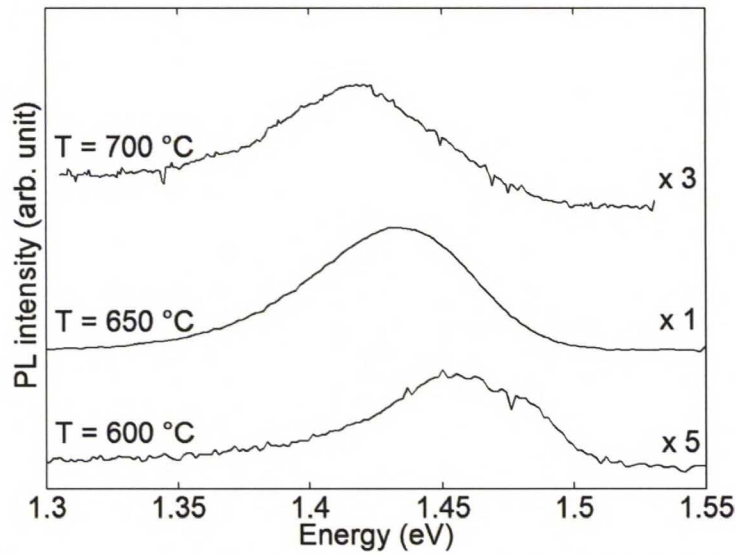

Figure 36: PL spectra at 20 K for CS NWs at shell deposition temperatures 600, 650 and 700 °C. The TMA flow was the same in all of the growth runs, and shell composition of x_{Al} = 48.8 % was estimated at 650 °C.

PL measurements at a temperature range of 20 – 200 K was performed on the CS NW with shell x_{Al} = 21.9 % and figure 37a presents the results for 20 – 170 K. The PL intensity decreased when temperature was raised, as was expected. The intensity at 200 K was only 1 % from that of at 20 K. It is noteworthy that no signal was seen in the nonpassivated NWs, but even 1 % of the signal from the passivated signal was detected even with high laser intensity. Thus it can be concluded that the passivation increased the intensity of the PL signal by several orders of magnitude. Besides the intensity, also the band gap decreased at higher temperatures. The shift in the PL peak was compared to the theoretical values given by equation (2), and the results are presented in figure 37b. Besides the offset of 10-20 meV the measured values agree well to the theory.

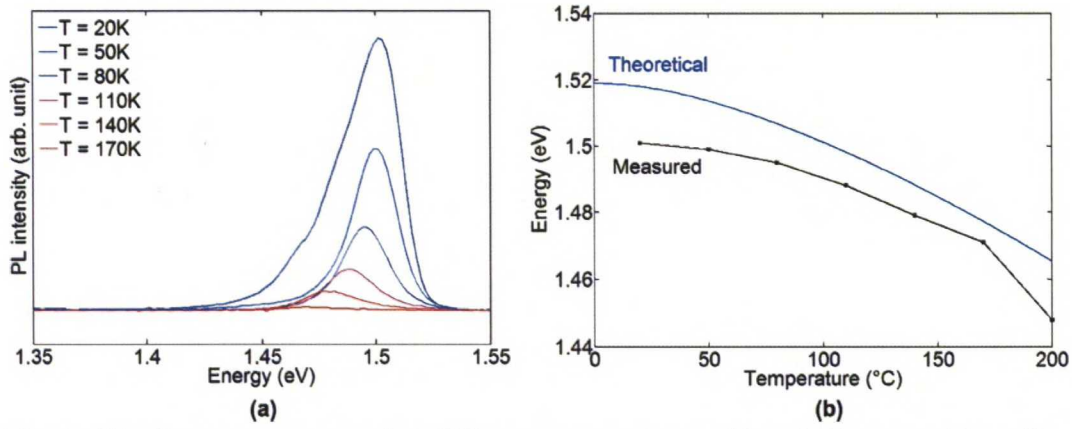

Figure 37: PL spectra measured at different temperatures with a shell composition of $x_{Al} = 21.9$ % (a), and the GaAs band gap dependency on temperature with measured (black) and theoretical (blue) values (b).

4.4.2. GaAs/GaAsP core-shell nanowires

Figure 38a presents 20 K – PL spectra for GaAs/GaAs$_{1-x}$P$_x$ NWs. All of the NWs were measured from 600 nm to 1000 nm (only peak positions are shown). When the same measurement values were used, highest intensity from GaAs/GaAsP NWs was approximately 25 % of the highest value for GaAs/AlGaAs NWs. This indicates that AlGaAs provided better passivation in the studied NWs.

The compositions were acquired from EDS which was performed with a SEM. Thus, the EDS results gave signal from both the core and the shell of the NWs. EDS was performed on a NW with a GaP shell and without any shell. Ga proportion in the core was calculated from the relation As / (P + As) with the results from the GaAs/GaP NW. Assuming that there was equal amount of Ga and As in the core, this gave the amount of As in the core as well. This Ga proportion was used to estimate the amount of As in the core for the measured GaAs/GaAs$_{1-x}$P$_x$ NWs. Then, the amount of As in the core was deducted from the total measured amount to get the amount of As in the shell, which was needed to calculate x_P in the shell.

The composition was estimated also with equation (12). Distribution coefficient value $K = 1/6.3$ was taken from an earlier study with the same MOVPE system, which regarded InGaAsP quantum wells [22 p. 26]. This gave a lower GaAsP shell x_P value of 11.5 % and a higher of 38.5 %. The difference is attributed to estimations done with calculations from the EDS data, as well as difference in distribution coefficient due to different growth parameters and geometry. In the following discussion directly measured EDS data is assumed to be closer to actual values.

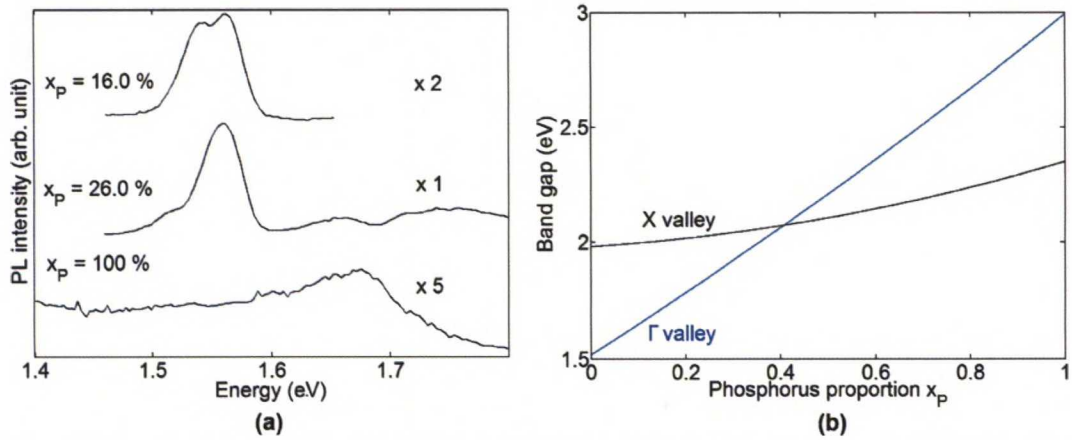

Figure 38: PL spectra from GaAs/GaAsP NWs with varying P concentration in shell (x_P) (a) and GaAsP Γ-valley (blue) and X-valley band gaps as a function of x_P (b).

The NWs with a shell of x_P = 16 % and x_P = 26 % have their highest peaks at 1.562 eV accompanied by another peak at 1.542 eV and 1.516 eV, respectively. GaP has a smaller lattice constant than GaAs, thus the NW core is under compressive stress, which causes the PL signal to blueshift. The higher peaks are proposed here to origin from the strained core, and the shoulders at slightly lower energies from carbon impurities. The carbon impurity signal has been observed with AlGaAs shells between 1.48 eV and 1.50 eV [43] [57], and they could also have shifted due to strain. The core peaks were observed to shift slightly on different measurement spots on the samples, thus the core peaks having the same value can be explained with variations in growth conditions. The radial growth is the preferred route for carbon incorporation [43], thus the difference in carbon peak positions is probably due to different shell deposition parameters.

Also peaks at higher energies were observed. The sample with the shell of x_P = 26 % had two broad peaks with low intensity at ~1.65 eV and at ~1.75 eV. The existence of two peaks is probably due to variations in the shell thicknesses and compositions. Reactions with the group III element are expected to be mass-transport limited, thus in dense areas the vicinity of the NWs is depleted from Ga during the shell growth, leading to variations in the growth rate and in the thickness. Composition variations were observed in the EDS measurements. The variation in the composition could be due to one of the group V elements being depleted to greater extent than the other due in the dense areas. The explanation of local variations is supported by the breadth of the peaks.

Regardless the origin of the two peaks, both are in the direct band gap region, *i.e.* at the Γ-valley. To identify the observed peaks, figure 38b presents $GaAs_{1-x}P_x$ Γ- and X- valley band gaps at 20 K as a function of the P concentration x_P. The band gaps were calculated with equations (2) and (3). According to figure 38b, $GaAs_{1-x}P_x$ has a band gap of 1.866 eV with x_P = 26 %. Considering that the shell is under tensile stress due to comparable dimensions with the core, the 1.65 – 1.75 eV peaks in the sample with the shell x_P = 26 % correspond rather well to the theoretical value. Thus, these peaks are considered to originate from the shell.

The signal from the GaAs/GaP NW peaks at 1.675 eV. Signal from the shell would be at over 2 eV and in the indirect band gap region, thus it can be ruled out. In

previous reports a GaAs/GaP NW core has been found to luminate at approximately 1.77 eV [76], which is close to the observed value. The peak position was previously attributed to strain [76], and as strain is dependent from the NW dimensions, also band gap depends on it. Thus, the observed signal is assumed to be from the NW core.

Intensity of the peak with the GaP shell was notably lower compared to the other ones, and it had a long tail on the low-energy side. The low intensity is attributed to a thin shell, which might not provide sufficient energy barrier to passivate the NW. The tail could be explained in part by shell thickness variations, and thus strain variations. However, as the tail continues below the GaAs band gap energy, it is considered to be a measurement artifact.

4.4.3. ALD passivated nanowires

ALD passivation efficiency was studied by coating GaAs NWs grown at 450 °C and 470 °C with 2 Å and 5 Å thick AlN layers. The studied NWs grown at 450 °C were annealed at 650 °C after the growth, which was found to result in a slightly higher PL signal. Figures 39a-d present the PL spectra at 15 K, with the NW growth temperature and AlN thickness given in each figure. The graphs show peaks at two locations; approximately at 1.51 eV and at 1.46 eV. In an earlier study, a GaAs PL signal was measured at 18 K, and an exciton peak was observed just below 1.52 eV and a carbon-related donor-acceptor recombination peak between at ~1.49 eV [43]. The observed values correspond rather well to the previously reported ones [43], only with a slight redshift.

Total intensity of the two peaks is approximately constant. This indicates that an approximately same number of electrons are excited in each sample, but the recombination path varies between the samples. The proportion of recombination via either path is expected to depend on the number of carbon-induced states. All of the samples had the same precursor molar flows, thus the formation of the carbon-induced states appears to depend on uncontrollable factors in the MOVPE growth. The increasing bottom line in each graph results from high laser intensity, which was found to produce such an artifact with the used setup. Also in the earlier study the exciton peak was vanished as the carbon peak became dominant [43].

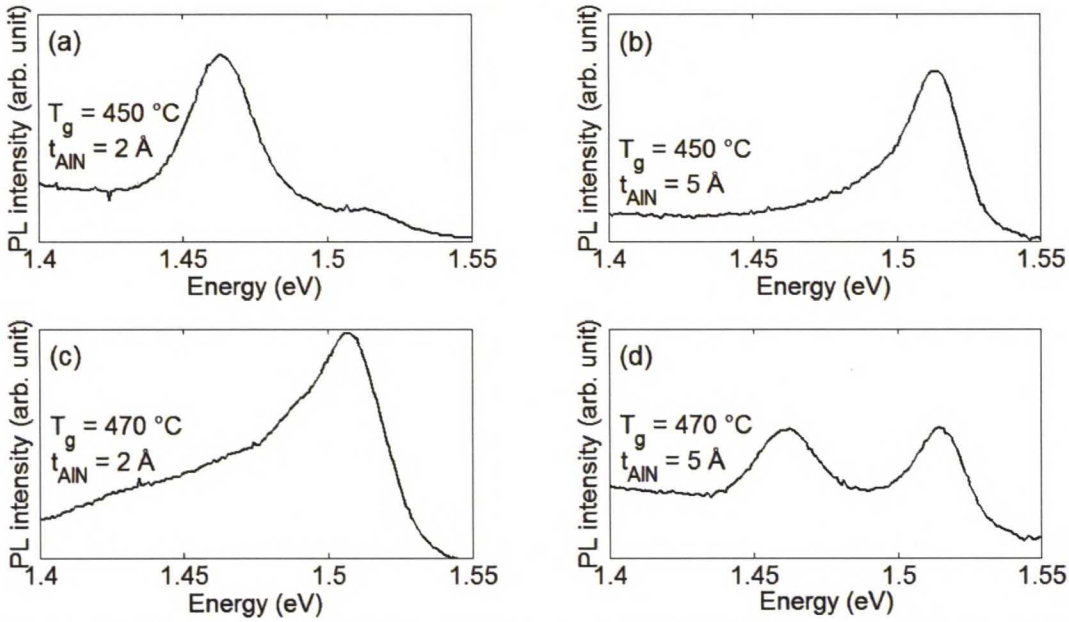

Figure 39: PL spectra at 15 K from NW grown at 450 °C (a,b) and 470 °C (c,d) with 2 Å (a,c) and 5 Å (b,d) thick AlN coating. The intensity scale is the same in each graph.

PL signal was measured also from AlN coated NWs without the oxide removal step before ALD. In this case no signal was seen, indicating that the oxide-induced trap states remained in effect after ALD coating, as was expected. Thus the oxide removal step was verified necessary. The oxide removal was also found to remove Au NPs from the tips of the NWs. The removal of the Au NP can be useful when thick shells are grown and no simultaneous axial growth is desired.

5. Conclusions

In this work GaAs NWs were grown on silicon substrates with an atmospheric pressure reactor MOVPE at different temperatures, V/III ratios, total molar flows and for different times. The NWs were seeded with Au NPs that were deposited from a colloid solution with HCl-assisted deposition method. Also different Au deposition parameters were investigated. The effects of the growth and deposition parameters on growth were studied with SEM, the crystallographic parameters and quality with TEM, optical properties with PL measurements and chemical compositions with EDS.

Different Au NP deposition methods and different wafers were tested by growing NWs with consistent growth parameters. Yield of epitaxial NWs was similar with the HCl and PLL methods, and from the wafers the highly doped one showed poorer yield. Density of the NWs varied between 0.2 and 0.7 NW/μm^2.

Temperature effects were studied at a temperature range of 370-560 °C with a V/III ratio of 25 and with narrower ranges with V/III ratios 2, 7, 16, 35, 45 and 55. The growth temperature affected the yield of epitaxial NWs, which were successfully grown between 390-530 °C. The yield increased up to circa 450 °C and was approximately constant until 560 °C, where epitaxy failed again. With TMG flow of 10.8 µmol/min highest yields were approximately 80 %. Another affected parameter was axial growth rate, which peaked at over 80 nm/s at circa 450 °C. Above 450 °C competing sidewall growth slowed the axial growth. Radial growth and thus tapering were significant at 500 °C and above, otherwise little tapering was observed. The results imply appropriate temperature window of 450-500 °C in the used system.

When the TMG flow was kept constant, increasing the V/III ratio from 7 upwards decreased the yield of epitaxial NWs. However, decreasing the total molar flow increased the yield up to 90 %. This suggests that the yield was dependent on the total molar flow rather than the V/III ratio. The yield being dependent on the total molar flow has not been reported previously. The effect can be due to increased stacking defect density, which promotes kinking. Axial growth rate decreased slightly with increasing V/III ratio due to an As-terminated growth interface and solidification of the seed particle. The axial growth rate increased approximately linearly with increasing total molar flow, and peaked at 120 nm/s with TMG flow of 14 µmol/min and a V/III ratio of 25. On the other hand, then the yield was low.

V/III ratio or total molar flow had little effect on the radial growth. Tapering was slightly affected by V/III ratio, whereas increasing total molar flow decreased it dramatically. As a conclusion, the appropriate window for the V/III ratio with TMG flow of 10.8 µmol/min was between 7 and 25. The value of the total molar flow is a compromise between yield of epitaxial NWs, and growth rate and tapering.

NW length was found to be linearly dependent on the growth time, with nucleation time of 0.25 s. This was notably shorter time than previously reported, which was attributed to Ga addition on the sample before the NW growth step.

The crystal structure was studied with TEM, and ZB with a low density of twin planes was observed. Also shell composition was studied for GaAs/$Al_{0.37}Ga_{0.63}As$ NW with EDS analysis in the TEM. Shell thickness was ~20 nm, which was sufficient for passivation, as was determined by PL measurements on GaAs/$Al_xGa_{1-x}As$ NWs. The measured photon energy decreased from 1.506 eV to 1.396 eV when x_{Al} in the shell was increased from 15.5 to 48.4 %. Redshift with similar CS NWs has been observed

earlier, and it has been proposed to arise from a strained core. However, the magnitude observed elsewhere was much smaller elsewhere than in this work; thus the strain is insufficient to explain the observed remarkable redshift, and more investigation is required instead. PL measurements were performed also on GaAs/$Al_{0.48}Ga_{0.52}As$ NWs with the shells grown at 600, 650 and 700 °C. The PL peak shifted with the with shell deposition temperature, suggesting that the composition varied with deposition temperature. PL intensity was highest with the deposition temperature of 650 °C.

Temperature effects on the PL signal were measured for a GaAs/$Al_{0.22}Ga_{0.78}As$ NW at 20 – 200 K. The signal intensity decreased ~99 % over the measured range. Yet no signal was detected from nonpassivated NWs, which indicates that the passivation increased the PL intensity by several orders of magnitude. The measured band gap shifted from 1.502 to 1.452 eV, which corresponded well to theoretical predictions.

Passivation of GaAs NWs with an in-situ deposited GaAsP shell was studied with x_P = 16 - 100 % in the shell. The signal from the core blueshifted due to shell-induced strain. The highest intensity from the GaAsP passivated NWs was ~25 % of that of with AlGaAs shells, when the same PL measurement values were used. Another studied passivation method ALD-deposited AlN coating. The ALD-passivated samples showed PL peaks which corresponded well to previously reported signals from GaAs NW core and related carbon impurities. Thus it was demonstrated that GaAs NWs can be passivated with the ALD technique.

This study demonstrated that GaAs NWs with few stacking defects can be grown on silicon in an atmospheric-pressure MOVPE reactor. Optimal growth parameters in the used system were a temperature range from 450 °C to 500 °C and a V/III ratio from 7 to 25 with a TMG flow of 10.8 µmol/min. Lower TMG flow increased the yield of epitaxial NWs with a fixed V/III ratio. PL from the NWs was weak unless they were passivated, and the PL improved drastically either with *in-situ* passivation by AlGaAs or GaAsP shells, or with an ALD-deposited AlN layer. The benefits of *in-situ* passivation include simple processing and an oxide-free interface, whereas the advantages of ALD include a wide range of available materials and a low process temperature.

The future studies related to the present work include development and optimization of different passivation methods (such as chemical passivation, other ALD coatings, and CS structures), investigation on effects of the seed particle density and diameter, the growth pressure, NW growth on different substrates, and catalyst-free growth of GaAs NWs on silicon and other substrates. Further investigation is needed also on the two observed phenomena, the notable redshift with AlGaAs shells and the increased kinking with a high total molar flow, which had not been previously reported. From a wider point of view, extensive research is still needed to produce industrially feasible NW applications.

References

[1] Y. Huan, X. Bai and Y. Zhang. In situ mechanical properties of individual ZnO nanowires and the mass measurement of nanoparticles. *Journal of Physics: Condensed Matter,* 2006, Vol. 18, p. L179-L184.

[2] Y. Cui, Q. Wei, H. Park and C. Lieber. Nanowire Nanosensors for Highly Sensitive and Selective Detection of Biological and Chemical Species. *Science,* 2001,Vol. 293, p. 1289-1292.

[3] F. Qian, S. Gradecak, Y. Li and C. Lieber. Core/Multishell Nanowire Heterostructures as Multicolor, High-Efficiency Light-Emitting Diodes. *Nano Letters,* 2005,Vol. 5, p. 2287-2291.

[4] X. Duan, Y. Huang, Y. Cui, J. Wang and C. Lieber. Indium phosphide nanowires as building blocks for nanoscale electronic and optoelectronic devices. *Nature,* 2001,Vol. 409, p. 66-69.

[5] X. Duan, Y. Huang, R. Agarwal and C. Lieber. Single-nanowire electrically driven lasers. *Nature*, 2003, Vol. 421, p. 241-245.

[6] C. Thelander, H. Nilsson, L. Jensen and L. Samuelson. Nanowire Single-Electron Memory. *Nano Letters*, 2005, Vol. 5, p. 635-638.

[7] E. C. Garnett, M. L. Brongersma, Y. Cui, and M. D. McGehee. Nanowire solar cells. *Annual Review of Materials Research,* 2011, Vol. 41, p. 269-295.

[8] O. Oda. *Compound Semiconductor Bulk Materials and Characterizations*. New Jersey, World Scientific, 2007, eISBN: 9789812770387

[9] H. J. Joyce, J. Wong-Leung, Q. Gao, H. H. Tan and C. Jagadish. Phase perfection in Zinc Blende and Wurtzite III-V Nanowires Using Basic Growth Parameters. *Nano Letters,* 2010, Vol. 10 (3) p. 908-915.

[10] . K. A. Dick, P. Caroff, J. Bolinsson, M. E. Messing, J. Johansson, K. Deppert, L. R. Wallenberg and L. Samuelson. Control of III-V nanowire crystal structure by growth parameter tuning. *Semiconductor Science and Technology,* 2010, Vol. 25, p. 024009.

[11] P. Bhattacharya. *Semiconductor Optoelectronic devices.* 2nd edition. New Delhi, Prentice-Hall, 2008.

[12] I. Vurgaftman, J. R. Meyer, and L. R. Ram-Mohan. Band parameters for III-V compound semiconductors and their alloys. *Journal of Applied Physics*, 2001,Vol. 89 (11), p. 5815..

[13] J. Sinkkonen. *Puolijohdeteknologian perusteet*. Espoo, Helsinki University of Technology, 1996.

[14] S. Adachi. *Properties of Semiconductor Alloys*. Weinheim, John Wiley and Sons, 2009. ISBN: 978-0-470-74369-0.

[15] J. Singh. *Semiconductor optoelectronics*. New York, McGraw-Hill, Inc., 1995. ISBN 0-07-113577-4.

[16] K. Dick. *Epitaxial Growth and Design of Nanowires and Complex Nanostructures*. Doctoral thesis, Lund University, Lund, 2007. ISBN 978-91-628-7150-5.

[17] S. Franssila. *Introduction to Microfabrication*. 2nd edition. John Wiley and Sons, 2010. ISBN: 978-0-470-74983-8.

[18] S. Franssila. Introduction to Microfabrication.1st edition.: John Wiley & Sons, 2004.

[19] E. Ertekin, P. A. Greaney, D. C. Chrzan, and T. D. Sands. Equilibrium limits of coherency in strained nanowire heterostructures. *Journal of Applied Physics,* 2005,Vol. 97 (11), p. 114325.

[20] M. Mattila. *Indiumfosfidin Stranski-Krastanow-kasvu organometallisessa kaasufaasiepitaksiassa*. Master's thesis, Helsinki University of Technology, Espoo, 2001.

[21] S. Koshiba, Y. Nakamura, M. Tsuchiya, i. Noge, H. Kano, Y. Nagamune, T. Noda, and H. Sakaki. Surface diffusion processes in molecular beam epitaxial growth of GaAs and AlAs as studied on GaAs (001)-(111)B facet structures. *Journal of Applied Physics,* 1994, Vol. 76 (7), p. 4138-4144.

[22] H. Jussila. *Fabrication of Indium Arsenide Quantum Dot Structure for Semiconductor Optical Amplifiers*. Master's thesis, Helsinki University of Technology, Espoo, 2010.

[23] C. Colombo, D. Spirkoska, M. Frimmer, G. Abstreiter and A. Fontcuberta i Morral. Ga-assisted catalyst-free growth mechanism of GaAs nanowires by molecular beam epitaxy. Physical Review B, 2008, Vol. 77, p. 155326.

[24] L. Schubert, P. Werner, N. D. Zakharov, G. Gerth, F. M. Kolb, L. Long, U. Gösele and T. Y. Tan. Silicon nanowhiskers grown on {111} Si substrates by molecular-beam epitaxy. Applied Physics Letters, 2004, Vol. 84, p. 4968.

[25] C.-Y. Wen, M. C. Reuter, J. Tersoff, E. A. Stach and M. Ross. Structure, Growth Kinetics, and Ledge Flow during Vapor-Solid-Solid Growth of Copper-Catalyzed Silicon Nanowires. *Nano Letters,* 2010, Vol. 10, p. 514-519.

[26] C. Soci, X.-Y. Bao, D.P.R. Aplin, D. Wang. A Systematic Study on the Growth of GaAs Nanowires by Metal-Organic Vapor Deposition. *Nano Letters,* 2008, Vol. 8 (12), p. 4275-4282.

[27] T. Mårtensson, C.P.T. Svensson, B.A. Wacaser, M.W. Larsson, W. Seifert, K. Deppert, A. Gustafsson, L.R. Wallenberg and L. Samuelsson. Epitaxial III-V Nanowires on Silicon. *Nano Letters,* 2004, Vol. 4 (10), p. 1987-1990.

[28] J. Johansson, B.A. Wacaser, K.A. Dick, W. Seifert. Growth related aspects of epitaxial nanowires. *Nanotechnology,* 2006, Vol. 17, p. S355–S361.

[29] X.-Y. Bao, C. Soci, D. Susac, J. Bratvold, D.P.R. Alplin, W. Wei, C.Y. Chen, S.A. Dayeh, K.L. Kavanagh and D. Wang. Heteroepitaxial Growth of Vertical GaAs Nanowires on Si (111) Substrates by Metal-Organic Vapor Deposition. *Nano Letters,* 2008, Vol. 8 (11), p. 3755-3760.

[30] W. Seifert, M. Borgström, K. Deppert, K.A. Dick, J. Johansson. Growth of one-dimensional nanostructures in MOVPE. *Journal of Crystal Growth,* 2004, Vol. 272 (1-4), p. 211-220.

[31] M. Mattila. *Self-Assemled Indium Phosphide Nanowires*. Doctoral thesis, Helsinki University of Technology, Espoo, 2007. ISBN 978-951-22-8812-0.

[32] K. Hillerich, M. E. Messing, L. R. Wallenberg, K. Deppert and K. A. Dick. Epitaxial InP nanowire growth from Cu seed particles. *Journal of Crystal Growth,* 2011, Vol. 315, p. 134-137.

[33] I. Regolin, V. Khorenko, W. Prost, F. J. Tegude, D. Sudfeld, J. Kästner, G. Dumpich, K. Hitzbleck and H. Wiggers. GaAs whiskers grown by metal-organic vapor-phase epitaxy using Fe nanoparticles. *Journal of Applied Physics,* 2007, Vol. 101, p. 054318.

[34] P. Prete and N. Lovergine. *Nanowires*. 1st edition, Vukovar, Intech, 2010. ISBN: 978-953-7619-79-4

[35] M. Mattila, T. Hakkarainen, H. Lipsanen. Catalyst-free fabrication of InP and InP(N) nanowires by metalorganic vapor phase epitaxy. *Journal of Crystal Growth,* 2007, Vol. 298, p. 640-643.

[36] C.J. Yu, and P.K.L. Novotny. Vertically aligned, catalyst-free InP nanowires grown by metalorganic chemical vapor deposition. *Applied Physics Letters,* 2005,Vol. 87, p. 203111.

[37] M. Moewe, L. C. Chuang, S. Crankshaw, C. Chase and D. Chang-Hasnain. Atomically sharp catalyst-free GaAs/AlGaAs nanoneedles grown on silicon. *Applied Physics Letters,* 2008, Vol. 93 (2), p. 023116.

[38] S. Kodambaka, J. Tersoff, M. C. Reuter and F. M. Ross. Diameter-Independent Kinetics in the Vapor-Liquid-Solid Growth of Si Nanowires. *Physical Review Letters,* 2006, Vol. 96, p. 096105.

[39] P. Paiano, P. Prete, N. Lovergine and M. Mancini. Size and shape control of GaAs nanowires grown by metalorganic vapor phase epitaxy using tertiarybuylarsenide. *Journal of Applied Physics,* 2006, Vol. 100, p. 094305.

[40] K.A. Dick. A review of nanowire growth promoted by alloys and non-alloying elements with emphasis on Au-assisted III-V nanowires. *Progress in Crystal Growth and Characterization of Materials,* 2008,Vol. 54, p. 138-173

[41] J. C. Harmand, G. Patriarche, N. Péré-Laperne, M.-N. Mérat-Combes, L. Travers and F. Glas. Analysis of vapor-liquid-solid mechanism in Au-assisted GaAs nanowire growth. *Applied Physics Letters,* 2005, Vol. 87, p. 203101.

[42] M. A. Verheijen, G. Immink, T. de Smet, M. T. Borgström and E. P. A. M. Bakkers. Growth Kinetics of Heterostructured GaP-GaAs Nanowires. *Journal of the American Chemical Society,* 2006, Vol. 128, p. 1353-1359.

[43] H. J. Joyce, Q. Gao, H. H. Tan, C. Jagadish, Y. Kim, M. A. Fickenscher, S. Perera, T. B. Hoang, L. M. Smith, H. E. Jackson, J. M. Yarrison-Rice, X. Zhang and J. Zou. Unexpected Benefits of Rapid Growth Rate for III - V Nanowires. Nano Letters, 2009, Vol. 9 (2), p. 695-701.

[44] A. I. Persson, M. W. Larsson, S. Stenström, B. J. Ohlsson, L. Samuelson and L. R. Wallenberg. Solid-phase diffusion mechanism of GaAs nanowire growth. *Nature Materials,* 2004, Vol. 3, p. 677-681.

[45] K. A. Dick, K. Deppert, T. Mårtensson, B. Mandl, L. Samuelson and W. Seifert. Failure of the Vapor-Liquid-Solid Mechanism in Au-Assisted MOVPE Growth of InAs Nanowires. *Nano Letters,* 2005, Vol. 5, p. 761-764.

[46] S. Kodambaka, J. Tersoff, M. C. Reuter and F. M. Ross. Germanium Nanowire Growth Below the Eutectic Temperature. *Science,* 2007, Vol. 316, p. 729-732.

[47] K. W. Schwarz, and J.Tersoff. Elementary Processes in Nanowire Growth. *Nano Letters,* 2011, Vol. 11, p. 316-320.

[48] K. W. Schwartz, J. and Tersoff. From Droplets to Nanowires: Dynamics of Vapor-Liquid-Solid Growth. *Physical Review Letters,* 2009, Vol. 102, p. 206101.

[49] P. Madras, E. Dailey and F. Drucker. Kinetically Induced Kinking of Vapor-Liquid-Solid Grown Epitaxial Si Nanowires. *Nano Letters,* 2009,Vol. 9 (11), p. 3826-3830.

[50] K.R. Williams, and R.S. Müller. Etch rates for micromachining processing. *Journal of Microelectromechanical Systems,* 1996, Vol. 5, p. 256-269.

[51] G. S. Higashi, R. S. Becker, Y.J. Chabal and A. J. Becker. Comparison of Si(111) surfaces prepared using aqueous solutions of NH4F versus HF. *Applied Physics Letters,* 1991,Vol. 15, p. 1656-1658.

[52] J. H. Woodruff, J. B. Ratchford, I. A. Goldthorpe, P. C. McIntyre and C. E. D. Chidsey. Vertically Oriented Germanium Nanowires Grown from Gold Colloids on Silicon Substrates and Subsequent Gold Removal. *Nano Letters,* 2007, Vol. 7 (6), p. 1637-1642.

[53] H. J. Joyce, Q. Gao, H. H. Tan, C. Jagadish, Y. Kim, X. Zhang, Y. Guo and J. Zou. Twin-Free Uniform Epitaxial GaAs Nanowires Grown by a Two-Temperature Process. *Nano Letters,* 2007, Vol. 7 (4), p. 921-926.

[54] J. Bauer, H. Paetzelt, V. Gottschalch and G. Wagner. GaAs nanowires grown by MOVPE. *Physica Status Solidi b,* 2010, Vol. 247, p. 1294-1309.

[55] P. Caroff, K. A. Dick, J. Johansson, M. E. Messing, K. Deppert and L. Samuelson. Controlled polytypic and twin-plane superlattices in III-V nanowires. *Nature Nanotechnology,* 2009, Vol. 4, p. 50-55.

[56] L. V. Titova, T. B. Hoang, H. E. Jackson, L. M. Smith, J. M. Yarrison-Rice, Y. Kim, H. J. Joyce, H. H. Tan, and C. Jagadish. Temperature dependence of photoluminescence from single core-shell GaAs-AlGaAs nanowires. *Applied Physics Letters,* 2006, Vol. 89, p. 173126.

[57] H. J. Joyce, Q. Gao, H. H. Tan, C. Jagadish, Y. Kim, M. A. Fickenscher, S. Perera, T. B. Hoang, L. M. Smith, H. E. Jackson, J. M. Yarrison-Rice, X. Zhang and J. Zou. High Purity GaAs Nanowires Free of Planar Defects: Growth and Characterization. *Advanced Functional Materials,* 2008, Vol. 18, p. 3794-3800.

[58] S. A. Dayeh, E. T. Yu and D. Wang. III-V Nanowire Growth Mechanism: V/III Ratio and Temperature Effects. *Nano Letters,* 2007, Vol. 7 (8), p. 2486-2490.

[59] K. A. Dick, K. Deppert, L. Samuelson and W. Seifert. Optimization of Au-assisted InAs nanowires grown by MOVPE. *Journal of Crystal Growth,* 2006,Vol. 297, p. 326-333.

[60] V. G. Dubrovskii, N. V. Sibirev, J. C. Harmand, and F. Glas. Growth kinetics and crystal structure of semiconductor nanowires. *Physical Review B,* 2008, Vol. 78, p. 235301.

[61] J. Johansson, L. S. Karlsson, K. A. Dick, J. Bolinsson, B. A. Wacaser, K. Deppert and L. Samuelson. Effects of growth conditions on the crystal structure of gold-seeded GaP nanowires. *Journal of Crystal Growth,* 2008, Vol. 310, pp. 5102-5105.

[62] J. Johansson, L. S. Karlsson, K. A. Dick, J. Bolinsson, B. A. Wacaser, K. Deppert, and L. Samuelsson. Effects of Supersaturation on the Crystal Structure of Gold Seeded III-V Nanowires. Crystal Growth & Design, 2008, Vol. 9 (2), p. 766-773.

[63] J. Johansson, K. A. Dick, P. Caroff, M. E. Messing, J. Bolinsson, K. Deppert, and L. Samuelson. Diameter Dependence of the Wurtzite-Zinc Blende Trasition in InAs Nanowires. *The journal of physical chemistry. B,* 2010, Vol. 114, p. 3837-3842.

[64] J. Johansson, C. P. T. Svensson, T. Mårtensson, L. Samuelson, and W. Seifert. Mass Transport Model for Semiconductor Nanowire Growth. *The journal of physical chemistry B,* 2005, Vol. 109, p. 13567-13571.

[65] X. Ye, H. Huang, X.-M. Ren, Y.-S. Yang, J.-W. Guo, Y.-Q. Huang, and Q. Wang. Growth of Pure Zinc Blende GaAs Nanowires: Effect of Size and Density of Au Nanoparticles. *Chinese Physics Letters,* 2010, Vol. 4, p. 046101.

[66] Y. Kim, H. J. Joyce, Q. Gao, H. H. Tan, C.i Jagadish, M. Paladugu, J. Zou, and A. A. Suvorova. Influence of Nanowire Density on the Shape and Optical Properties of Ternary InGaAs Nanowires. *Nano Letters,* 2006, Vol. 6 (4), p. 599-604.

[67] J. Sinkkonen. Kvanttielektroniikka. Espoo, Helsinki University of Technology, 1998. ISBN: 951-22-4210-9.

[68] D. E. Eastman, and W. D. Grobman. Photoemission Densities of Intrinsic Surface States for Si, Ge, and GaAs. *Physical Review Letters,* 1972, Vol. 28 (21), p. 1378-1381.

[69] A. M. Green, and W.E. Spicer. Do we need a new method for GaAs passivation? *Journal of vacuum science & technology,* 1993, Vol. 11, p. 1061-1069.

[70] K. Tomioka, J. Motohisa, S. Hara, K. Hiruma, and T. Fukui. GaAs/AlGaAs Core Multishell Nanowire-Based Light-Emitting Diodes on Si. *Nano Letters,* 2010, Vol. 10 (5), p. 1639-1644.

[71] Q. Gao, H. H. Tan, H. E. Jackson, L. M. Smith, J. M. Yarrison-Rice, J. Zou, and C. Jagadish. Growth and properties of III-V compound semiconductor heterostucture nanowires. *Semiconductor Science and Technology,* 2011, Vol. 26, p. 014035.

[72] P. Prete, F. Marzo, P. Piaino, N. Lovergine, G. Salviati, L. Lazzarini, and T. Sekiguchi. Luminescence of GaAs/AlGaAs core-shell nanowires grown by MOVPE using tertiarybutylarsenide. *Journal of Crystal Growth,* 2008, Vol. 310 (23), p. 5114-5118.

[73] M. J. Tambe, S. K. Lim, M. J. Smith, L. F. Allard, and S. Gradecak. Realization of defect-free epitaxial core-shell GaAs/AlGaAs nanowire heterostuctures. *Applied Physics Letters,* 2008, Vol. 93, p. 151917.

[74] J.-H. Kang, Q. Gao, H. J. Joyce, H. H. Tan, C. Jagadish, Y. Kim, Y. Guo, H. Xu, J. Zou, M. A. Fickenscher, L. M. Smith, H. E. Jackson and J. M. Yarrison-Rice. Defect-Free GaAs/AlGaAs Core-Shell Nanowires on Si Substrates. *Crystal Growth & Design.* 2011, Vol. 11 (7), p. 3109-3114

[75] N. Sköld, L. S. Karlsson, M. W. Larsson, M-E. Pistol, W. Seifert, J. Trägårdh, and L. Samuelson. Growth and Optical Properties of Strained GaAs-Ga(x)In(1-x)P Core-Shell Nanowires. *Nano Letters,* 2005, Vol. 5 (10), p. 1943-1947.

[76] M. Montazeri, M. Fickenscher, L. M. Smith, H. E. Jackson, J. Yarrison-Rice, J. H. Kang, Q. Gao, H. H. Tan, C. Jagadish, Y. Guo, J. Zou, M-E. Pistol, and C. E. Pryor. Direct measure of Strain and Electronic Structure in GaAs/GaP Core-Shell Nanowires. *Nano Letters,* 2010, Vol. 10 (3), p. 880-886.

[77] B. Hua, J. Motohisa, Y. Kobyashi, S. Hara, and T. Fukui. Single GaAs/GaAsP Coaxial Core-Shell Nanowire Lasers. *Nano Letters,* 2009, Vol. 9 (1), p. 112-116.

[78] F. Jabeen, S. Rubini, V. Grillo, L. Felisari, and F. Martelli. Room temperature luminescent InGaAs/GaAs core-shell nanowires. *Applied Physics Letters,* 2008, Vol. 93 (8), p. 083117.

[79] C. Bocchi, C. Ferrari, P. Franzosi, A. Bosacchi, and S. Franchi. Accurate determination of lattice mismatch in the epitaxial AlAs/GaAs system by high-resolution X-ray diffraction. *Journal of Crystal Growth,* 1992, Vol. 137 (1-4), p. 680.

[80] V. Swaminathan, D. L. Van Heren, J. L. Zilko, P. Y. Lu, and N. E. Schumaker. Characterization of GaAs films grown by metalorganic chemical vapor deposition. *Journal of Applied Physics,* 1985, Vol. 57 (12), p. 5349.

[81] M. Bosund, P. Mattila, A. Aierken, T. Hakkarainen, H. Koskenvaara, M. Sopanen, V.-M. Airaksinen, and H. Lipsanen. GaAs surface passivation by plasma-enhanced atomic-layer-deposited aluminum nitride. *Applied Surface Science,* 2010, Vol. 256 (24), p. 7434-7437.

[82] M. Bosund, A. Aierken, J. Tiilikainen, T. Hakkarainen, and H. Lipsanen. Passivation of GaAs surface by atomic-layer-deposited titanium nitride. *Applied Surface Science,* 2008, Vol. 254 (17), p. 5385-5389.

[83] M. Bosund. *Galliumarsenidipinnan passivointi atomikerroskasvatustekniikalla.* Master's thesis, Espoo, Helsinki University of Technology, 2007.

[84] P. J. Goodhew, F. J. Humphreys, and R. Beanland. *Electron Microscopy and Analysis.* Taylor & Francis, 2000. eISBN: 9780203184257.

[85] K. Hiruma, M. Yazawa, K. Haraguchi, K. Ogawa, T. Katsuyama, M. Koguchi, and H. Kakibayashi. GaAs free-standing quantum-size wires. *Journal of Applied Physics,* 1993, Vol. 74, p. 3162-3171.

[86] D. L. Dheeraj. Growth and structural characterization of III-V nanowires grown by molecular beam epitaxy. Doctoral thesis, Trondheim, Norwegian University of Science and Technology, 2010. ISBN: 978-82-471-2357-7.

[87] D. L. Dheeraj, G. Patriarche, H. Zhou, T. B. Hoang, A. F. Moses, S. Gronsberg, A. T. J. van Helvoort, B-O. Fimland, and H. Weman. Growth and Characterization of Wurtzite GaAs Nanowires with Defect-Free Zinc Blende GaAsSb Inserts. *Nano Letters,* 2008, Vol. 8 (12), p. 4459-4463.

[88] B. G. Streetman, S. Banerjee. *Solid State Electronic Devices*. 5th edition. Prentice Hall, 2000. ISBN: 0-13-025538-6.

[89] Y. Sun, S. E. Thompson, and T. Toshikazy. *Strain Effect in Semiconductors.* Springer, 2009. ISBN: 978-1-4419-0551-2.

[90] A. Nazimov, E. Cohen, A. Ron, B. M. Ashkinadze, and E. Linder. Excitons in GaAs/AlGaAs quantum wells containing a low density two-dimensional electron gas. *Journal of Luminescence,* 2000, Vol. 85, p. 301-307.